Title
pH-weighted Molecular Magnetic Resonance Imaging in Gliomas

Author
Harris, Robert John

Publication Date
2016

UNIVERSITY OF CALIFORNIA

Los Angeles

pH-weighted Molecular Magnetic Resonance Imaging in Gliomas

A dissertation submitted in partial satisfaction
of the requirements for the degree Doctor of Philosophy
in Biomedical Physics

by

Robert John Harris

2016

ABSTRACT OF THE DISSERTATION

pH-weighted Molecular
Magnetic Resonance Imaging in Gliomas

by

Robert John Harris

Doctor of Philosophy in Biomedical Physics

University of California, Los Angeles, 2016

Professor Benjamin M. Ellingson, Chair

Magnetic resonance imaging is an integral part of medical diagnoses, treatment, and evaluation of patients with brain tumors. While standard anatomical imaging is useful, it does not provide information about molecular-level tumor characteristics that may spatially and temporally vary throughout the tumor. As such, there remains a need for the development of novel MRI techniques that can be used for evaluation of tumor growth and treatment response in patients with glioma undergoing radiochemotherapy. Extracellular acidosis is a hallmark of cancer and is intertwined with other common characteristics of the tumor microenvironment including hypoxia and angiogenesis. Therefore, the central objective of this dissertation was to develop a non-invasive imaging technique for identifying regions of acidosis within glioma and surrounding tissues using MRI. The most common types of glioma are highly aggressive and often require radiochemotherapy, which can result in variable responses across the patient population. Information about the acidity characteristics of these gliomas and the surrounding tissue may allow us to more accurately select targets for biopsy and radiation therapy, identify which patients are responding well to treatment, and predict prognosis.

Chemical exchange saturation transfer (CEST) MRI is a molecular imaging technique that generates contrast indirectly from protons on labile functional groups such as amines, amides, and hydroxyls. CEST image contrast is dependent on the exchange rate between bulk water protons and these functional groups, which is in turn dependent upon local pH. Because of this, we hypothesized that we could utilize CEST MRI for pH-weighted imaging in human tissues. By developing simulations of the Bloch-McConnell equations governing chemical exchange, we have shown that the CEST contrast generated by fast-exchanging amino acid amine protons increases with decreasing pH within a physiologically relevant range (6.0-7.4). We have also incorporated experimental scan parameters into these simulations to more accurately simulate the CEST contrast obtained during clinical data acquisition. Data were acquired in amino acid phantoms at varying pH and concentration, verifying our image contrast was dependent on pH. Our pH-weighted MRI sequence was also applied in animal models of glioma, providing evidence it can be used to generate unique contrast within tumors and can serve as a potential biomarker for response to treatment.

Our CEST MRI method was then applied serially in a cohort of glioblastoma patients undergoing treatment with standard radiochemotherapy, along with select cases of patients undergoing targeted biopsy. Results showed that tumor acidity characteristics

were predictive of progression-free survival in the glioblastoma patient cohort. Acidity of targets selected for biopsy on pH-weighted images was indicative of tumor within those biopsy samples. To improve the imaging time of our sequence, we then upgraded the readout to utilize echo-planar imaging (EPI) rather than the standard gradient echo method. This allowed for whole brain coverage and multiple averages within a reduced scan time. The pH-weighted CEST-EPI sequence was applied in healthy volunteers and in a cohort of glioma patients prior to biopsy, in order to select targets for biopsy in regions of acidic and non-acidic tumor tissue. A subset of these patients also underwent PET imaging using ^{18}F-FDOPA, an amino acid analog, near the time of their their pH-weighted scan. ^{18}F-FDOPA uptake was shown to correlate quantitatively and qualitatively with regions of acidity, although pH-weighted imaging provided unique contrast in some cases. pH-weighted MRI was also acquired in recurrent glioblastoma patients before and after the start of treatment with bevacizumab. Acidity was shown to decrease after bevacizumab treatment, and in some cases acidic regions with no apparent contrast enhancement were shown to develop contrast enhancement on follow-up images, indicating that acidic lesions on pH-weighted MRI may be predictive of further tumor growth. Two additional advanced pH-weighted CEST MRI techniques were also implemented. CEST-EPI with a multi-echo readout was developed and acquired in a small cohort of glioma patients. The short and long echoes can provide sensitivity to more and less restricted water molecules, respectively. Separately, our CEST simulation incorporating T_1 and T_2 maps was used to quantitatively calculate estimates of pH in each image voxel for a subset of patients and animal models. This allows us to correct for T_1 and T_2 effects and generate numerical estimates of pH rather than pH-weighted images.

Together, these experiments and results present a comprehensive description of pH-weighted molecular MRI in gliomas. This technique has the potential to be implemented clinically for detection of acidosis in gliomas and other brain pathologies.

The dissertation of Robert John Harris is approved.

Jonathan Goldin

Linda M. Liau

Timothy F. Cloughesy

Daniel B. Ennis

Benjamin M. Ellingson, Committee Chair

University of California, Los Angeles

2016

DEDICATION

This dissertation is dedicated to my fiancé Casey for her continuing support throughout this journey and her companionship on the road ahead.

TABLE OF CONTENTS

ACKNOWLEDGEMENTS

I would like to thank Polly Kay and her team for managing the clinical aspects of many of our projects simultaneously. I would also like to thank Sergio Godinez, Glen Nyborg, Francine Cobla, Kelly O'Connor, Nick Haid, and Karen Hernandez for their technical help during the collection of patient data as well as Lauren Mutascio, Earline Clausell, Andrea Osuna, Oscar Perez, and Anthony Smithson for their help with scheduling and administrative support.

I would like to thank Stanislas Rapacchi, Ziwu Zhou, and Yutaka Natsuaki for their critical help with pulse sequence programming, along with Gerhard Laub and Siemens Medical Solutions for their source code, research collaborations, and scanner accessibility. I would also like to thank Debiao Li for sharing the compiled code of their version of the CEST-GRE sequence.

I would like to thank Andy Frew, Robert Prins, Joseph Antonios, Horacio Soto, David Nathanson, Lisa Ta, Waldy Ladno, and Jelena Zinnanti for their help with pre-clinical experiments on the Bruker 7T system. I would also like to thank William Yong and his team for their histological resources and collaboration.

I would like to thank Whitney Pope, Lea Guo, Brenna Tam, Albert Lai and Tie Li for their assistance with wetlab resources, which were essential to the development of these techniques.

I would like to thank the administrative members of the Physics and Biology in Medicine graduate program (formerly Biomedical Physics), including Dr. Michael McNitt-Gray, Reth Thatch Im, and Terry Moore, for welcoming me into this program and giving me a home for these last six years. I would also like to thank the members of my graduating class, Brendon Villegas, Yazeed Hiyari, Aspram Minasyan, and Yanisley Valenciaga, as well as the other members of this graduate program for accompanying me throughout this experience.

I would like to thank the current and former members of the UCLA Brain Tumor Imaging Laboratory, including Taryar Zaw, Davis Woodworth, Kevin Leu, Anh Tran, Anthony Hardy, and Ruben Nechifor for their assistance during numerous projects.

Finally, I would like to thank my committee members for their constructive criticism and their interest in my research. I would especially like to thank my advisor Dr. Benjamin Ellingson for his countless hours of mentoring, training, advice, and guidance, as well as his genuine commitment to my development as a scientist.

BIOGRAPHICAL SKETCH

2013 MS Biomedical Physics, University of California – Los Angeles, Los Angeles, CA

2010 BS Physics, University of Minnesota – Twin Cities, Minneapolis, MN

PUBLICATIONS

1. **Harris RJ**, Cloughesy TF, Liau LM, Prins RM, Antonios JP, Li D, Yong WH, Pope WB, Lai A, Nghiemphu PL, Ellingson BM. pH-weighted molecular imaging of gliomas using amine chemical exchange saturation transfer MRI. *Neuro Oncol.* 2015; [Epub ahead of print]
2. **Harris RJ**, Cloughesy TF, Hardy AJ, Liau LM, Pope WB, Nghiemphu PL, Lai A, Ellingson BM. MRI perfusion measurements calculated using advanced deconvolution techniques predict survival in recurrent glioblastoma treated with bevacizumab. *J Neurooncol* 2015; 122(3):497-505.
3. **Harris RJ**, Bookheimer SY, Cloughesy TF, Kim HJ, Pope WB, Lai A, Nghiemphu PL, Liau LM, Ellingson BM. Altered functional connectivity of the default mode network in diffuse gliomas measured with pseudo-resting state fMRI. *J Neurooncol* 2013; 116(2):373-9.
4. **Harris RJ**, Cloughesy TF, Pope WB, Godinez S, Natsuaki Y, Nghiemphu PL, Meyer H, Paul D, Behbahanian Y, Lai A, Ellingson BM. Pre- and post-contrast three-dimensional double inversion-recovery MRI in human glioblastoma. *J Neurooncol* 2013; 112(2):257-66.
5. **Harris RJ**, Cloughesy TF, Pope WB, Nghiemphu PL, Lai A, Zaw T, Czernin J, Phelps ME, Chen W, Ellingson BM. ^{18}F-FDOPA and ^{18}F-FLT positron emission tomography parametric response maps (PET PRMs) predict response in recurrent malignant gliomas treated with bevacizumab. *Neuro Oncol*. 2012; 14(8): 1079-89.
6. Chang W, Pope WB, **Harris RJ**, Hardy AJ, Leu K, Mody RR, Nghiemphu PL, Lai A, Cloughesy TF, Ellingson BM. Diffusion MR Characteristics Following Concurrent Radiochemotherapy Predicts Progression-Free and Overall Survival in Newly Diagnosed Glioblastoma. Tomography 2015; 1(1):37-43.
7. Banerjee P, Leu K, **Harris RJ**, Cloughesy TF, Lai A, Nghiemphu PL, Pope WB, Bookheimer SY, Ellingson BM. Association between lesion location and language function in adult glioma using voxel-based lesion-symptom mapping. *Neuroimage Clin*. 2015; 9:617-24.
8. Yogi A, Hirata Y, Karavaeva E, **Harris RJ**, Wu JY, Yudovin SL, Linetsky M, Mathern GW, Ellingson BM, Salamon N. DTI of tuber and perituberal tissue can predict epileptogenicity in tuberous sclerosis complex. *Neurology* 2015; 85(23):2011-5
9. Karavaeva E, **Harris RJ**, Leu K, Shabihkhani M, Yong WH, Pope WB, Lai A, Nghiemphu PL, Liau LM, Chen W, Czernin J, Cloughesy TF, Ellingson BM. Relationship between [18F]FDOPA PET uptake, Apparent Diffusion Coefficient

(ADC), and Proliferation Rate in Recurrent Malignant Gliomas. *Mol Imaging Biol* 2015; 434-42.

10. Ellingson BM, Kim HJ, Woodworth DC, Pope WB, Cloughesy TF, **Harris RJ**, Lai A, Nghiemphu PL, Cloughesy TF. Recurrent glioblastoma treated with bevacizumab: contrast-enhanced T1-weighted subtraction maps improve tumor delineation and predict survival in a multicenter clinical trial. *Radiology* 2014; 271(1):200.
11. Ellingson BM, Sahebjam S, Kim HJ, Pope WB, **Harris RJ**, Woodworth DC, Lai A, Nghiemphu PL, Mason WP, Cloughesy TF. Pretreatment ADC histogram analysis is a predictive imaging biomarker for bevacizumab treatment but not chemotherapy in recurrent glioblastoma. *AJNR Am J Neuroradiol* 2014; 35(4):673-9.
12. Tran AN, Lai A, Li S, Pope WB, Teixeira S, **Harris RJ**, Woodworth DC, Nghiemphu PL, Cloughesy TF, Ellingson BM. Increased sensitivity to radiochemotherapy in IDH1 mutant glioblastoma as demonstrated by serial quantitative MR volumetry. *Neuro Oncol* 2014; 16(3):414-20.
13. Boxerman JL, Ellingson BM, Jeyapalan S, Elinzano H, **Harris RJ**, Rogg JM, Pope WB, Safran H. Longitudinal DSC-MRI for Distinguishing Tumor Recurrence from Pseudoprogression in Patients With a High-grade Glioma. *Am J Clin Oncol* 2014; [Epub ahead of print]
14. Naeini KM, Pope WB, Cloughesy TF, **Harris RJ**, Lai A, Askin A, Chowdhury R, Phillips HS, Nghiemphu PL, Behbahanian Y, Ellingson BM. Identifying the mesenchymal molecular subtype of glioblastoma using quantitative volumetric analysis of anatomic magnetic resonance images. *Neuro Oncol* 2013; 15(5):626-34.
15. Ellingson BM, Mayer E, **Harris RJ**, Ashe-McNally C, Naliboff BD, Labus JS, Tillisch K. Diffusion tensor imaging detects microstructural reorganization in the brain associated with chronic irritable bowel syndrome. *Pain* 2013; 154(9):1528-41.
16. Ellingson BM, Lai A, **Harris RJ**, Selfridge JM, Yong WH, Das K, Pope WB, Nghiemphu PL, Vinters HV, Liau LM, Mischel PS, Cloughesy TF. Probabilistic Radiographic Atlas of Glioblastoma Phenotypes. *AJNR Am J Neuroradiol* 2013; 34(3):533-40.
17. Ellingson BM, Chen W, **Harris RJ**, Pope WB, Lai A, Nghiemphu PL, Czernin J, Phelps ME, Cloughesy TF. PET Parametric Response Mapping for Clinical Monitoring and Treatment Response Evaluation in Brain Tumors. *PET Clinics* 2013; 8(2): 201-217.
18. Ellingson BM, Cloughesy TF, Zaw TM, Lai A, Nghiemphu PL, **Harris RJ**, Lalezari S, Wagle N, Naeini KM, Carrillo J, Liau LM, Pope WB. Functional diffusion maps (fDMs) evaluated before and after radiochemotherapy predict progression-free and overall survival in newly diagnosed glioblastoma. *Neuro Oncol*. 2012; 14(3):333-43.
19. Ellingson BM, Cloughesy TF, Pope WB, Zaw TM, Phillips H, Lalezari S, Nghiemphu PL, Ibrahim H, Naeini KM, **Harris RJ**, Lai A. Anatomic Localization of O6-methylguanine DNA methyltransferase (MGMT) promoter methylated and unmethylated tumors: a radiographic study in 358 de novo human glioblastomas. *Neuroimage* 2012; 59(2):908-16.

CHAPTER I

Background

i. Gliomas

There are approximately 78,000 new primary brain tumors diagnosed in the United States each year, of which 35% are malignant [1]. Brain tumors are typically gliomas, which are graded through conventions described by the World Health Organization (WHO). Grade II gliomas are benign, low-grade tumors that typically grow slowly [2]. Grade III gliomas are anaplastic and are classified as high-grade, malignant tumors [3]. Grade IV gliomas are the most malignant and aggressive type of brain tumor, termed glioblastoma multiforme (GBM) [3]. GBM is also the most common type of primary brain tumor and carries the worst prognosis among brain tumors. Despite decades of research, the median survival rate of 14 months for patients diagnosed with GBM has not changed significantly [4].

The standard of care for GBM treatment is surgical resection in conjunction with radiotherapy and concurrent temozolomide followed by adjuvant temozolomide [5]. Some patients respond to treatment with a reduction in tumor size followed by stability for a year or more; some patients will recur quickly following treatment. This response may depend on factors such as the genetic profile or location of the tumor [6]. Often, a patient's reaction to treatment as assessed by imaging will determine whether to continue with therapy or employ different therapeutic drugs as a second- or third-line treatment. Therefore, imaging techniques for characterizing tumor aggressiveness and an individual patient's response to treatment are critical for managing patient care.

Extracellular acidosis is a hallmark of cancer. A number of studies performed on different cancer subtypes have provided generally consistent evidence of extracellular acidity compared with normal tissues. As described by Gerweck et al., Pampus et al. measured extracellular pH in four human cancer subtypes and found that mean pH was consistently lower in tumor compared to matching healthy tissue measurements (6.87 vs. 7.14, glioblastoma; 6.75 vs 7.10, astrocytoma; 6.92 vs 7.64, uterine cancer; 6.75 vs 7.42, melanoma) [7]. A review by Griffiths et al. compiled a number of studies that found an extracellular pH range of 5.6 to 7.5 in various human cancers compared to 6.9 to 7.6 in healthy tissues [8]. Measures of extracellular pH in pre-clinical models have been consistent with this hypothesis as well. Helmlinger et al. found pH values of 7.03 in a human adenocarcinoma xenograft mouse model compared with 7.30 in healthy tissue [9], while Gallagher et al. found average pH values of 6.71 in a subcutaneous lymphoma mouse model compared with 7.09 in healthy tissue [10]. Cell culture experiments have also provided evidence that low pH is strongly correlated with tumor cell growth, as seen in Figure 1.

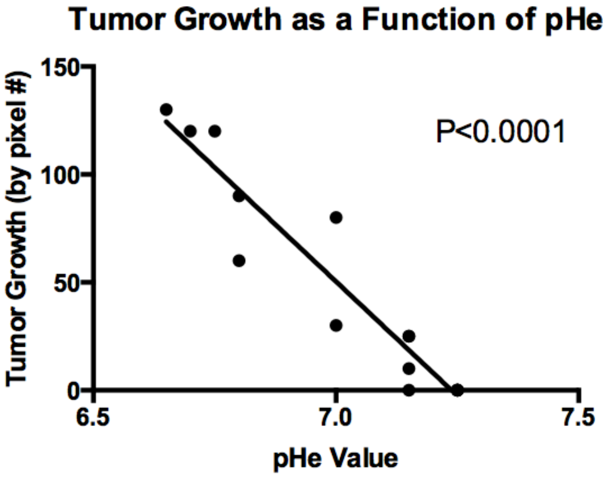

Figure 1. The radial growth outwards of *in vitro* tumor cells compared with the extracellular pH (pHe) measured along a particular radial direction from the cell culture centroid. Results show that radial tumor growth rate is highest in areas of pHe < 7.0. Adapted from [11].

Although the measured pH values for healthy or tumor tissue can vary depending on cancer subtype and experimental method, because of the concordance between results obtained from human, pre-clinical, and *in vitro* studies, the general consensus of a decreased extracellular pH in cancerous tissues is relatively uncontroversial.

Decreased extracellular pH is thought to arise from the downstream effects of local hypoxia due to abnormal blood flow and vasculature in the tumor region [12]. This hypoxia leads to an increase in glycolysis that in turn upregulates production of lactic acid. This lack of oxygen increases glycolysis and results in accumulation of carboxylic acid and lactic acid in the extracellular space [13, 14]. In these acidic conditions, Na^+/H^+ transport between the intracellular and extracellular space is upregulated to maintain a high intracellular pH, resulting in a further decrease in extracellular pH. This acidic environment then essentially creates a positive feedback loop leading to further tumor aggressiveness (Figure 2).

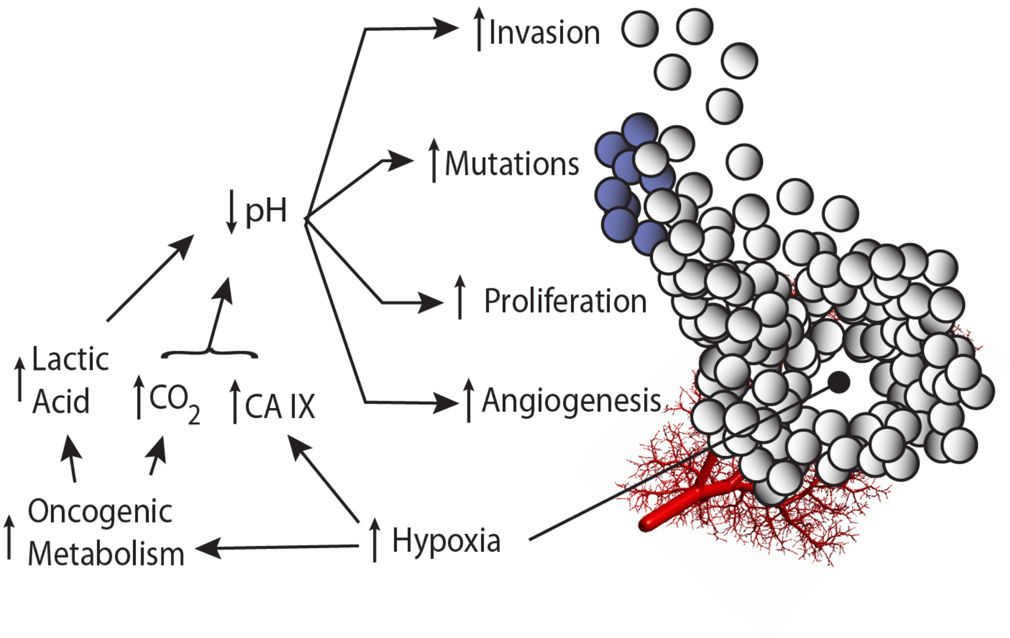

Figure 2. The downstream effects of hypoxia and acidosis create a positive feedback loop leading to further acidosis in proliferative tumor regions [15].

This increase in extracellular acidity can be directly linked to the degree of tumor aggressiveness. A decrease in extracellular pH results in decreased immune function [16], increased chromosomal rearrangements [17], increased tumor invasion [18], and increased angiogenesis through elevated vascular endothelial growth factor (VEGF) [19] and platelet-derived endothelial growth factor receptor (EGFR) [20]. The decrease in extracellular pH also results in resistance to various forms of therapy, including resistance to radiation therapy [21] and specific chemotherapies [22]. All of these characteristics account for a complicated and abnormal microenvironment in regions of tumor growth, one that is in general characterized by acidosis and hypoxia.

ii. Current pH-weighted Imaging Techniques

Currently, there are no well-established methods for non-invasively obtaining fast pH-weighted images with high spatial resolution, although several techniques have been developed, each with various pitfalls.

Phosphorus (^{31}P) spectroscopy provides information about energy metabolism in tissue and can also be used to measure tissue pH [23]. However, this technique has low sensitivity due to the relatively small number of ^{31}P nuclei. Because of this, most ^{31}P data is acquired using large voxels approximately 3x3x3 cm in size for human imaging with long scan times of approximately 17 minutes per voxel [24], making it not suited for clinical evaluation of spatially heterogeneous or small tumors. Additionally, ^{31}P spectroscopy is thought to be sensitive to intracellular pH rather than extracellular tissue [25], so it may not be sensitive to the extracellular acidosis that occurs in regions of tumor.

In buffered solutions, bicarbonate dissociates into carbon dioxide to a degree that is dependent upon pH. Therefore, some studies have used the ratio between ^{13}C-labeled bicarbonate and carbon dioxide as a marker of pH in tissue [26]. However, due to the low natural abundance of ^{13}C, the bicarbonate sample must first undergo hyperpolarization. Therefore this requires both expensive external hyperpolarizing equipment and exogenous contrast and is also typically a low-resolution technique, allowing for matrix sizes of only 16x16 in animal models [10].

Some paramagnetic gadolinium contrast agents have been shown to be sensitive to pH as well [27-29]. However, this again requires an exogenous contrast agent that may not be commonly clinically available. As such, development of endogenous imaging techniques sensitive to pH with high spatial resolution and clinically feasible scan times fulfills a critical need in cancer imaging.

iii. Principles of Magnetic Resonance Imaging

Magnetic resonance imaging (MRI) is a versatile medical imaging technique that can provide qualitative and quantitative information about tissues in the human body. MRI sequences can be tuned to provide information on a variety of tissue properties, including anatomical information, diffusion and perfusion characteristics, magnetization transfer effects, and many others. This section will provide an introduction on the principles of MRI and a foundation for understanding the physics behind chemical exchange saturation transfer (CEST) techniques.

The Larmor Frequency

Protons possess an intrinsic property called spin (**S**), or quantum angular momentum, that has magnitude and direction. A proton's spin results in it possessing a small magnetic moment (**μ**), given by the relationship:

$$\boldsymbol{\mu} = \gamma \boldsymbol{S} \tag{1}$$

where γ is the gyromagnetic ratio, a constant with a value of $\gamma/2\pi = 42.576$ MHz/T for hydrogen. In the absence of an external magnetic field, hydrogen spins in biological samples are randomly oriented and their magnetic moments cancel, resulting in a lack of net magnetization. However, when a strong magnetic field ($\mathbf{B_0}$) is applied to a sample of hydrogen protons, the proton spins align themselves either parallel or anti-parallel to the direction of the magnetic field. The parallel state has a slightly lower energy state than the anti-parallel state, with the energy difference given by:

$$\Delta E = \gamma \hbar B_0 \tag{2}$$

where $\hbar$ is the Planck constant divided by 2π, which has a value of $1.054\text{x}10^{-34}$ J•s. Because of this, a slightly higher population ($\sim 10^{-4}$ % for $B_0 = 3$ tesla) of the magnetic moments will align themselves in the parallel direction. Due to quantization properties, the individual spins retain a longitudinal and transverse component in a frame where the magnetic field is defined as being in the z-direction. However, in a large spin ensemble, the transverse components are randomly distributed and cancel, leaving only the longitudinal component. The net sum of these magnetic moment vectors then results in a nonzero net magnetization (**M**) aligned with the direction of the main magnetic field ($\mathbf{B_0}$). On an individual scale, the external magnetic field produces a torque on the magnetic moments, causing them to precess around the z-axis with an angular frequency known as the Larmor frequency ω, which is given by:

$$\boldsymbol{\omega} = -\gamma \boldsymbol{B} \tag{3}$$

The MRI signal is obtained by measuring the magnetization of these protons after application of a series of radiofrequency (RF) pulses and magnetic gradients.

RF Excitation, Magnetic Gradients, and Relaxation

The signal in MRI is generated as a result of Faraday's law of induction, which states that a changing magnetic field will induce a voltage change in nearby conducting coils. However, by design, the MRI receiver coils detect only transverse signal rather than longitudinal. Because of this, the longitudinal magnetization must first be tipped into the transverse plane before signal acquisition (i.e. readout) can occur. This is accomplished through the use of RF pulses applied to the imaging sample, which tip the magnetization away from its equilibrium orientation along the z-direction and towards the XY-plane. After the RF pulse is no longer applied, the magnetization will begin to return to its equilibrium state along the z-axis. The behavior of a magnetization vector in these conditions is described by the Bloch equations:

$$\frac{dM_x(t)}{dt} = \gamma\left[M_y(t)B_z(t) - M_z(t)B_y(t)\right] - \frac{M_x(t)}{T_2} \tag{4}$$

$$\frac{dM_y(t)}{dt} = \gamma[M_z(t)B_x(t) - M_x(t)B_z(t)] - \frac{M_y(t)}{T_2} \tag{5}$$

$$\frac{dM_z(t)}{dt} = \gamma\left[M_x(t)B_y(t) - M_y(t)B_x(t)\right] - \frac{(M_z(t) - M_0)}{T_1} \tag{6}$$

where **M**(t) is the magnetization at time t, M_0 is the equilibrium magnetization in the z-direction, and T_1 and T_2 are time constants describing the rate of recovery to the equilibrium state for the longitudinal and transverse magnetization components, respectively. The T_1 time constant is dependent upon the rate at which spins leave the higher-energy anti-parallel state and return to equilibrium, and the T_2 constant is dependent upon the phase coherence of the spins in the XY-plane, which are in phase following the RF pulse but immediately begin to dephase afterwards [30]. Different tissues possess different T_1 and T_2 relaxation properties, and the MRI contrast in many anatomical imaging applications is based on these properties. In all cases, $T_1 > T_2$.

In order for MRI to produce an image rather than just a single magnetization measurement, spatial encoding is required. This is accomplished through the use of magnetic field gradients, which are applied in addition to the $\mathbf{B_0}$ field. These gradients are much weaker than the overall the $\mathbf{B_0}$ field. Clinical scanners typically use $\mathbf{B_0}$ fields of 1.5 or 3.0 tesla, while a spatial encoding gradient is typically on the order of 10^{-3} tesla across an imaging volume for clinical scanners. Gradient strengths are typically expressed in terms of millitesla per meter (mT/m). When a gradient (**G**) is applied along the z-direction of an imaging sample, the strength of the total magnetic field at a particular location is then given by

$$\boldsymbol{B}(\boldsymbol{z}) = \boldsymbol{B_0} + \boldsymbol{G} \cdot \boldsymbol{z} \tag{7}$$

Because the Larmor frequency is dependent upon the strength of the applied magnetic field, protons in the imaging sample will have a range of Larmor frequencies corresponding to their spatial position within the gradient. It is this principle that allows for spatial encoding of information with MRI. In addition to gradients along the z-direction, MRI sequences use additional gradients along the x- or y-direction for spatial encoding in three dimensions.

After an RF pulse, the magnetization vectors within an imaging sample precess at different rates depending on their location in the sample, as well as undergoing T_1 and T_2 decay. This changing magnetic field due to the precessing bulk magnetization induces a current in the receiver coils of the MRI scanner [31], producing a composite signal from all frequencies encoded within the sample. A Fourier transform of this composite signal produces image data, with the time domain being converted to a frequency domain:

$$S(\omega) = \int_{-\infty}^{\infty} s(t)e^{-i\omega t}dt \tag{8}$$

where s(t) is the measured signal at time t and S(ω) is the signal in the frequency domain, which will correspond with the magnitude of the magnetization precessing at frequency ω. This magnetization will in turn be dependent on the T_1 and T_2 relaxation times, such that maps of image contrast can be produced in which T_1 and T_2 information is spatially recorded and displayed. Although Eqn. 6 describes a 1-dimensional Fourier transform, typically 2- or 3-dimensional Fourier transforms are used to produce image data.

K-Space

Prior to the Fourier transform, the raw MRI data is collected in a spatial frequency domain referred to as k-space, which has units of inverse meters [32]. In 2-dimensional MRI, each image plane corresponds to one plane of k-space. K-space is traversed by the application of gradients in the x- or y-directions, with the total distance traversed given by

$$k_{x,y} = \bar{\gamma} \int_0^t G_{x,y}(t)\, dt \tag{9}$$

where $\bar{\gamma}$ is the gyromagnetic ratio divided by 2π, $G_{x,y}$ is the magnitude of the gradient applied in either the x- or y-direction, and t is the duration of the gradient. Regions of k-space near the center are low frequency components and are representative of the broader structure of the imaging target, while regions of k-space far from the center are high frequency components that provide the finer spatial resolution in an image. During MRI acquisition, the RF excitation pulse is followed by a series of readout gradients used to traverse k-space while recording complex data at a series of specified points within k-space, referred to as the acquisition matrix. The shape of these readout gradients and the number of data points acquired per excitation pulse are dependent on the type of readout, which can vary between MRI sequences depending on the application.

iv. Chemical Exchange Saturation Transfer

The versatility of MRI arises from its ability to generate different forms of image contrast by using almost limitless combinations of applied RF pulses and magnetic gradients to read out information stored in the spin system as it interacts with its environment. One such application is chemical exchange saturation transfer (CEST). CEST imaging exploits the chemical exchange between bulk water protons within biological tissue and exchangeable protons on other molecules such as proteins, chelates, or smaller metabolites. The CEST effect can be described by a two-pool model of a single solute in water (Figure 3).

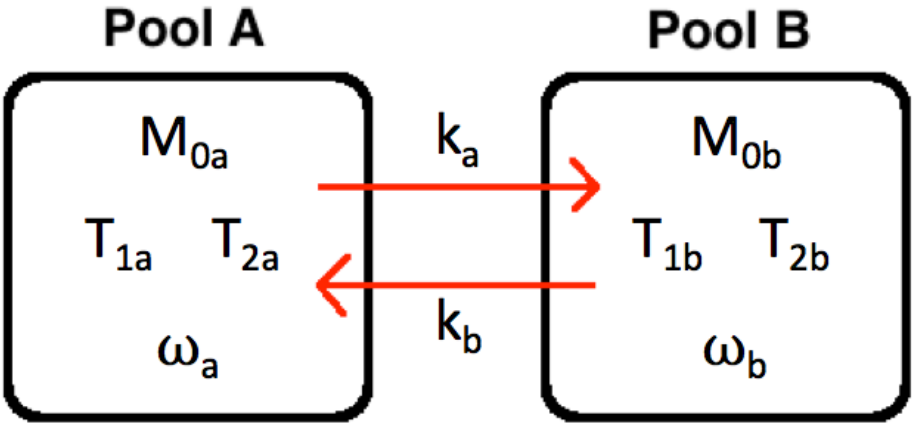

Figure 3. Two-pool model of chemical exchange of hydrogen protons between bulk water (Pool A) and a metabolite (Pool B). Each pool has properties of equilibrium net magnetization (M_0), T_1 and T_2, and a proton resonance frequency (ω).

Although the resonance frequencies of free protons in a particular magnetic field are constant (Eqn. 3), when attached to molecules including water or other metabolites, electron shielding and quantum interactions from other nuclei can cause alterations in the observed local magnetic field near a particular proton and therefore induce slight variations in its resonance frequency ω. Protons on functional groups such as amines (-NH_2), amides (-NH), and hydroxyls (-OH) possess resonance frequencies which are slightly different from the bulk water resonance frequency, which for these purposes is set to 0 Hz in the so-called rotating coordinate frame. During CEST, a preparatory RF pulse is applied at a resonance frequency specific to protons on a functional group undergoing chemical exchange to saturate its longitudinal magnetization and reduce the resulting contribution to the MR signal in the bulk water pool. The magnetization for the bulk water and solute pools can be described by the Bloch equations modified to incorporate chemical exchange, also called the Bloch-McConnell equations [33]:

$$\frac{d\boldsymbol{M}(t)}{dt} = \boldsymbol{X} * \boldsymbol{M}(t) - \boldsymbol{c} \tag{10}$$

in which

$$\boldsymbol{M} = \begin{pmatrix} M_{ax} \\ M_{bx} \\ M_{ay} \\ M_{by} \\ M_{az} \\ M_{bz} \end{pmatrix}, \quad \boldsymbol{X} = \begin{pmatrix} C_{2a} & k_b & -\delta a & 0 & 0 & 0 \\ k_a & C_{2b} & 0 & -\delta b & 0 & 0 \\ \delta a & 0 & C_{2a} & k_b & -\omega_1 & 0 \\ 0 & \delta b & k_a & C_{2b} & 0 & -\omega_1 \\ 0 & 0 & \omega_1 & 0 & C_{1a} & k_b \\ 0 & 0 & 0 & \omega_1 & k_a & C_{1b} \end{pmatrix}, \quad \boldsymbol{c} = \begin{pmatrix} 0 \\ 0 \\ 0 \\ 0 \\ M_{az0}/T_{1a} \\ M_{bz0}/T_{1b} \end{pmatrix} \tag{11}$$

where pool A and pool B are the bulk water protons and solute protons, respectively; M_{a0} and M_{b0} are the equilibrium magnetizations of pool A and B, respectively; k_b is the exchange rate of protons from pool B to pool A; k_a is the exchange rate of protons from pool A to pool B as given by $(M_{b0}/M_{a0})*k_b$; ω_1 is the RF pulse amplitude as given by $\omega_1 = \gamma B_1$, where γ is the gyromagnetic ratio and B_1 is given in μT; $\delta a = (\omega-\omega_a)$ and $\delta b = (\omega-\omega_b)$, where ω is the applied RF saturation frequency, ω_a is the bulk water resonance frequency (0 Hz), and ω_b is the labile proton resonance frequency; T_{1a} and T_{1b} are the longitudinal relaxation times of pool A and B, respectively; and $C_{1a} = (1/T_{1a})+k_a$, $C_{2a} = (1/T_{2a})+k_a$, $C_{1b} = (1/T_{1b})+k_b$, $C_{2b} = (1/T_{2b})+k_b$.

As the longitudinal magnetization of the solute pool is reduced during preparatory RF saturation, the saturated solute protons cause a net reduction in the initial magnetization of bulk water when these protons undergo chemical exchange. The bulk water signal is then acquired, which is the traditional MR contrast for traditional MR techniques. The degree of reduction in the bulk water signal will be dependent upon the RF amplitude ω_1, the time of saturation, the equilibrium magnetizations M_{0a} and M_{0b}, and the chemical exchange rate between the two pools. This chemical exchange rate is in turn dependent upon the chemical properties of the molecules, temperature, and pH [34].

CEST Data Acquisition

When acquiring CEST data, a series of images is typically acquired using a set of serial off-resonance saturation frequencies swept throughout a range of interest. These frequencies are usually expressed in terms of parts per million (ppm) relative to the Larmor frequency, where the bulk water resonance is 0 ppm. Most endogenous metabolites have protons that resonate within a range of approximately -5 to +5 ppm. The series of images at different saturation frequencies is referred to as the “z-spectrum”. When chemical exchange occurs between bulk water and a metabolite, attenuation will appear at the resonance frequency of the metabolite protons as the irradiation frequency is swept across the z-spectrum, as shown in Figure 4.

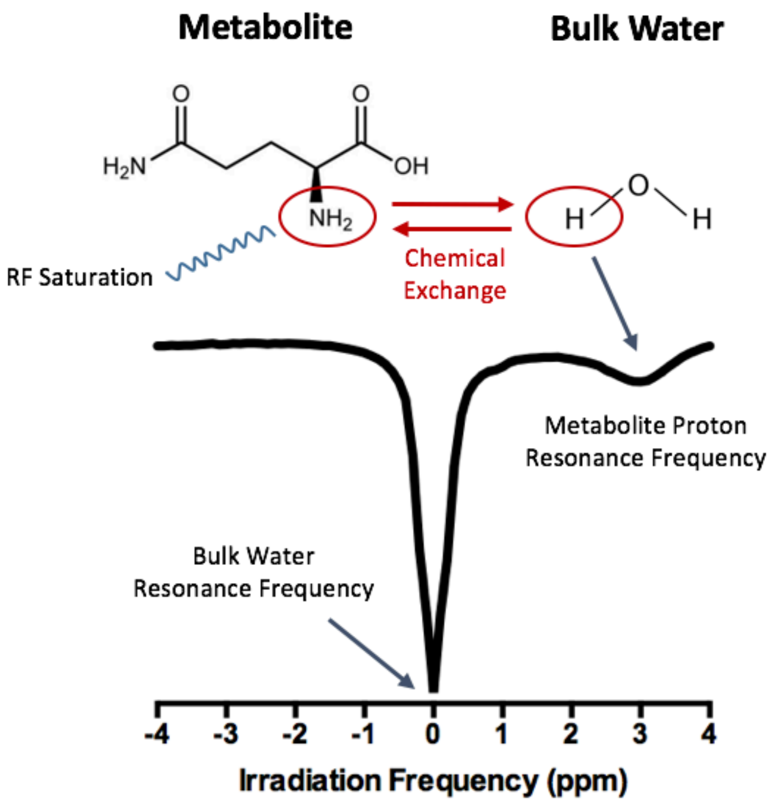

Figure 4. A CEST z-spectrum for a metabolite undergoing chemical exchange with bulk water. Each data point in the z-spectrum represents the image intensity in an image acquired using one off-resonance saturation frequency. A peak appears at the resonance frequency of the labile metabolite protons.

Thus, CEST imaging produces negative contrast in the presence of chemical exchange. A large attenuation peak around 0 ppm arises because at this frequency the bulk water itself is saturated before readout, so the available signal will be very small.

Calculation of Image Contrast

To normalize the z-spectrum, a CEST scan called the S_0 image is often also acquired without the application of an RF saturation pulse. The magnetization transfer ratio (MTR) at a particular frequency in the z-spectrum can be defined as

$$MTR(\omega) = \frac{S(\omega)}{S_0} \tag{12}$$

where $S(\omega)$ is the signal intensity at frequency ω and S_0 is the signal intensity of the S_0 image. The MTR will range between 0 and 1 depending on the degree of bulk water saturation. Because positive image contrast is typically easier to visualize than negative image contrast, and also to remove the influence of T_1 and T_2 characteristics from the image readout and leave only the effects of chemical exchange, CEST data are typically examined in terms of the asymmetry around the water peak, given by MTR_{asym}:

$$MTR_{asym} = MTR(-\omega) - MTR(\omega) = \frac{S(-\omega)-S(\omega)}{S_0} \tag{13}$$

where $-\omega$ is the frequency on the opposite side of the bulk water frequency from ω. This allows us to calculate positive image contrast in the presence of CEST effects, as shown in Figure 5.

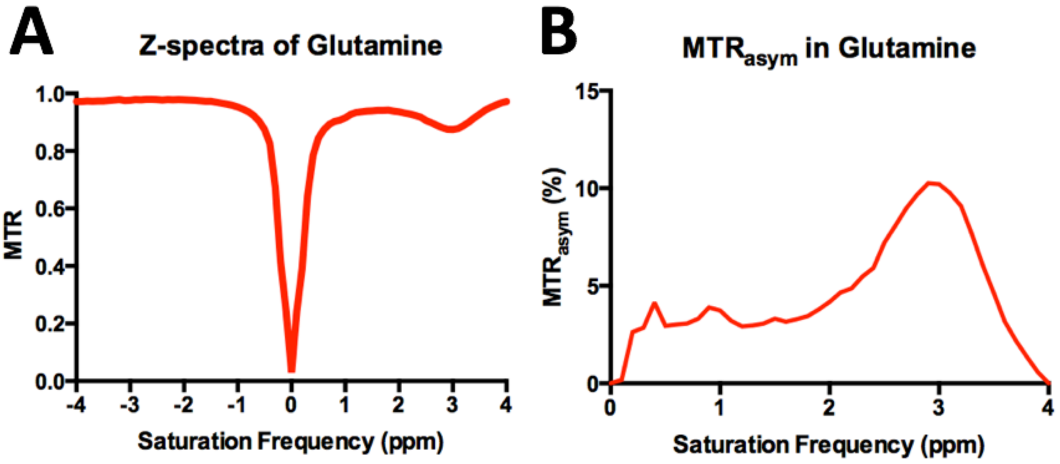

Figure 5. A) Z-spectra of glutamine in water, with attenuation at 3.0 ppm produced by the CEST effect. B) Asymmetry of the data in (A) as calculated by Eqn. 13.

v. Hypothesis

As previously described, the CEST effect is dependent upon the exchange rate between labile protons and bulk water protons, which is in turn dependent upon pH. Previous studies have shown that for most labile groups, the CEST effect decreases with decreasing pH. However, for amine protons that exchange rapidly (~5000 Hz) and have a resonance frequency of 3.0 ppm, the CEST effect increases with decreasing pH (Figure 6).

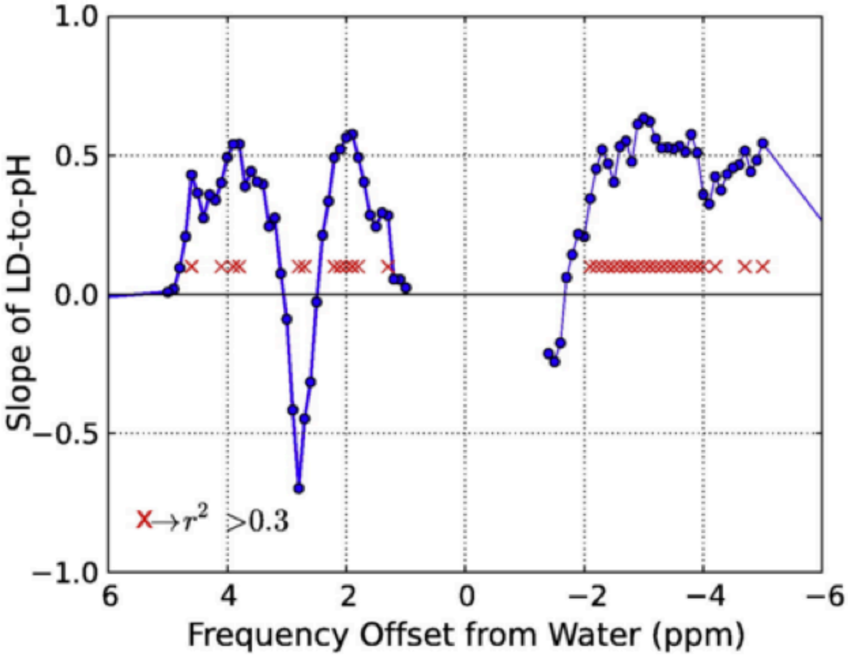

Figure 6. A comparison of the slope between CEST asymmetry and pH as a function of saturation frequency, as measured in a sample of bovine serum albumin (BSA) [35]. An inverse relationship between pH and CEST contrast is seen only for amine protons that resonate at a frequency of approximately 3.0 ppm; the slope is positive for all other offset frequencies.

This property arises due to the fact that in order for a CEST peak to be resolved, the chemical exchange rate between the bulk water and labile protons must be either slower than or approximately equal to the difference in resonance frequencies between those protons [36]. If the exchange rate becomes greater than this difference in resonance frequencies, blurring occurs between the two peaks and the CEST signal will decrease. An increase in pH causes this increase in the exchange rate. For the majority of endogenous labile protons, their exchange rate is low enough that they will remain within the slow to intermediate domain at physiological pH (6.0-7.4), meaning that increases in pH will result in an increase in CEST contrast. Fast-exchanging amine protons such as those found on the backbones of all amino acids, however, move into the fast domain within this physiologically relevant pH range, leading to a reduction in CEST contrast with increasing pH. We therefore hypothesized that CEST targeted to the amino acid backbone amine protons can serve as a biomarker for pH, making this imaging technique sensitive to acidic tissue and proliferating tumor.

vi. Overview of Current CEST Applications

CEST imaging has been applied to target a number of molecules in various settings. Hydroxyl groups have protons with resonance frequencies of approximately 1.0 ppm; although its proximity to the bulk water peak leads to spillover saturation and difficulty obtaining accurate quantitative measurements, many studies have reported promising results targeting hydroxyl groups. Haris et. al. used hydroxyl CEST to measure changes in myo-inositol concentration in a mouse model of Alzheimer's disease [37]. Some studies have targeted the hydroxyl groups on glucose to measure metabolism in tumors, a technique termed glucoCEST [38, 39]. The hydroxyl groups of glycoaminoglycans in cartilage and breast tissue have also been imaged using a technique terms gagCEST [40, 41]. A number of studies have also explored CEST imaging of creatine amine protons, primarily to measure concentration. These protons resonate around 2.0 ppm and exchange more slowly than the fast-exchanging amino acid amine protons at

3.0 ppm, and have been targeted in phantoms, gliomas, and muscle tissue [42-45]. The creatine CEST signal has shown a dependence on pH, but due to the slower exchange regime, the CEST signal increases rather than decreases with increasing pH [46]. This may lead to competing effects of decreased creatine CEST signal from lower pH and increased CEST signal from protein side chains and metabolites that may have elevated concentrations in tumor.

Some recent studies have implemented a pH-sensitive CEST technique using iopromide or iopamidol, two exogenous contrast agents typically used in computed tomography (CT) imaging. Both contrast agents possess two amide proton groups with resonance frequencies at 4.2 and 5.6 ppm, which result in corresponding peaks in the CEST spectra that are modulated with changing pH. Chen et al. showed that the ratio between these two peaks in the presence of iopromide can be used as a measure of pH in phantoms and an animal tumor model [47], and other groups have shown that iopamidol can provide similar contrast in phantoms and an animal tumor model as well [48, 49]. Iobitridol, an x-ray contrast agent, possesses a single amide group at 5.6 ppm and has been used as a pH-sensitive CEST contrast agent by Longo et al. [50]. However, all of these techniques require injection of an exogenous contrast agent, which is not preferable if endogenous pH-sensitive imaging can be achieved. These contrast agents also do not cross the blood brain barrier, and thus would be unable to provide information about local tissue characteristics except in areas of blood brain barrier breakdown.

Paramagnetic compounds have been explored that can be used to enhance imaging of gliomas using CEST, a technique called paraCEST [51, 52]. The majority of these paraCEST contrast agents are compounds bound to lanthanide ions such as Yb^{3+}, Dy^{3+}, Tb^{3+}, or Tm^{3+} [53]. Although gadolinium (Gd^{3+}) is also a lanthanide ion, it causes significant alterations in the relaxation properties of nearby protons; although this can be beneficial for traditional anatomical imaging, it is not desired in the context of paraCEST imaging and is not typically used. The primary advantage of paraCEST techniques is that the contrast agent causes a shift in nearby proton resonance frequencies to spectral regions far away (~kHz) from the water peak, therefore offering advantages in contrast-to-noise ratio and RF labeling efficiency. In principle, this can remove the need for asymmetry analysis of the z-spectrum as well [54]. ParaCEST contrast agents sensitive to pH have been applied in animal tumor models [55, 56]. However, these techniques once again require use of an exogenous contrast agent. Additionally, unlike the off-label use of CT contrast agents, these paramagnetic contrast agents have typically not been approved for safety in human subjects, limiting research to phantom and animal models.

In addition to the techniques described above, the majority of CEST studies performed to date have focused on a specific application of CEST called amide proton transfer (APT) imaging. First described in 2003 [57], APT targets the protons on the backbones of proteins, which resonate at a frequency of 3.5 ppm away from bulk water. These protons have a slow exchange rate (~30 Hz) compared to their chemical shift and will therefore be in the slow regime at all physiological pH values. APT has been applied in glioma [58-60], acute stroke [61, 62], breast tissue [63, 64], Alzheimer's disease [65], neck tissues [66], and other settings. Some previous studies have suggested the use of APT for pH-weighted imaging [67], measuring the decrease in APT signal with decreasing pH seen at these slow exchange rates. However, other studies have suggested that elevated protein content in regions of tumor causes an increase in APT signal in those regions [68]. In tumor regions likely to be both acidic and with elevated protein concentration, these APT effects would act to counteract each other. Conversely, using a biomarker such as amino acid amine CEST in which the signal increases with decreasing pH, the effects would be additive in regions of tumor.

When performing CEST experiments, Nuclear Overhauser enhancement (NOE) effects can result from magnetization transfer between labile and bulk water protons. This effect does not arise due to physical exchange of protons, but rather from cross-relaxation of the proton dipoles [69]. NOE effects have been shown to cause attenuation in the z-spectra downfield from the bulk water frequency, opposite from the region of typical amine and amide effects. When calculating the asymmetry around the bulk water frequency, this can have the effect of reducing the asymmetry caused by traditional CEST effects from endogenous molecules. Fortunately, NOE effects are mainly prevalent at higher field strengths (≥7T), and we do not expect them to become a significant confounding factor at our clinical field strength of 3T. However, in some cases, NOE effects may be targeted as a source of image contrast. At high field strength (≥7T) and low saturation power (<1.0 μT), studies have shown saturation transfer is predominantly mediated by NOE effects [35]. These effects are attributed to aliphatic and olefinic protons in mobile proteins and peptides in tissue [70], and have been shown to decrease in tumor [71]. This effect is thought to be due to abnormal properties of protein folding and water content [72, 73], although it is not yet fully understood. Because the majority of clinical MRI scanners have field strengths of 3T or below, it currently remains difficult to widely implement NOE-based imaging, although NOE contrast may serve as an important molecular biomarker in gliomas imaged at 7T or above.

A few previous studies have explored the targeting of fast-exchanging amine protons during CEST experiments. Jin et al. demonstrated that amine protons at 3.0 ppm are optimally saturated using high-power, short-duration saturation in phantoms, and saw that CEST targeted to this group could identify regions of ischemia in a rat model [74]. Kogan et al. have performed CEST imaging targeted to glutamate protons at 3.0 ppm, using this as a measure of glutamate concentration in the human spinal cord [75]. Scheidegger et al. also measured amine CEST contrast in eight glioma patients using high-power, short-duration saturation and found heterogeneous hyperintensity in tumor regions, although they used an amine resonance frequency of 2.5 rather than 3.0 ppm for simulations and a targeted frequency of 2.0 ppm rather than 3.0 ppm during imaging [76]. Although these studies demonstrate that amine CEST is feasible, a more thorough investigation of its utility in gliomas is needed.

CHAPTER II

Simulation of Amine CEST Contrast for pH-weighted Imaging

It is often instructive to simulate expected results when possible prior to obtaining data experimentally to validate the experimental concept and to estimate the optimal values of experimental parameters. In the case of MR experiments, the dynamic values of magnetization vectors can be simulated as they are perturbed by RF pulses, magnetic gradients, and relaxation to estimate the resulting image contrast [77-79]. In this chapter, we implement a simulation of magnetization vector evolution during a CEST experiment as described by the Bloch-McConnell equations, specifically in the context of pH-weighted imaging.

i. Simulation Background

In a CEST experiment, the contrast measured will depend on the characteristics of the off-resonance RF irradiation pulse, with fast-exchanging amine protons typically requiring pulses of high amplitude to effectively saturate their magnetization [74, 80]. In addition to the amplitude and length of the irradiation pulse, the CEST contrast will also be dependent upon the shape or envelope of the pulse. Although some studies have effectively modeled CEST contrast under RF irradiation [33, 81, 82], these models typically assume a hard RF pulse with a fixed pulse length and amplitude, which may not be the most effective method of saturation and may provide quite different contrast compared with more commonly used RF pulse shapes including Gaussian or *Sinc* pulses. Additionally, these simulations often do not address factors specific to clinical implementation such as differences in repetition time (TR) that may result in incomplete longitudinal magnetization recovery between image acquisitions. As such, development of a more complete model of experimental CEST contrast is warranted.

In the current study we implement an analytical solution for CEST contrast using a two-pool model of bulk water and fast-exchanging amine protons, with modifications to this simulation to account for various RF irradiation pulse characteristics and clinical imaging factors specific to a recently developed CEST echo planar imaging (EPI) sequence for fast clinical pH-weighted imaging. We then modulate properties of the RF irradiation pulse including pulse shape, amplitude, and pulse train length, as well as clinical acquisition parameters and verify our simulations using CEST-EPI applied to physical phantoms containing amino acids at known pH.

ii. Magnetization Evolution Theory

The magnetization of bulk water protons undergoing two-pool chemical exchange with labile proton groups is described previously by Equations 10 and 11. Eqn. 10 can be solved analytically to yield

$$\boldsymbol{M}(t) = e^{\boldsymbol{X}t} \cdot \boldsymbol{M_0}(\boldsymbol{X}/\boldsymbol{c}) - (\boldsymbol{X}/\boldsymbol{c}) \tag{14}$$

where $M_{az}(t_1)$ represents the longitudinal magnetization of bulk water available for subsequent readout after CEST effects (Figure 7A). Assuming the spoiler duration ($t_2 - t_1$) and water excitation pulse duration ($t_3 - t_2$) are negligible, then $M_{az}(t_1) = M_{az}(t_3)$ reflects the available longitudinal magnetization for subsequent readout.

Equations 10-14 have previously been used to model CEST effects under various RF pulse parameters [83, 84]; however, these models often use a single value of ω_1, which describes a hard RF pulse and does not represent more commonly used RF pulses including Gaussian or *Sinc* pulses. To overcome these challenges we first digitized the pulse shape used in our imaging experiments, then modeled these complex RF pulses as the sum of multiple short rectangular pulses.

Additionally, implementation of CEST imaging in a clinical environment often requires acquisition of multiple slices and offset frequencies combined with a short TR for reduced scan time, which can reduce the available longitudinal magnetization within the water pool. Also, the use of non-selective saturation of the metabolite pool combined with a short TR may result in steady-state saturation after several pulses, which can change the amount of available CEST contrast. Therefore, we simulated the relaxation that occurs in both pools during image acquisition, prior to the next off-resonance saturation pulse train, in order to accurately estimate the longitudinal magnetization available for subsequent image acquisition. This relaxation will be described by the Bloch-McConnell equations under the condition $B_1 = 0$ μT, which for the longitudinal magnetization simplifies to:

$$M_{az}(t_5) = M_{az0} - [M_{az0} - M_{az}(t_1)] * e^{-\frac{t_5 - t_1}{T_{1a}}} \quad (15)$$

$$M_{bz}(t_5) = M_{bz0} - [M_{bz0} - M_{bz}(t_1)] * e^{-\frac{t_5 - t_1}{T_{1b}}} \quad (16)$$

where $M_{az}(t_3)$ is the longitudinal magnetization of water protons and $M_{bz}(t_3)$ is the longitudinal magnetization of metabolite protons following completion of the current saturation pulse (assuming spoiling and excitation duration are negligible, or $t_3 = t_1$); $M_{az}(t_5)$ and $M_{bz}(t_5)$ are the longitudinal magnetization for the water and metabolite protons available just prior to the next off-resonance RF saturation pulse train; $t_5 - t_1$ is the time between the end of water excitation and subsequent off-resonance RF saturation; and T_{1a} and T_{1b} are the longitudinal relaxation times for the water and metabolite protons, respectively. CEST sequences often utilize spoiling gradients to destroy remaining transverse magnetization between off-resonance RF saturation and acquisition of the bulk water signal (i.e. from t_1 to t_2). Therefore, to account for the effects of spoiling gradients, transverse magnetization components were set to zero following each saturation pulse.

Lastly, in order to model the effects of pH on the CEST signal, the chemical exchange rate between protons on bulk water and metabolites must be accounted for. The chemical exchange between amino acid amine protons and protons in water can be characterized as a base-catalyzed process, governed by the equation:

$$k_b = k_0 + k_{base} * 10^{-(14-pH)} \tag{17}$$

where k_0 is the default exchange rate, k_{base} is the base-catalyzed rate constant, and k_b is the exchange rate of protons from the metabolite proton pool to the water pool [85]. Although CEST contrast can be simulated as a function of exchange rate, we do not know *a priori* the relationship between pH and the exchange rate for amino acid amines in particular; knowledge of this relationship is necessary to perform simulations of CEST contrast as a function of pH and will be addressed using physical phantoms as described below.

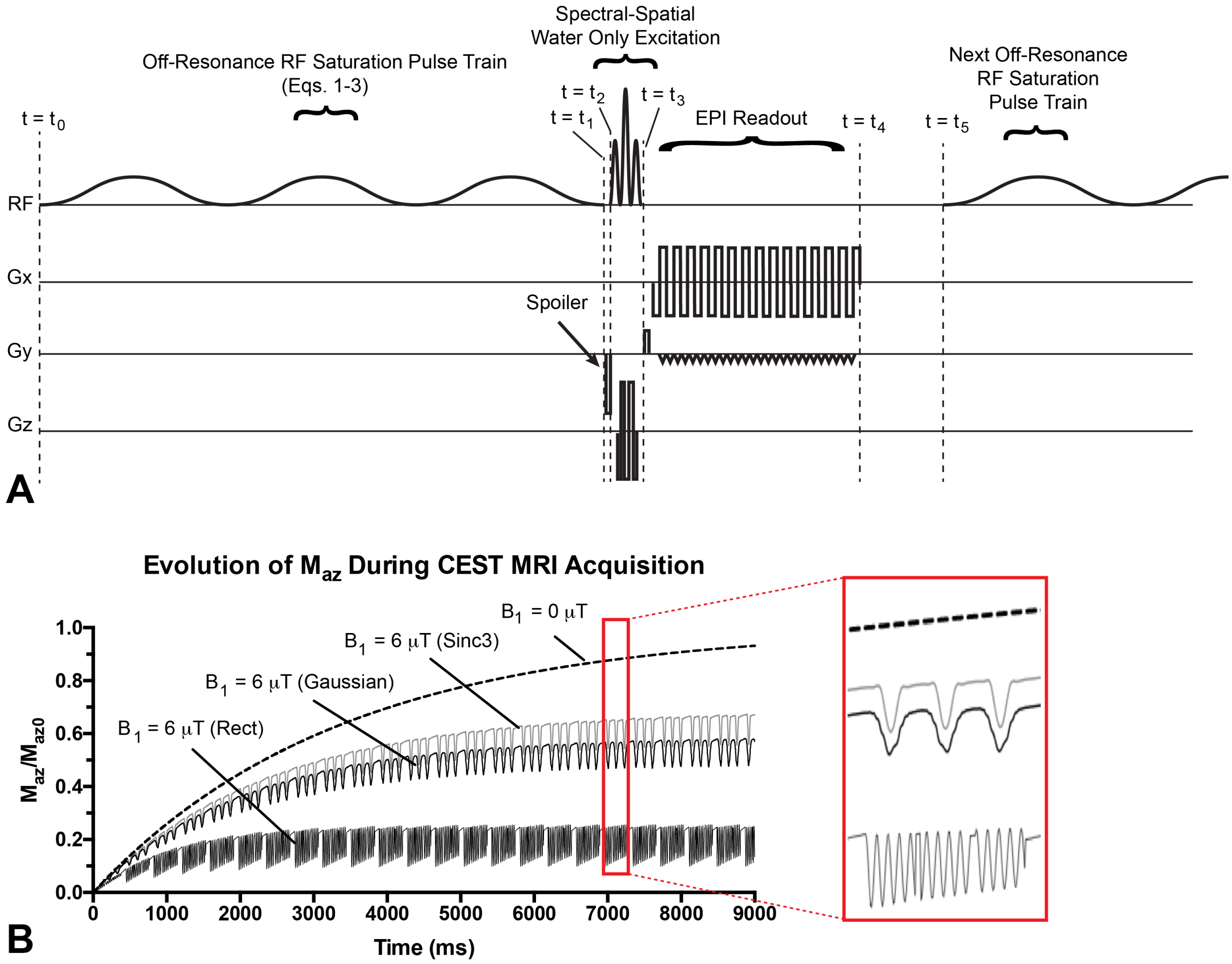

Figure 7. A) Pulse sequence diagram of a CEST-EPI sequence through one repetition. t_0 represents the start of the saturation pulse train, which ends at t_1. Spoiling gradients are played between t_1 and t_2. The spectral-spatial water-only excitation RF pulse is applied between t_2 and t_3. Between t_3 and t_4, EPI readout takes place. The time between t_4 and t_5 represents the time between the completion of readout and the start of the next repetition, which increases with TR. t_5 is equivalent to t_0 for the next repetition. B) Simulated longitudinal bulk water magnetization (M_{az}) at 3.0 ppm during CEST-EPI acquisition in a sample of glutamine in water at pH=6.0. Scan parameters are TR = 380 ms, slices = 25, pulse length = 100 ms, pulse train length = 3 pulses, deadtime = 10 ms. M_{az} is set to zero by the excitation pulse, and competing effects of RF saturation, chemical exchange, and relaxation influence its return to equilibrium. When saturation is applied, attenuation caused by the off-resonance RF saturation pulse train can be seen during recovery (B_1=6 µT). The magnetization time

course is dependent on the applied saturation pulse shape (Gaussian, *Sinc3*, Rect). The measurement of S_0 is given by the recovery of longitudinal magnetization in the absence of saturation (B_1=0 μT). The influence of discrete Gaussian and *Sinc3* pulses can be seen reflected in a corresponding attenuation of M_{az}, while the rectangular pulses result in a more complicated perturbation of M_{az} (red box).

ii. Variation of Model Parameters

Modeling RF Saturation

Gaussian RF pulses were implemented in the Bloch-McConnell equations by dividing a truncated Gaussian waveform of a given duration (standard deviation approximately 20% of total duration, truncated at approximately 2.5 standard deviations) into a series of 101 short block pulses and applying these piecewise block pulses consecutively into the simulation. A *Sinc3* pulse (truncated 3-lobed *Sinc* pulse) and rectangular (hard) RF pulse of constant amplitude were implemented using the same approach. RF saturation pulse trains consisted of a number of these pulses applied consecutively, with a "deadtime" of 10 ms between pulses that is often necessary due to hardware limitations of the RF power amplifier.

Modeling Longitudinal Relaxation After Water Excitation to Estimate Available Longitudinal Magnetization for Subsequent Acquisitions

For the CEST-EPI sequence (Figure 7), one repetition consists of a non-selective RF off-resonance saturation pulse train followed by readout of a single image slice. Because the RF pulse train is non-selective, this saturation was applied during each repetition in our simulation. To simulate the relaxation that occurs in the water pool during image acquisition (free-precession) and prior to the next off-resonance saturation pulse train, Eqns. 15 and 16 were applied between saturation pulse trains with $t_5 - t_1$ = 60 ms (using an echo time (TE) = 27 ms). Eqns. 15 and 16 were also applied during the short deadtime periods (10 ms) between saturation pulses in the pulse train.

Complete Simulation

Because the bulk water longitudinal magnetization in a particular slice is set approximately equal to zero during readout by the 90° spectral-spatial water only excitation pulse (Figure 7A), M_{az0} was set equal to zero at the start of each simulation. The amount of longitudinal magnetization then available in that slice at the next readout is dependent upon the properties of saturation and recovery that occur during the intervening period. Unless stated otherwise, we simulated 25 slices (i.e. 25 repetitions between subsequent 90° excitation pulses) acquired using the minimum TR. This number of slices is appropriate for achieving full brain coverage (~100 mm) with a reasonable slice thickness (4 mm). Although clinical sequences can acquire slices either sequentially or interleaved, the slice order does not affect simulated results. The minimum TR is used by default to minimize the total scan time, which is often desired clinically. An example of the longitudinal bulk water magnetization evolution between one excitation pulse and the next using a 25 slice acquisition is shown in Fig. 1B, with a saturation pulse train consisting of three pulses of amplitude B_1 = 6 μT implemented using either a Gaussian, *Sinc3*, or rectangular waveform. This saturation pulse amplitude was chosen for reasons discussed below. The longitudinal bulk water magnetization evolution using a saturation pulse amplitude of B_1 = 0 μT (S_0 scan) is also shown in Fig. 1B.

To correct for S_0 as described in Eqns. 4 and 5, each simulation was followed by application of an identical simulation with B_1 = 0 μT. The longitudinal magnetization at readout was taken as the value of S_0, and MTR or MTR_{asym} were calculated accordingly. Although longitudinal magnetization decay occurs during readout, this decay affects both the z-spectra and S_0 and therefore cancels out during calculation of MTR or MTR_{asym}.

Calculation of Exchange Rate Constants

To determine the constants k_0 and k_{base} for amino acid amines, a phantom of twelve solutions of 50 mM glutamine dissolved in water at varying pH (5.4 to 7.6 in units of 0.2) was created. Previous studies have shown that amine CEST contrast can be generated using RF pulses of short duration and high amplitude [74, 83, 84]. The maximum Gaussian RF amplitude that can be repeatedly achieved on clinical scanners within hardware limitations was empirically determined to be approximately 6 μT, with Gaussian pulses being the default saturation pulse shape for magnetization transfer applications. This saturation pulse amplitude was calculated via the relationship between the integral of the pulse waveform and the total saturation pulse flip angle, which is the input used by the scanner software. CEST-EPI data were acquired for this phantom on a Siemens 3T Prisma system using a saturation pulse train consisting of 3x100 ms Gaussian pulses of amplitude $B_1 = 6$ μT (TR=380 ms), with 51 spectral points acquired between -5.0 and 5.0 ppm. Glutamine samples were split into two groups of six, as our phantom held a maximum of six samples (Figure 8A). MTR_{asym} at 3.0 ppm was calculated for the solutions of different pH.

A nonlinear least-squares model (*lsqnonlin*, Matlab) was used to estimate k_0 and k_{base} as variables using the simulation equations applied to phantom measurements. For the simulation, T_1 and T_2 of bulk water (T_{1a} and T_{2a}) were estimated as 3.375 s [86] and 2.500 s [87], respectively. The T_1 and T_2 of the amine pool (T_{1b} and T_{2b}) were estimated as 0.2 s and 0.1 s, respectively, based on estimates from the literature [33, 88-90]. After fitting, the resulting values of k_0 and k_{base} were then used to calculate the amine exchange rate k_b from pH for a specific pH. To verify the repeatability of k_0 and k_{base} measurements and the accuracy of resulting simulations, the same pH phantom was scanned using a similar CEST-EPI sequence, but replacing the Gaussian saturation pulses with *Sinc3* pulses. The previously measured values of k_0 and k_{base} were used to generate the expected z-spectrum during application of *Sinc3* pulses and the respective acquisition parameters. Pearson's correlation coefficient was used to assess the association between the simulated and measured values of MTR_{asym}.

Comparison of Simulated and Experimental Z-Spectra

The fidelity of the simulations was tested against phantom data for Gaussian, *Sinc3* and rectangular pulses. Both simulations and experimental acquisitions used a saturation pulse train of 3x100 ms pulses with amplitude $B_1 = 4\ \mu T$ for Gaussian, *Sinc3* and rectangular pulse shapes and a *TR*=380 ms applied to a phantom containing 50 mM glutamine at a pH of 6.0. This lower saturation pulse amplitude was used to compare pulse shapes because rectangular saturation pulses with amplitude $B_1 = 6\ \mu T$ could not be repeatedly applied within the limits of the RF power amplifier. The simulated and experimental z-spectra were directly compared for each pulse type to verify the correlation had an approximate slope of unity.

Effects of Saturation Pulse Shape on Z-spectra in Tissues

Biopsies of human cortex have found the concentration of amino acids in brain tissue to be approximately 20-25 mM [91]. In addition to the standard proteinogenic amino acids, many amino acid derivative metabolites including norepinephrine, 5-hydroxytryptophan, levodopa, and other neurotransmitters possess an amine group that will contribute to the signal at 3.0 ppm as well. Proteins such as bovine serum albumin (BSA) have also shown characteristics of a fast-exchanging amine component at 3.0 ppm [35], likely from common amine groups on exposed protein side chains. Thus, a total amine concentration of 50 mM was assumed in neural tissues and used for simulation purposes in normal-appearing white matter (NAWM) (T_{1a} = 1.22 s, T_{2a} = 0.107 s) [92, 93], tumor tissue (T_{1a} = 1.37 s, T_{2a} = 0.170 s) [93, 94] and cerebrospinal fluid (CSF) (T_{1a} = 3.375 s, T_{2a} = 2.500 s, similar to fluid phantoms). A T_{1b} of 0.2 s and T_{2b} of 0.1 s were again used for the amine pool. To demonstrate the effects of saturation pulse shape on the CEST effect in tissue, we first simulated application of a Gaussian, *Sinc3*, and rectangular pulse train all consisting of 3x100 ms pulses of amplitude 6 μT (TR=380 ms) at pH=6.0. MTR at spectral points between -5.0 and +5.0 ppm were calculated to obtain simulated z-spectra in these tissues.

Effects of Saturation Pulse Discretization on Z-spectra

A sufficient number of discretized data points describing the Gaussian or *Sinc3* pulses must be used to accurately simulate the pulse shape. To test the effect of changing the pulse bin size, we simulated application of our clinical scan parameters on a sample of 50 mM glutamine in water at pH=6.0 using a saturation pulse train of 3x100 ms Gaussian pulses at amplitude 6 μT (TR=380 ms) and a bin size of 25, 50, 75, 101, 151, or 301. MTR at spectral points between -5.0 and +5.0 ppm were calculated.

Comparison of Saturation Pulse Lengths

Clinical scanners often have limitations on the length of the RF pulse that can be delivered. The maximum pulse length empirically achievable on our scanners is approximately

100 ms, in line with other studies [95]. However, it remains unclear whether pulse trains consisting of higher numbers of short pulses, such as those suggested in some studies [63], is preferable to a lower number of pulses with longer saturation duration. To determine the dependence of MTR_{asym} at 3.0 ppm on pH for different saturation pulse durations for NAWM, glioma and CSF, RF saturation pulses with a total saturation of approximately 300 ms per repetition were examined under four scenarios: A) 12x25 ms pulses; B) 6x50 ms pulses; C) 3x100 ms pulses; and D) 1x300 ms pulse. A deadtime of 10 ms was used between all pulses. Because the additional deadtimes between shorter saturation pulses will lengthen the total pulse train time, t_5-t_1 was adjusted to keep an identical TR=470 ms and equivalent saturation time integral between simulations (t_5-t_1 = 60, 120, 150, and 170 ms, respectively).

Effects of Repetition Time and Pulse Train Length

Next, the dependence of MTR_{asym} at 3.0ppm on pH was evaluated for different TR using a constant saturation pulse train length to understand the effects of increasing longitudinal relaxation time between saturation pulse trains for NAWM, glioma and CSF. The minimum TR achievable on a 3T Siemens Prisma for a pulse train of 3x100 ms Gaussian pulses is 380 ms (t_1-t_0 = 320 ms, t_5-t_1 = 60 ms). The TR was varied between 380, 500, 1000, and 2000 ms while holding the pulse train length and all other parameters constant. The effect of the specific number of 100 ms pulses used in the pulse train was also examined for the minimum TR available. Pulse train lengths of 1, 2, 3, 5, and 25 pulses were used with minimum TRs of 160, 270, 380, 600, and 2580 ms, respectively.

Effects of Saturation Pulse Amplitude and Scanner Field Strength

The dependence of MTR_{asym} at 3.0ppm on pH was then tested for various B_1 pulse amplitudes. A saturation pulse train consisting of 3x100 ms Gaussian pulses of amplitudes B_1 = 2, 4, 6, and 8 μT were used with TR=380 ms. Additionally, the dependence of MTR_{asym} at 3.0ppm on pH was also explored for various B_0 field strengths including 1.5, 3.0, 7.0, 9.4, and 11.0 T, again using a saturation pulse train of 3x100 ms Gaussian pulses of B_1 = 6 μT and TR=380 ms.

Effects of Proton Relaxation Times

The influence of relaxation rates for both bulk water and the labile proton pool on MTR_{asym} at 3.0 ppm for various pH were then examined. NAWM relaxation rates were used as reference values. T_{1a} was varied between 0.5 and 3.0 s, T_{2a} was varied between 0.05 and 0.3 s, T_{1b} was varied between 0.001 and 1.0 s, and T_{2b} was varied between 0.0001 and 0.1 s. A saturation pulse train of 3x100 ms Gaussian pulses of amplitude B_1 = 6 μT and TR=380 ms were used for simulation purposes.

Effects of Amine Concentration

Lastly, the dependence of MTR_{asym} at 3.0ppm on pH was then tested for varying amine concentrations. The amine concentration was varied between 5, 25, 50, 100, and 200 mM, using a saturation pulse train of 3x100 ms Gaussian pulses of amplitude B_1 = 6 μT and TR=380 ms.

iv. Simulation and Phantom Results

Calculation of Exchange Rate Constants

We obtained $k_0 = 75.9$ Hz, $k_{base} = 5.64$ Hz as the optimal solution to Eq. 8 by fitting phantom data acquired using Gaussian saturation pulses (Figures 8A&B, $R^2 = 0.985$). These values were then used to calculate the amine exchange rate k_b from pH for the remainder of these simulations. After using those parameters to implement a simulation using *Sinc3* pulses, the resulting simulated data matched well to experimental *Sinc3* pulse data (Figures 8C&D; $R^2 = 0.976$).

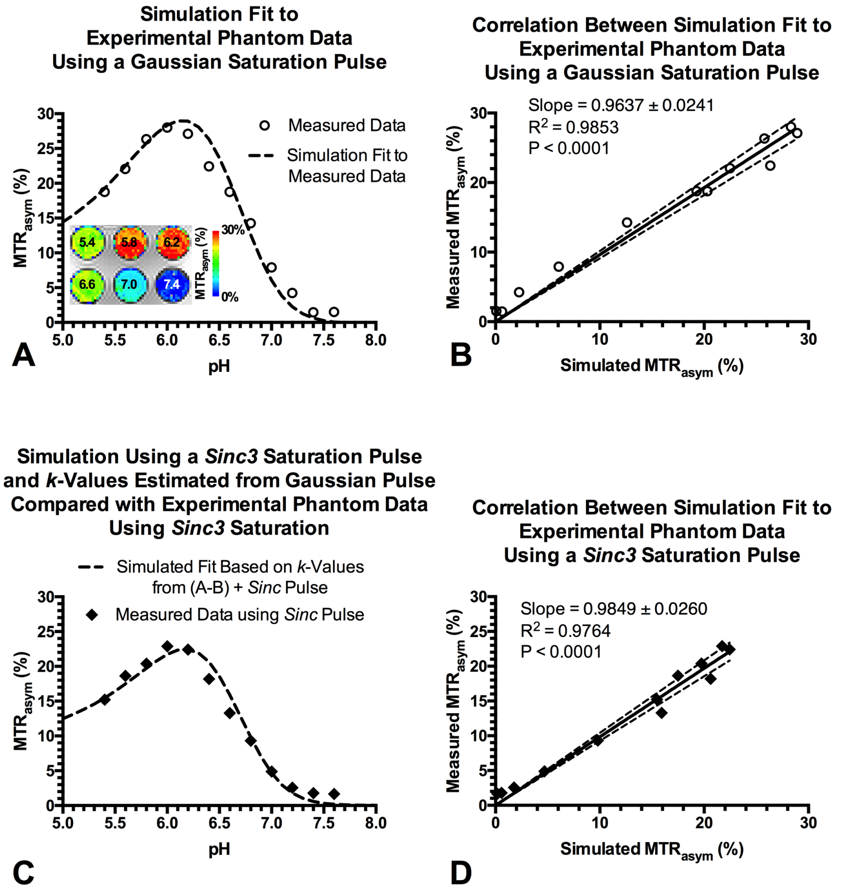

Figure 8: A) Simulation fit to experimental phantom (50 mM glutamine at varying pH) data using a Gaussian saturation pulse and CEST-EPI. B) Correlation between simulation fit to experimental phantom data using a Gaussian saturation pulse. C) Simulation using a *Sinc3*

saturation pulse and *k*-values estimated from the Gaussian pulse compared with experimental phantom data using *Sinc3* saturation and CEST-EPI. D) Correlation between simulation fit to experimental phantom data using a *Sinc3* saturation pulse.

Comparison of Simulated and Experimental Z-Spectra

The simulated estimates of the z-spectrum matched well with experimental data for Gaussian, *Sinc3* and rectangular pulses at pH = 6.0 (Figures 9A-C). Interestingly, rectangular saturation pulses showed oscillations in the z-spectra for both simulations and experimental data, along with increased overall attenuation over all frequencies compared with Gaussian and *Sinc3* pulses (Figure 9C). Experimental values of MTR_{asym} closely resembled the simulated data as well (Figures 9D-F), with Gaussian pulses providing slightly higher MTR_{asym} at 3.0 ppm than *Sinc3* pulses in both simulated and experimental data. Direct comparisons between simulated and experimental spectral points are shown in Figures 9G-I. Linear fitting of these data points indicated that the slopes were only 1%, 1%, and 6% away from unity for the Gaussian, *Sinc3*, and rectangular pulse trains, respectively.

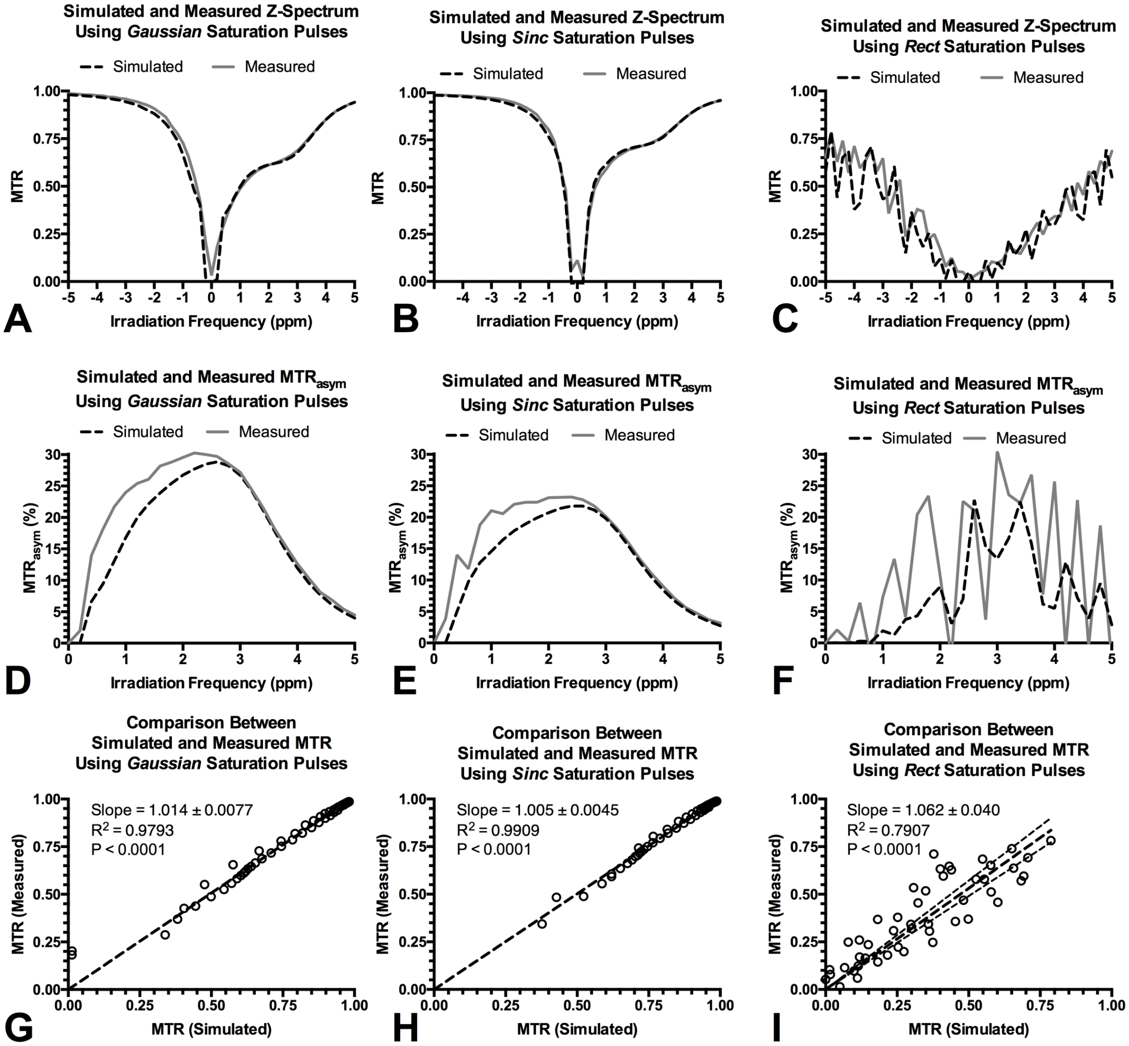

Figure 9: Simulated and experimental z-spectra for a water phantom of 50 mM glutamine at pH=6.0 using a CEST-EPI sequence with (A) Gaussian, (B) *Sinc3*, and (C) rectangular RF pulses. (D), (E) and (F) show MTR$_{asym}$ for the data shown in (A), (B) and (C), respectively. (G), (H), and (I) show a comparison of the simulated and experimental spectral points shown in (A), (B), and (C), respectively.

Effects of Saturation Pulse Shape on Z-spectra in Tissues

In NAWM and tumor tissue, Gaussian and *Sinc3* pulses again produced less overall attenuation across all frequencies than rectangular pulses (Figures 10A&B). Z-spectra in NAWM and tumor were overall more attenuated than in CSF z-spectra (Figure 10C). Gaussian and *Sinc3* pulses also had peaks more specific to the amine frequency of 3.0 ppm than the rectangular pulse in NAWM and tumor (Figures 10D&E).

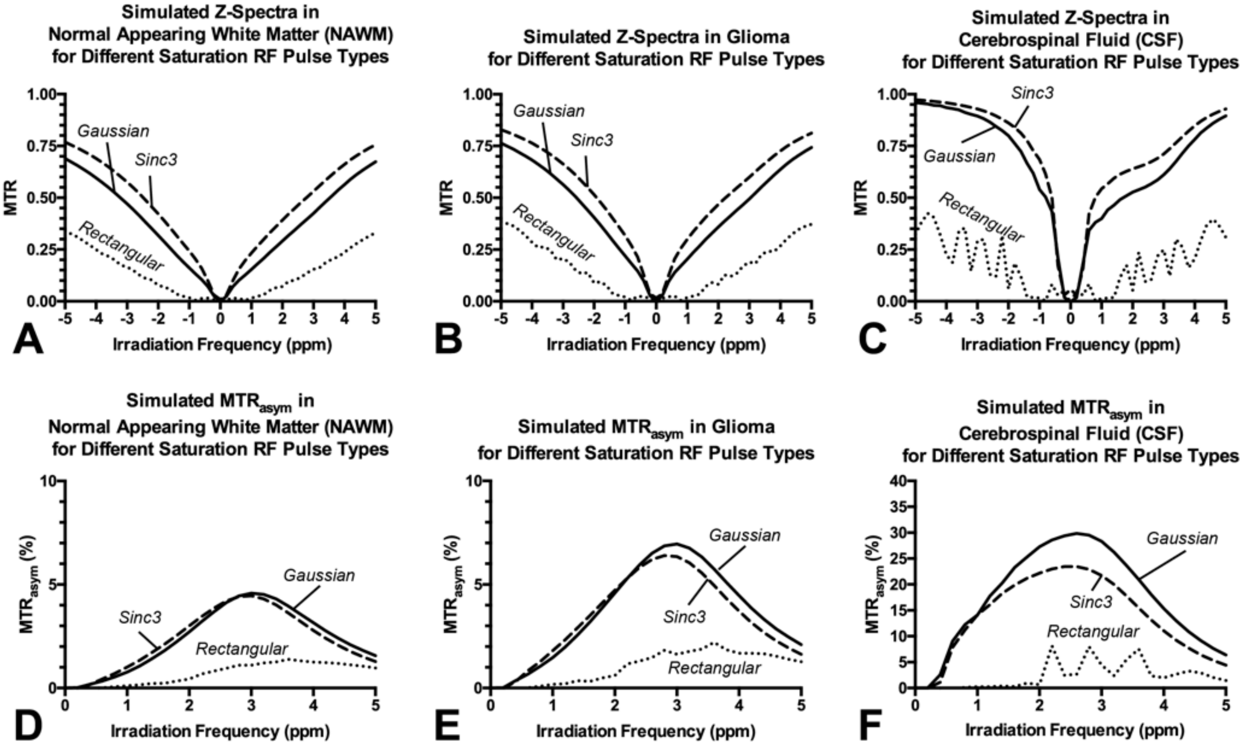

Figure 10: Z-spectra for a two-pool amine model in (A) NAWM, (B) tumor and (C) CSF for different saturation pulse shapes. (D), (E) and (F) show MTR$_{asym}$ for the data shown in (A), (B) and (C), respectively. Gaussian and *Sinc3* pulses appear to produce more contrast specific to 3.0 ppm than rectangular pulses.

Effects of Saturation Pulse Discretization on Z-spectra

We aimed to determine the number of bins required to accurately simulate an arbitrary pulse shape such as a Gaussian pulse. Results showed artifacts that appeared in the z-spectra without a sufficiently high number of bins, as seen in Figure 11.

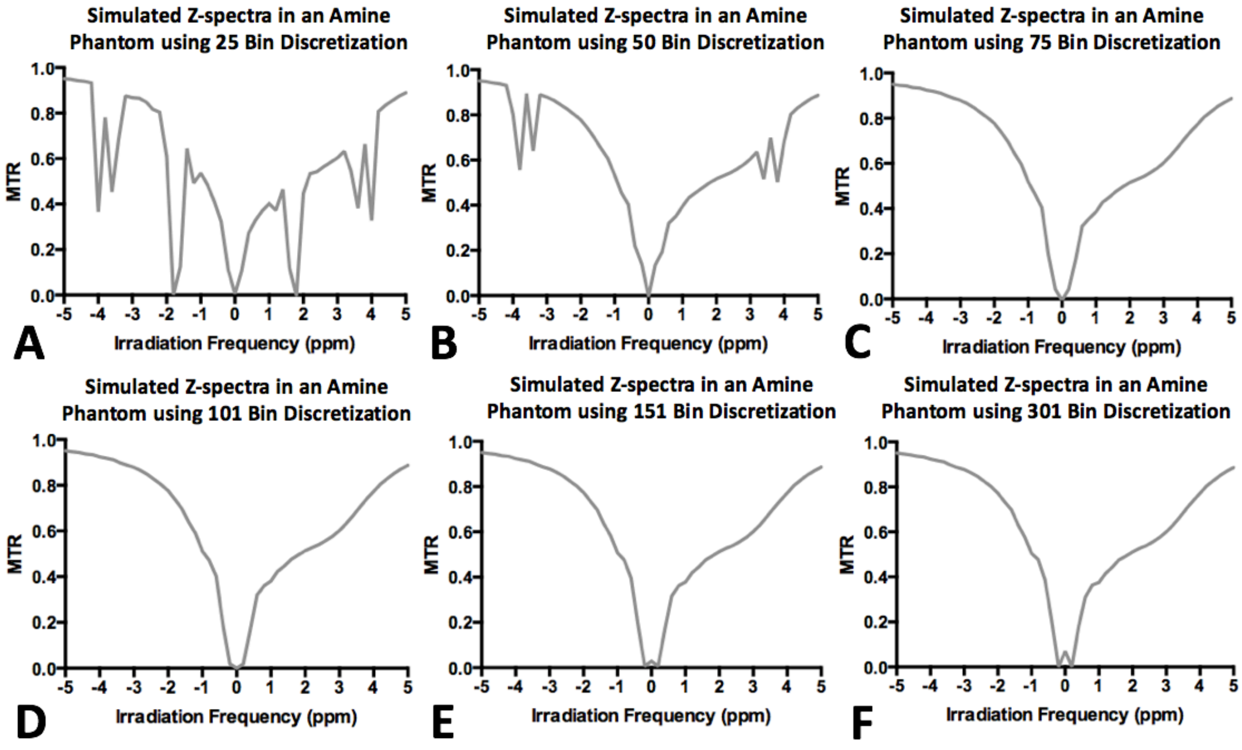

Figure 11. Z-spectra of two-pool amine model in water at pH=6.0. The discretization of the simulated Gaussian pulses is varied from 25 to 301 bins. Spectra are almost identical after reaching sufficient bin size, but artifacts occur below this limit.

Empirically, approximately 75 bins of width 1.35 ms were required to obtain spectra without periodic artifacts. After reaching this bin number, the spectra did not significantly change with increasing bin number. Because of this, the value of 101 bins used during our simulations appears to be a sufficient tradeoff between computation time and simulation accuracy.

Comparison of Saturation Pulse Lengths

Our next aim was to determine the optimal saturation pulse length given a set total pulse train length. Changes in saturation pulse length did not result in consequential differences in

$\mathrm{MTR}_{\mathrm{asym}}$ at 3.0 ppm in any of the three tissue types (Figures 12A-C). In NAWM and glioma, $\mathrm{MTR}_{\mathrm{asym}}$ at 3.0 ppm was slightly higher for pulses of 100 ms (Figures 12A&B). In CSF, $\mathrm{MTR}_{\mathrm{asym}}$ at 3.0 ppm was slightly higher when using one 300 ms pulse (Figure 12C). These results suggest saturation pulse trains using 100 ms pulses may be preferred for characterization of glioma tissues.

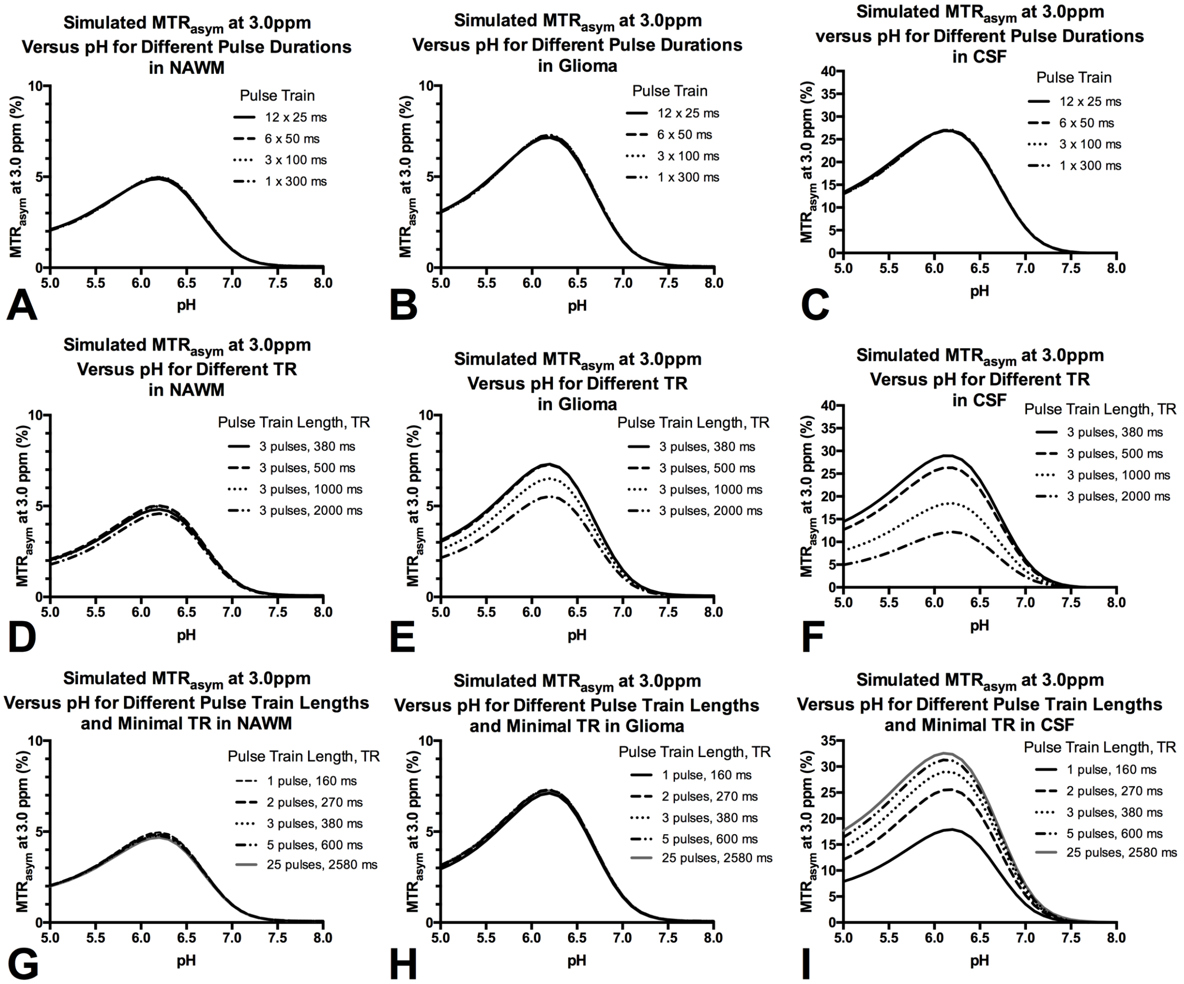

Figure 12: (A-C) Comparison of Gaussian pulse length in the saturation pulse train and the effect on pH sensitivity in (A) NAWM, (B) tumor, and (C) CSF. (D-F) $\mathrm{MTR}_{\mathrm{asym}}$ as a function of pH for varying TR and constant pulse train length in (D) NAWM, (E) tumor, and (F) CSF. (G-I) $\mathrm{MTR}_{\mathrm{asym}}$ as a function of pH for saturation pulse trains consisting of either one, two, three, five, or twenty-five 100 ms Gaussian pulses at minimum TR for (G) NAWM, (H) tumor, and (I) CSF.

Effects of Repetition Time and Pulse Train Length

Both glioma tissue and CSF showed decreased MTR_{asym} at 3.0 ppm with increasing TR (Figures 12E&F). This is likely due to increased longitudinal relaxation taking place between saturation pulse trains. In NAWM, MTR_{asym} at 3.0 ppm increased slightly with increasing TR before decreasing with further increases in TR (Figure 12D), although the effects of TR on the contrast were not as pronounced as in tumor tissue. These results suggest the minimum allowable TR is preferred for for pH-weighted contrast.

The difference in MTR_{asym} at 3.0 ppm for NAWM and glioma was small when changing the saturation pulse train length and selecting the minimum allowable TR (Figures 12G&H). However, in CSF, a longer pulse train resulted in higher MTR_{asym} at 3.0 ppm (Figure 12I). For pH between 6.0 and 7.0 in CSF, MTR_{asym} at 3.0 ppm reached approximately 90% of the maximum contrast available when using a pulse train length of 3 (Figure 12I). This suggests three pulses may be preferred for obtaining at least 90% of allowable pH-weighted contrast for all tissues of interest within the brain.

Effects of Saturation Pulse Amplitude and Scanner Field Strength

When varying the RF pulse amplitude B_1, results showed that the pH range with CEST sensitivity shifts towards higher pH values with higher B_1 (Figures 13A-C). In tumor tissue, maximum MTR_{asym} at pH values below 6.5 appeared to be maximized at 4 μT, although the resulting curves for 4 and 6 μT were approximately equal down to a pH of 6.5 (Figure 13B). In CSF, MTR_{asym} was maximized at high B_1 values of 6 and 8 μT (Figure 13C). When varying the scanner field strength B_0, results showed that MTR_{asym} generally increased at higher field strength, although the dependence of MTR_{asym} on field strength was not linear and approached a maximum at high field strength (Figures 13D-F). The pH range with CEST sensitivity also shifts to higher pH with increased B_0. This data indicates that pH-weighted amine CEST will not be as effective using a field strength of 1.5T compared with field strengths of 3.0T or higher.

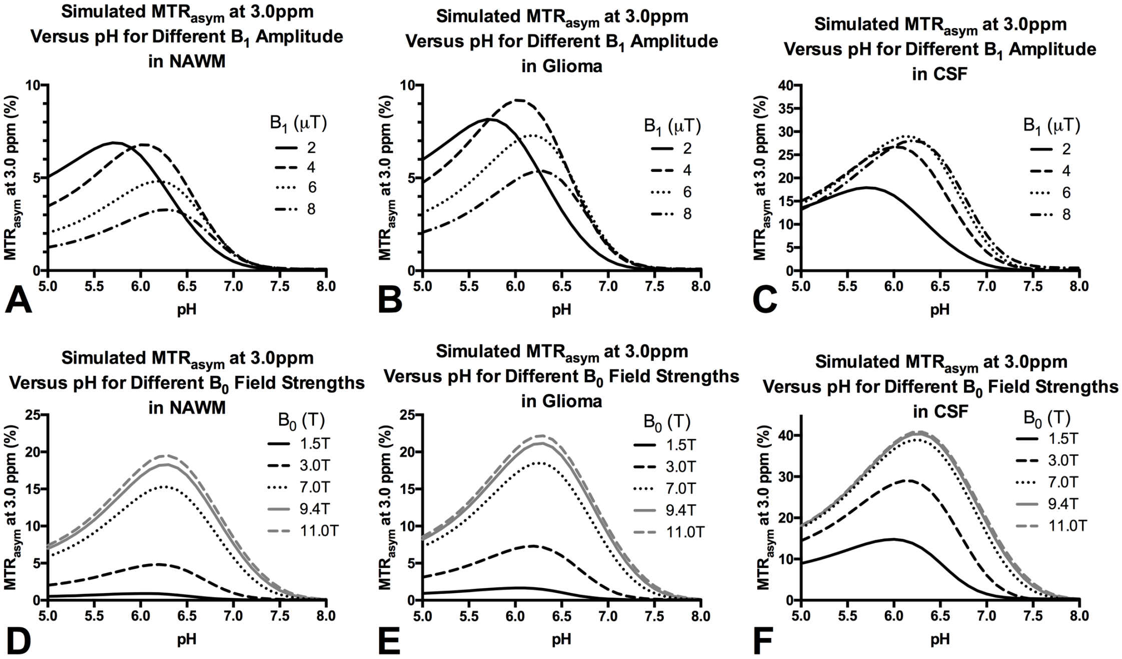

Figure 13: (A-C) MTR$_{asym}$ as a function of pH for varying saturation pulse amplitude B_1 in (A) NAWM, (B) tumor, and (C) CSF. (D-F) MTR$_{asym}$ as a function of pH for varying B_0 field strength in (D) NAWM, (E) tumor, and (F) CSF.

Effects of Proton Relaxation Times

Increases in T_{1a} first increased and then decreased MTR$_{asym}$ at 3.0 ppm within the tested range (Figure 14A). Increases in T_{2a} resulted in increased MTR$_{asym}$ at low pH (Figure 14B). Varying the amine pool relaxation parameters T_{1b} and T_{2b} had a negligible effect on the asymmetry at values above 0.1 and 0.01 s, respectively (Figures 14C&D). However, as T_{1b} decreased to 0.01 ms and below, MTR$_{asym}$ increased at pH values below approximately 6.5 (Figure 14C). Conversely, as T_{2b} decreased to 0.001 s and below, MTR$_{asym}$ decreased and eventually no longer increased with decreasing pH within a physiologically relevant pH range (Figure 14D).

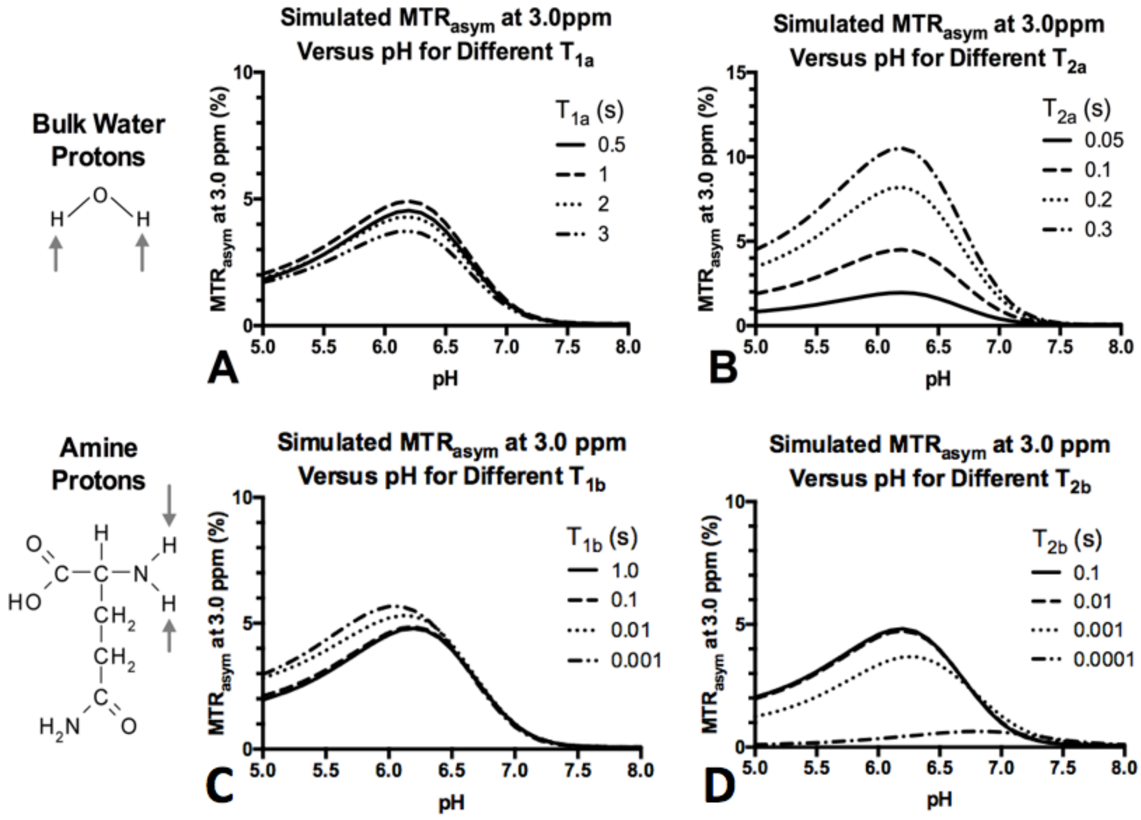

Figure 14: MTR$_{asym}$ as a function of pH for (A) varying T_{1a}, (B) varying T_{2a}, (C) varying T_{1b}, and (D) varying T_{2b} with NAWM relaxation times used as the baseline.

Effects of Amine Concentration

When varying the amine concentration, MTR$_{asym}$ increased with increasing concentration (Figures 15A-C). The slope between MTR$_{asym}$ and concentration decreased with increasing concentration, particularly for tissues with longer relaxation times (Figures 15D-F).

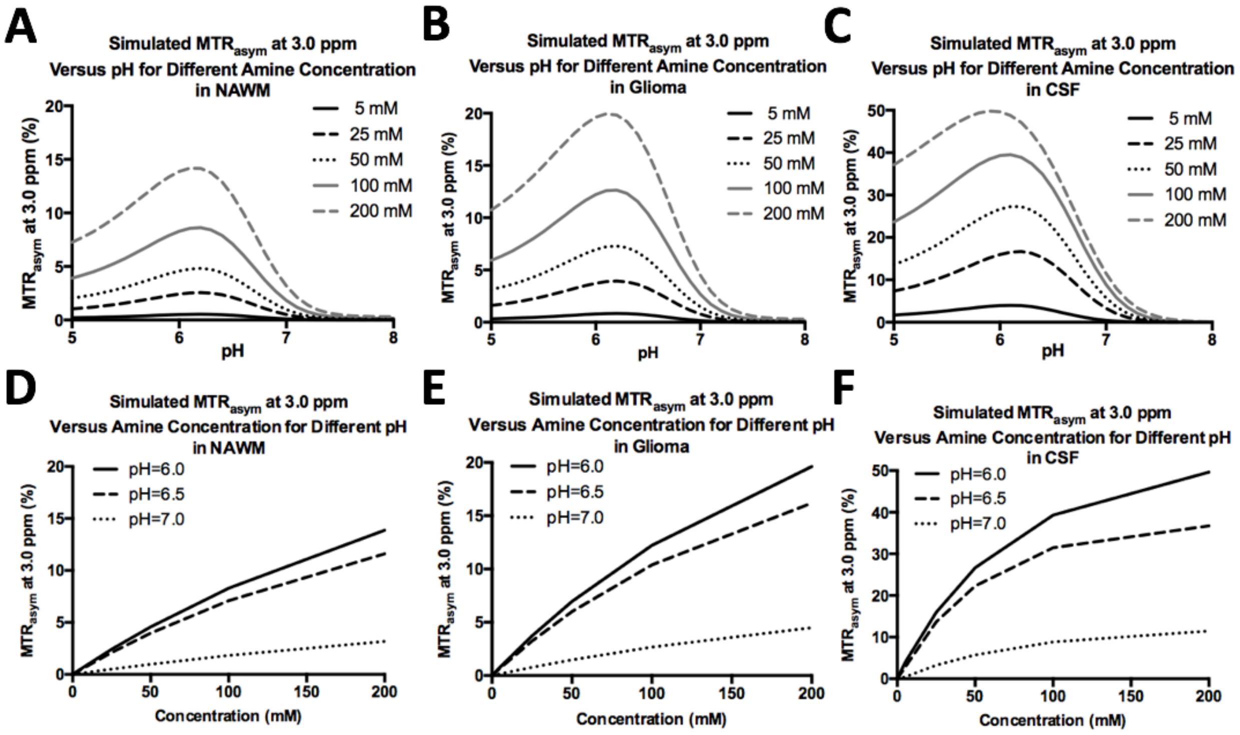

Figure 15: (A-C) MTR$_{asym}$ at 3.0 ppm as a function of pH for varying amine concentration in (A) NAWM, (B) tumor, and (C) CSF. (D-F) MTR$_{asym}$ at 3.0 ppm as a function of amine concentration at three pH values, as calculated from the data in (A-C).

v. Discussion

Results from this study provide a theoretical basis for using CEST MRI targeted to the amino acid amine group for pH-weighted imaging in tissues, and show the effects of clinical scan parameters on the resulting contrast. A significant finding of this study is that inputting a single value of B_1 into the Bloch-McConnell equations does not optimize the CEST contrast that can be achieved in terms of MTR$_{asym}$, and that unless the clinical sequence is utilizing a rectangular pulse rather than the more common Gaussian or *Sinc3* pulses for saturation, simulations that do not incorporate the true pulse waveform will produce erroneous results. To our knowledge, this study is the first to simulate CEST z-spectra with a non-rectangular saturation pulse for pH-weighted imaging.

Previous studies have implemented simulations of CEST spectra to test the effect of pulse parameters on the resulting measurements. Woessner et al. were among the first to describe the Bloch-McConnell equations under off-resonance irradiation in the context of CEST imaging [33]. However, this method uses a constant value of ω_1, which is likely not the pulse shape applied by the scanner. Zaiss et al. used an eigenvector solution of the Bloch-McConnell equations to simulate CEST and chemical exchange spin-lock (CESL) experiments [83, 84]. While an eigenvector solution is useful for obtaining equations in which the irradiation parameters can be seen in an intuitive form, the assumptions required for these solutions may break down at short irradiation times. Jin et al. also used an eigenvector solution of the Bloch-McConnell equations to describe CEST and CESL in a similar fashion [74, 96]. Sun et al. described an expansion of the two-pool CEST model to an arbitrary number of pools, but uses a constant value of ω_1 [81]. Our simulation has the potential to be scaled in a similar way as described by Sun. Sun et al. have also described the dependence of CEST-EPI on repetition time, duty cycle, and flip angle [82]. However, this study was performed for creatine imaging rather than amino acid amine imaging, which has a different relationship between pH and CEST contrast; a constant value of ω_1 was used in this study as well. Xiao et al. were one of the few groups to implement a shaped Gaussian pulse in the context of creatine imaging [97]; however, this study did not compare the effects of accurate modeling of the RF saturation pulses among different pulse shapes.

This study demonstrated that a saturation pulse train utilizing 100 ms pulses is ideal for saturation of fast-exchanging amines in tumor, and that a pulse train length of 3x100 ms pulses should be used to obtain 90% of the available pH-weighted contrast in all brain tissues. Our results further showed that TR should be minimized for CEST-EPI sequences to obtain maximum pH-weighted contrast. Using these parameters allows for collection of 29 z-spectral images and one S_0 image with full brain coverage in under 5 minutes of scan time, which is reasonable for clinical implementation.

We also demonstrated that the RF saturation pulse amplitude must be at 4 μT or above to obtain optimal pH sensitivity within a physiologically relevant range (6.0-7.4). Although the maximum MTR_{asym} at low pH (<6.5) was greater for 4 μT than 6 μT in tissues, the pH sensitivity is approximately equal down to pH values of 6.5. Because the optimal saturation pulse amplitude appears to increase with increasing relaxation times, an amplitude of 6 μT may still be ideal for ensuring that acidic regions of edematous tissue with long relaxation times can still be optimally identified.

Our results suggested that scanner B_0 field strengths should be 3.0T or above for effective pH-weighted imaging. These findings are in line with previously acquired phantom data [15]. Changes in relaxation properties of the bulk water influenced the resulting MTR_{asym}, with an increase in T_{1a} first resulting in increased and then decreased MTR_{asym}. This is likely due to competing effects of saturation at both the target frequency (+3.0 ppm) and control frequency (-3.0 ppm) used to calculate MTR_{asym}. This suggests that doing CEST imaging after injection of gadolinium contrast agent should be avoided, as the contrast agent will alter the T_{1a} characteristics of the tissue, possibly in a time-dependent manner as the contrast agent bolus passes through the tissue. An increase in T_{2a} resulted in increased MTR_{asym}, likely due to a narrowing of the bulk water peak and therefore less indirect saturation at the target and control frequencies. These results indicate that a correction for T_{1a} and T_{2a} relaxation times may be warranted to move towards quantitative pH imaging, although this pH-weighted technique appears useful at all T_{1a} and T_{2a} values for differentiating acidic (6.2-6.9) from non-acidic (7.3-7.4) tissue pH. Changes in the relaxation times of the labile proton pool had minimal effect on MTR_{asym} at typical values of metabolite T_{1b} and T_{2b} (≥0.1 and ≥0.01 s, respectively). This indicates that so long as the metabolite proton relaxation times fall within this typical range, even if we do not know the exact relaxation rates and must rely on estimation, it will not have a significant effect on simulation results. However, as T_{1b} decreased to very low values (≤0.01 s), MTR_{asym} increased at low pH. Again, this is likely caused by reduced attenuation of the control frequency (-3.0 ppm) compared with the target frequency (+3.0 ppm) at low T_{1b}. At very low values of T_{2b} (≤0.001 s), MTR_{asym} decreased and eventually no longer increased with decreasing pH within a physiologically relevant range. This indicates that bound metabolites with very short T_2 relaxation times may not contribute to the CEST signal during pH-weighted imaging and only the signal from free metabolites will be measured.

Changes in the amine concentration did have an effect on the resulting pH-weighted contrast, with higher amine concentration resulting in higher values of MTR_{asym}. This indicates that a correction for amine concentration also may be warranted, although this remains difficult to measure on a voxel-wise basis. One approach may be magnetic resonance spectroscopy (MRS); several studies have implemented MRS to measure glutamate and glutamine concentrations in brain tissue [98-100]. Chemical shift imaging (CSI) can be used to obtain multi-voxel spectroscopic data throughout the brain, but even this technique often requires large voxel sizes (10x10x10 mm^3) compared to traditional MRI techniques [101]. Still, CSI targeted to glutamine and glutamate could be used to approximate amine concentration spatially throughout the region of interest, allowing us to correct for amine concentration and move towards a more quantitative measure of pH.

There were a number of limitations in this study. Our model incorporated only fast-exchanging amine protons at 3.0 ppm, while the CEST signal in biological tissues will have many contributing exchangeable protons, including the more commonly measured protein amide protons targeted with proton transfer (APT) imaging at 3.5 ppm [57]. However, it is difficult to estimate the exchange rates and concentrations of exchangeable protons on proteins or other large molecules, as many protons may be rendered unexchangeable by protein folding. This study has not incorporated other experimental factors such as varying signal-to-noise ratio (SNR) in the resulting images, which will decrease with decreasing S_0 signal intensity. This S_0 signal intensity will in turn decrease with TR and pulse train length as the longitudinal bulk water magnetization does not have time to fully recover between excitation pulses. Therefore, the desired amount of pH-weighting must be balanced with these factors to obtain clinical images of sufficient quality. Rather than being perfectly uniform, the true B_1 amplitude and flip angle may vary spatially throughout the imaging target due to imperfect RF power deposition. However, this technique will still provide pH-weighted contrast provided the B_1 amplitude is sufficiently high at all locations. Finally, we have simulated a non-selective saturation pulse train that saturated all slices during each repetition; sequences that implement a slice-selective saturation pulse train can be described using this model and setting $B_1 = 0$ μT for all repetitions except the one preceding readout, which will provide less available pH-weighted contrast.

In conclusion, a two-pool simulation of pH-weighted amine CEST contrast was implemented in healthy tissue, tumor, and CSF using the Bloch-McConnell equations. Results suggested optimal scan parameters for clinical pH-weighted imaging and showed that pulse shape must be input correctly into the model to obtain accurate results.

CHAPTER III

Pre-Clinical Imaging

Before novel therapies or techniques are applied in human patients, they are often implemented in animals to gather preliminary information about whether the technique will work. In the case of brain tumor imaging, a common pre-clinical technique is to implant tumor cells into mouse brain tissue and allow the mouse to grow an intracranial tumor. We can then apply chemotherapeutic agents and acquire imaging data on these mice, as well as obtain histology from the brain tissue. In this chapter, we describe some pre-clinical pH-weighted MRI data that were acquired in mouse glioma models.

Gradient Echo Imaging

A CEST sequence consists of a RF saturation pulse train followed by an excitation pulse and readout. However, several different types of readout can be used. For animal studies, we utilized a gradient echo (GRE) readout [102], a common and simple form of readout that employs a 90° excitation pulse followed by a reversal of the gradient polarity to generate an echo. With this design, one line of k-space is acquired per excitation pulse. Spoiler gradients are also applied just prior to the excitation pulse to destroy unwanted transverse magnetization. This readout scheme is preceded by the saturation pulse, which can vary depending upon the CEST application. A GRE readout is preferable to EPI for these purposes in the pre-clinical setting because small magnetic field inhomogeneities lead to significant distortion of an EPI image at the small measurement scales inherent to a pre-clinical MR system.

i. pH-weighted MRI in a Mouse Model

To test the efficacy of amine CEST as a pH-weighted biomarker using a preclinical 7T small animal MR scanner, female C57BL/6 mice (6–8 weeks of age) were evaluated. One C57BL/6 mouse was injected with phosphate buffered saline (PBS; control) while 9 C57GL/6 mice were injected with 2×10^6 GL261 glioma cells and allowed to grow for 14 days. All procedures and protocols used in the current study were approved by the UCLA Institutional Animal Care and Use Committee to ensure proper animal care. Mice were sedated with 1%–3% isoflurane under O_2/N_2 flow, and respiration was monitored. Mice were kept warm with water heated to 37° C circulated using a TP500 water pump (Gaymar Solid State). All images were acquired on a 7T Bruker Biospec system with a custom-built 2.2-cm RF birdcage coil. Each mouse was scanned for less than one hour. We collected a series of anatomical images as well as pH-weighted MR images in these mice. Pre- and post-contrast 3D T1-weighted anatomical images were collected using a 3D fast low flip angle acquisition technique. A 100 μL bolus of 0.1 mM Gd-DTPA (Magnevist) was injected intravenously via tail vein prior to post-contrast imaging. Prior to contrast administration, pH-weighted CEST data were collected using a 2D GRE acquisition technique. Two spectral points were acquired, one at -3.0 ppm and one at +3.0 ppm. An S_0 image with no saturation pulse was also acquired for normalization. No additional spectral points could be acquired during this imaging session due to high throughput. Other CEST scan parameters were TE/TR = 6.9/2098 ms, FOV = 2x2 cm, matrix size = 128x128, bandwidth = 25 kHz, number of slices = 4, slice thickness = 1 mm, saturation pulse amplitude = 6 μT, saturation pulse length = 500 ms. The total CEST scan time was 10.5 min. Maps of MTR_{asym} were calculated using Eqn. 13.

As expected, T_1-weighted post-contrast and T_2-weighted images showed a large tumor burden in the tumor hemisphere. pH-weighted images showed avid contrast enhancement in the tumor hemisphere, although they did not coincide fully with tumor boundaries on T_1- and T_2-weighted images, indicating supplemental information. ROIs were manually drawn in the tumor regions as defined by enhancement on post-contrast T1-weighted images for nine GL261-tumored mice, with matching control regions drawn in the contralateral hemisphere. MTR_{asym} in the tumor region was significantly greater than that in the contralateral hemisphere as measured by a paired t-test (Figure 16E; $P=0.0002$). The mean tumor MTR_{asym} was 6.3% compared with 3.6% for contralateral tissue evaluated at a saturation frequency of 3.0 ppm in tumor, which was not observed in the control animal (Figures 16A&B). H&E histology confirmed that the areas showing an acidic signature were composed of relatively hypercellular, highly necrotic tumor tissue (Figures 16C&D).

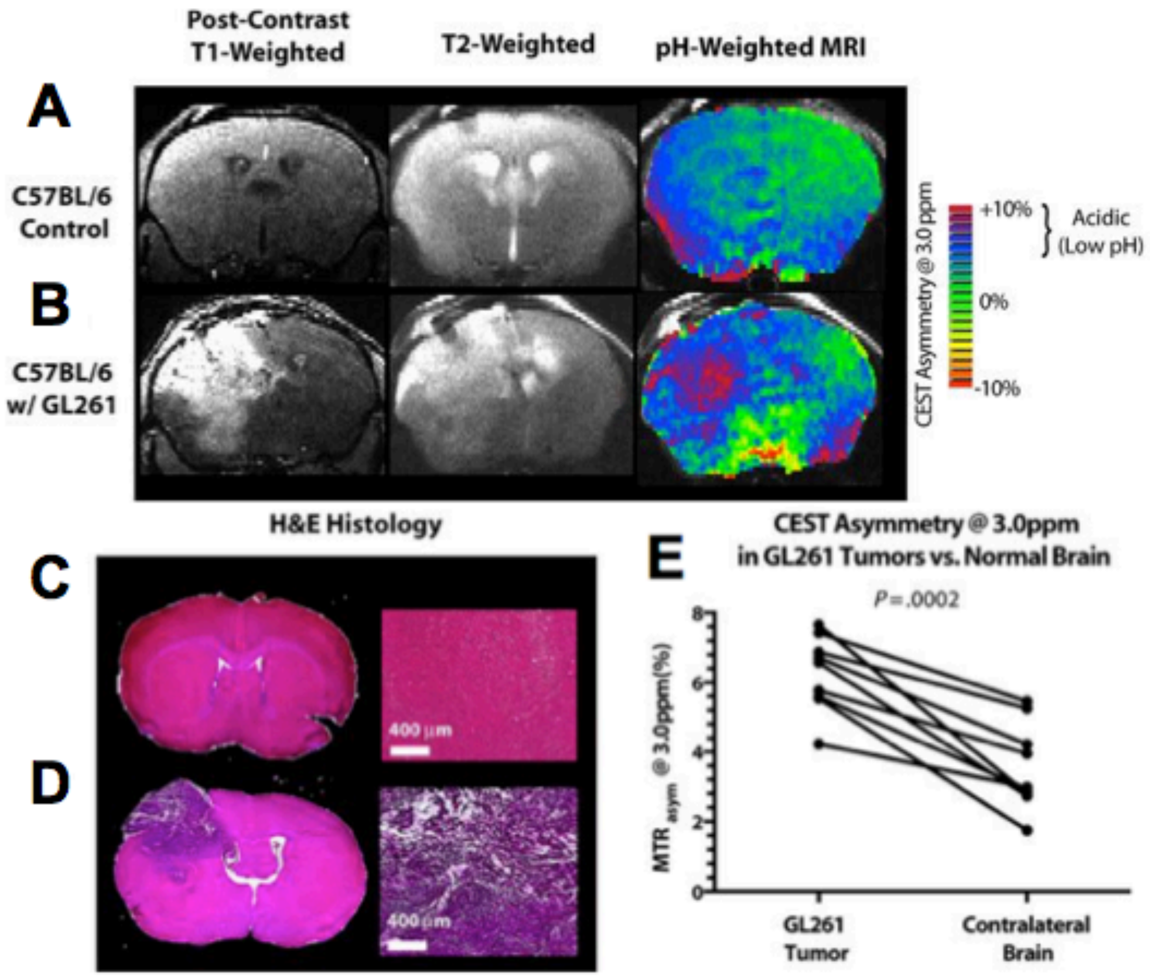

Figure 16. A) MRI data for a control mouse with no implanted tumor. B) MRI data for a mouse implanted with GL261 tumor cells, fourteen days post-implant. C) Matching H&E histology for the mouse shown in (A). D) Matching H&E histology for the mouse shown in (B). E) Tumor regions show significantly elevated pH-weighted contrast compared to contralateral tissue in mice. Adapted from [15].

ii. Dendritic Cell Immunotherapy

We then implemented pH-weighted MRI in a cohort of mice undergoing treatment with dendritic cell therapy and a programmed cell death protein (PD-1) inhibitor. Dendritic cell vaccination has been shown to initiate an immune response that activates T-cells, causing them to attack tumor cells [103]. However, this immune response is typically inhibited by PD-1 [104]. By also introducing a PD-1 inhibitor along with the dendritic cell vaccination, the immune response can proceed uninhibited. Previous data acquired by Antonios et al. [105] has suggested that dendritic cell vaccination in combination with a PD-1 inhibitor can extend survival in a GL261 mouse model (Figure 17). Therefore, we hypothesized that the activation of this immune response and subsequent improvement in tumor prognosis may happen alongside a reduction in acidity in the tumor microenvironment.

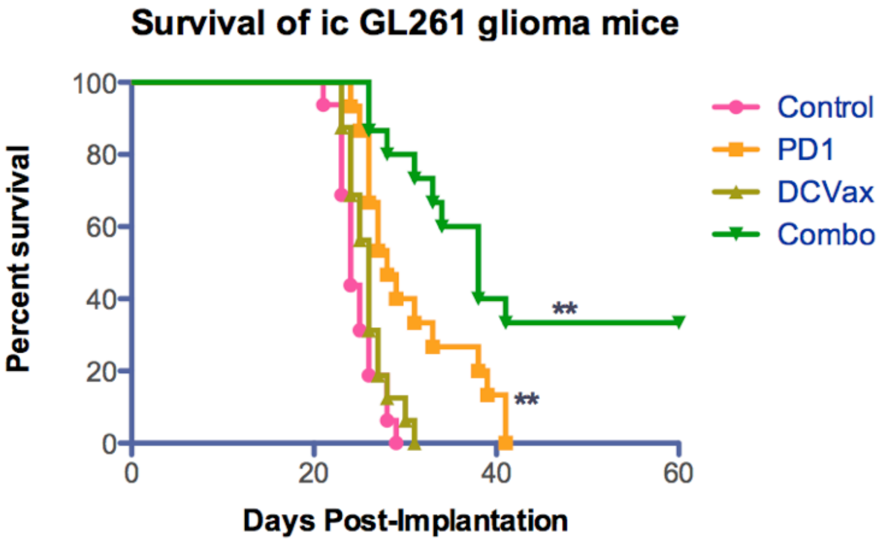

Figure 17. Overall survival data for mice with intracranial glioma treated with either saline, a PD-1 inhibitor, dendritic cell vaccination, or a combination of PD-1 inhibitor and dendritic cell vaccination. Mice in the combination group showed extended survival compared to the other groups [105].

To test this hypothesis, we implemented pH-weighted MRI in a cohort of mice divided into the same four treatment groups seen in Figure 17. Two mice from each group underwent imaging. The group receiving a combination of dendritic cell vaccination and PD-1 inhibitor showed reduced acidity compared to the other three groups (Figure 18).

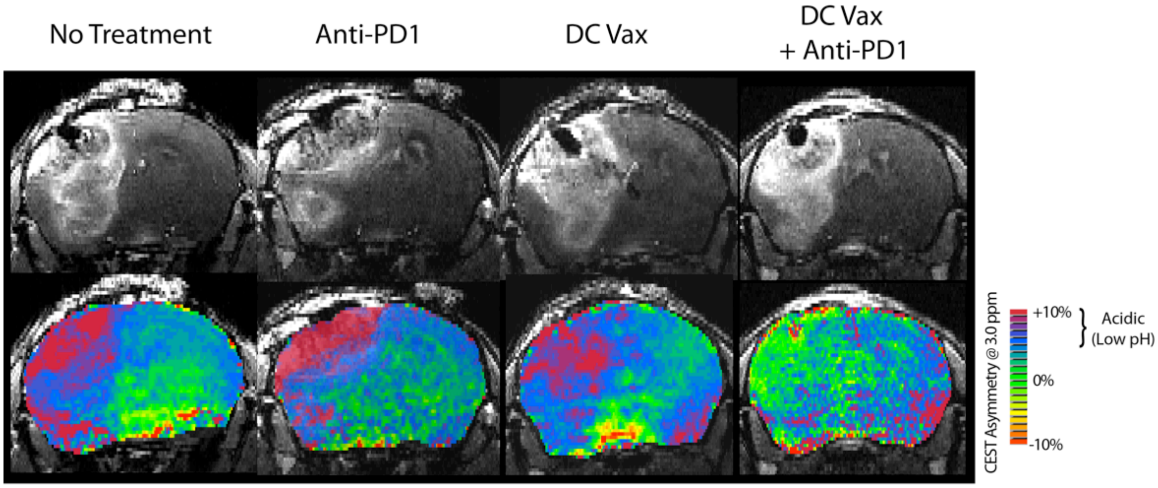

Figure 18. Post-contrast T1-weighted images and pH-weighted images for mice treated with either saline, a PD-1 inhibitor, dendritic cell vaccination, or combination therapy. Mice treated with the combination therapy show decreased pH-weighted image contrast within the tumor region.

As the groups that received combination treatment showed both increased survival and a decrease in acidity on pH-weighted images, these results provide evidence that pH-weighted MRI can be used as a biomarker for survival and treatment response.

iii. pH-weighted MRI and PET

Positron Emission Tomography (PET) is a molecular imaging technique in which a radiotracer fused to a metabolically active molecule is introduced into the imaging target. The molecule is then metabolized, trapping the radiotracer in the local tissue [106]. Tumor regions have been shown to have elevated PET tracer uptake using a number of different radiotracers. The most common radiotracer used in PET is fluorodeoxyglucose (^{18}F-FDG), a glucose analog [107]. Glucose is used as fuel for cells, and its uptake is elevated in highly metabolic tumors.

Therefore, it is of interest to see whether pH-weighted images and FDG uptake show similar regions of contrast.

A cohort of C57BL/6 mice with intracranial tumors grown from GL-261 glioma cells received PET imaging with ^{18}F-FDG, a subset (n=3) of which we were able to acquire our pH-weighted CEST sequence on in addition to standard anatomical MRI. Results showed an extremely large tumor burden with significant mass effect on anatomical T_2-weighted MRI (Figure 19). ^{18}F-FDG PET shows areas of increased metabolism around the periphery of the tumor. pH-weighted MRI appeared to show regions of elevated acidity corresponding to areas of increased FDG uptake. This may indicate elevated acidification in regions of high tumor metabolism. Although these results are interesting, a larger cohort of mice is needed for quantitative analysis of the relationship between pH-weighted imaging and PET in animal models.

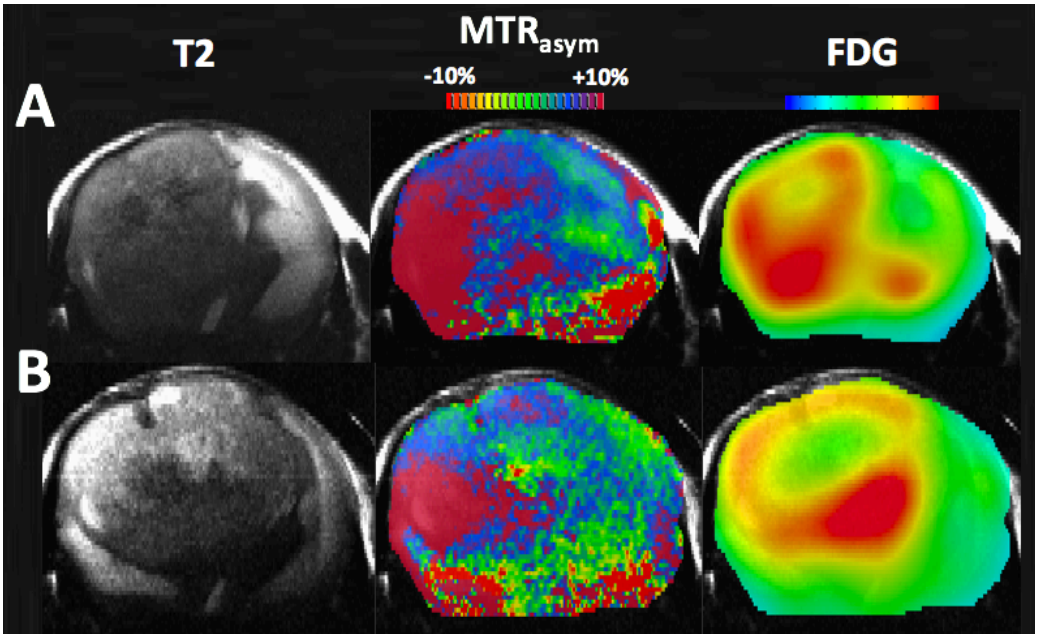

Figure 19. Imaging data for two mice (A&B) who received anatomical T_2-weighted MRI, pH-weighted MRI, and ^{18}F-FDG PET. Units of ^{18}F-FDG uptake are arbitrary and start at zero.

iv. In Vivo Measurement of pH in Glioma

One goal of our pH-weighted imaging development was to directly validate that image contrast is correlated with physical measurements of pH. However, direct measurement of pH *in vivo* is logistically difficult. Experimental measures of pH within human brain tissue cannot be taken for research purposes due to the invasive nature of the measurement. Some studies have proposed removal and homogenization of tissue in solution followed by measurement of solution pH [108, 109], though this likely results in destruction of the cellular membranes and a mixing of intracellular and extracellular protons, altering measured pH. Furthermore, as tissue is removed from the *in vivo* setting, its homeostatic properties quickly begin to change. Therefore, if possible, direct physical measurement of pH within the intact tissue is preferable for validation. To achieve this, we proposed pH-weighted imaging followed by *in vivo* measurement of pH in a mouse tumor model.

Imaging

Ten BL6 immunocompromised mice were implanted with 2.5×10^6 U87 glioblastoma cells at a depth of 2.0 mm. Tumors were allowed to grow until they appeared reasonably large on T_2-weighted images (approximately ¼ of total brain area at coronal slice of injection), which was approximately four weeks post-implant. Three mice died during this time and were removed from the study. Mice then underwent imaging on a 7T Bruker Biospin MRI system. Mice were sedated with 1%–3% isoflurane under O_2/N_2 flow; respiration and temperature was monitored. Mice were kept warm with water heated to 37° C circulated using a TP500 water pump (Gaymar Solid State). Each mouse underwent anatomical imaging consisting of a multi-echo spin echo (MESE) sequence for acquiring a series of T_2-weighted images. Parameters were

TR=2000 ms, TE=7.2 ms * echo number, 12 echoes, FOV = 2x2 cm, matrix size = 256x256, slice thickness 1 mm, slices = 11, bandwidth = 75757 Hz, total acquisition time = 6:32. pH-weighted imaging consisted of a series of CEST-GRE acquisitions with varying offset saturation frequencies. Scan parameters were TE/TR = 5.1/4084 ms, FOV = 1.5x1.5 cm, matrix size = 96x96, slice thickness = 1 mm, slices = 5, bandwidth = 37878 Hz, saturation pulse length 800 ms, saturation pulse amplitude 6 μT. Saturation offset frequencies of ±2.8, ±2.9, ±3.0, ±3.1, and ±3.2 ppm were acquired and an integral of the data points surrounding -3.0 and +3.0 ppm was calculated. An S_0 image was also acquired by setting B_1 = 0 μT and leaving all other parameters constant. MTR_{asym} was calculated as given by Eqn. 13. On the MTR_{asym} images, two targets were identified within the tumor hemisphere of each mouse: one target on the periphery of the tumor with moderately elevated MTR_{asym}, and one target within the core of the tumor in a region of more highly elevated MTR_{asym}. These targets were typically at depths of approximately 2.0 and 3.5 mm from the surface of the brain, although they varied in depth by approximately ±0.3 mm between mice. A circular ROI of 1.4 mm diameter was centered on each target on the slice containing the site of tumor implantation. The mean and standard deviation of MTR_{asym} within this ROI were calculated, with standard deviation used as the error in MTR_{asym}.

In Vivo pH Measurements

pH measurements were made using a needle-type optical pH microsensor probe (Presens Precision Sensing, Regensburg, Germany). This system utilizes a pH meter (Figure 20B) with detachable pH probes that house a fiber optic sensor within a needle sheath (Figure 20D). The pH probes can be mounted to a stereotactic micromanipulator for precision measurements in tissue (Figure 20A). Within two days prior to pH measurement in mice, each pH microsensor was calibrated using a series of phosphoric buffer solutions at pH values ranging from 4.0 to 9.0 to ensure accuracy.

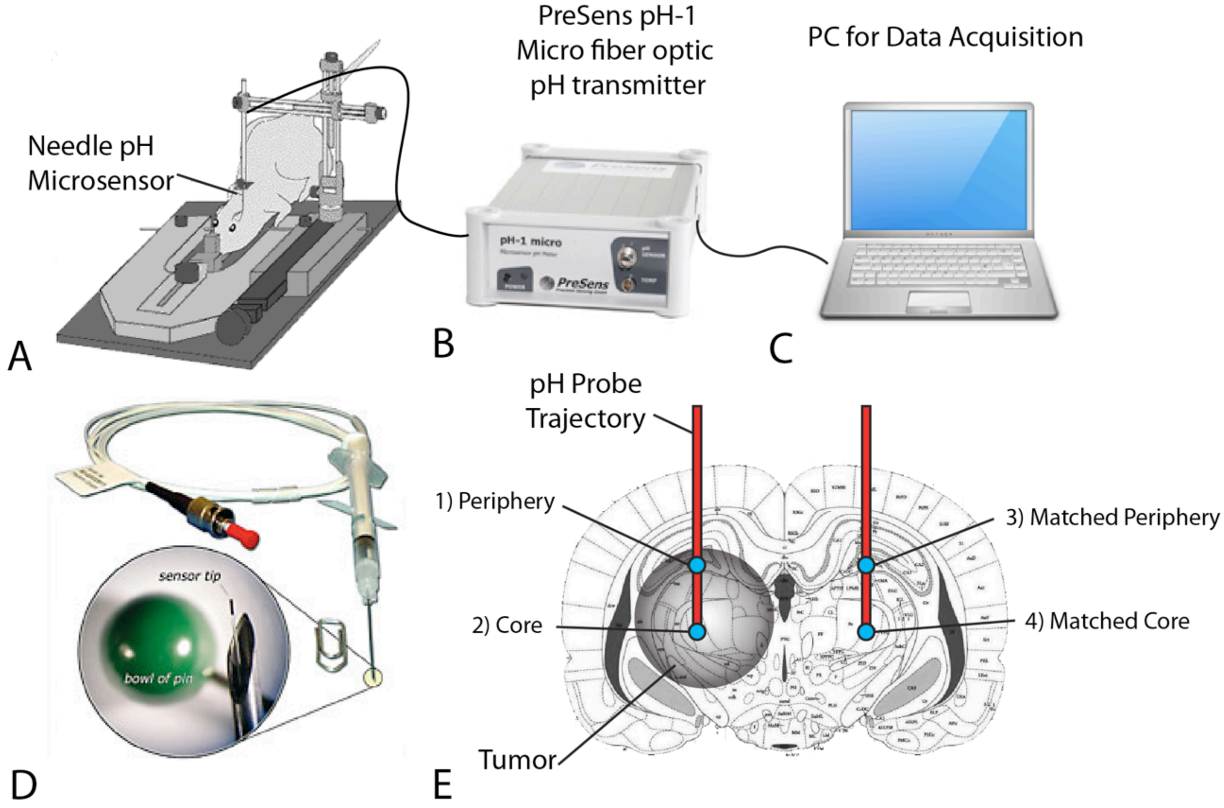

Figure 20. A) Anesthetized mice are held in place by a stereotaxic frame. B) Data is acquired by a pH meter in conjunction with C) software on a PC. D) A fiber optic needle-type pH microsensor for use with the pH meter. E) pH measurements are performed using locations identified on MRI, including the tumor periphery, tumor core, and normal tissue contralateral to both tumor hemisphere measurements.

Within 12 hours after imaging, mice underwent physical measurement of pH within the brain tissue. Mice were anesthetized with an intraperitoneal injection of ketamine (90 mg/kg) and xylazine (10 mg/kg) for non-survival surgery. After sedation, mice were placed on a stereotactic frame to minimize head motion. Bone wax at the site of the tumor implantation burr hole was removed, and the burr hole was re-drilled if necessary. A second burr hole was drilled contralateral to the tumor implantation burr hole to obtain contralateral measurements in normal brain tissue. The pH microsensor needle was positioned vertically above the mouse brain, perpendicular to the table surface. The needle was inserted into the brain tissue using the micromanipulator to the depth required by the selected targets (~2.0 mm, ~3.5 mm; Figure 20E). During measurement, the needle was retracted by the micromanipulator while the pH sensor remained in place to obtain readings. For each hemisphere, a measurement was first taken at the ~2.0 mm site and then secondly at the ~3.5 mm site without removing the needle from the brain tissue. Between hemisphere measurements and between mice, the needle sheath was retracted outside of any tissue and the microsensor tip was cleaned with distilled water. During measurement, readings were acquired every three seconds for a period of three minutes to allow the sensor readings time to equilibrate. For each measurement site, the final twenty readings (60 seconds) were used to calculate an average pH value for that location. The standard deviation of pH readings within these 60 seconds was taken as the error in pH. Two mice were excluded from analysis due to large bleeds that occurred prior to and during pH measurement.

Analysis

To determine the expected relationship between MTR_{asym} and pH for our pre-clinical pH-weighted sequence, the scan parameters used for this sequence (saturation pulse length = 800 ms, saturation pulse amplitude = 6 μT, pulse train length = 1, number of slices = 5, readout length = 17 ms, field strength = 7T) were implemented in our CEST simulation. Because our pre-clinical scanner utilizes a slice-selective rather than a non-selective preparatory saturation pulse, B_1 was set to zero during the first four repetitions. The simulated estimation of MTR_{asym} was plotted for pH values of 6.0 to 7.5. Experimentally measured values of MTR_{asym} were then compared to pH for both tumor periphery and tumor core measurements as well as their matching contralateral measurement in each mouse.

To determine whether pH was significantly decreased within the tumor compared with control tissue, a paired t-test was performed between the mean pH measurement in the tumor core and the matching contralateral target. A paired t-test was also performed between mean MTR_{asym} in the tumor core and the matching contralateral target.

Results

Comparisons of MTR_{asym} and measured pH are shown in Figure 21. Data appeared to be clustered either above or below the simulated curve. However, the measured data points in Figure 21 did not converge using a fit to our previously described simulation model, indicating a poor fit to the data.

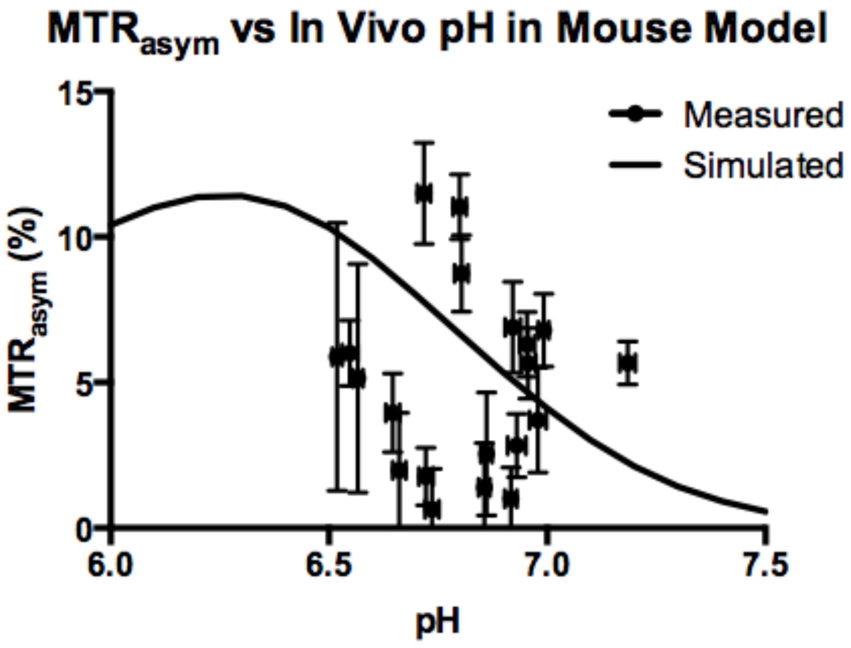

Figure 21. Experimentally measured values of pH within mouse brain as a function of pH-weighted image contrast (MTR$_{asym}$). Error bars are given by the standard deviation of the measurements of pH and MTR$_{asym}$. The simulated relationship between MTR$_{asym}$ and pH is shown by the solid line.

Results showed that pH was significantly lower within the tumor core than in matching contralateral tissue (Figure 22A, *P=0.035*), with a mean pH of 6.73±0.17 in the tumor core and 6.87±0.13 in the contralateral tissue. MTR$_{asym}$ was significantly higher within the tumor core than in matching contralateral tissue (Figure 22B, *P=0.0085*), with a mean MTRasym of 5.83±3.86% in the tumor core and 2.75±1.93% in the contralateral tissue.

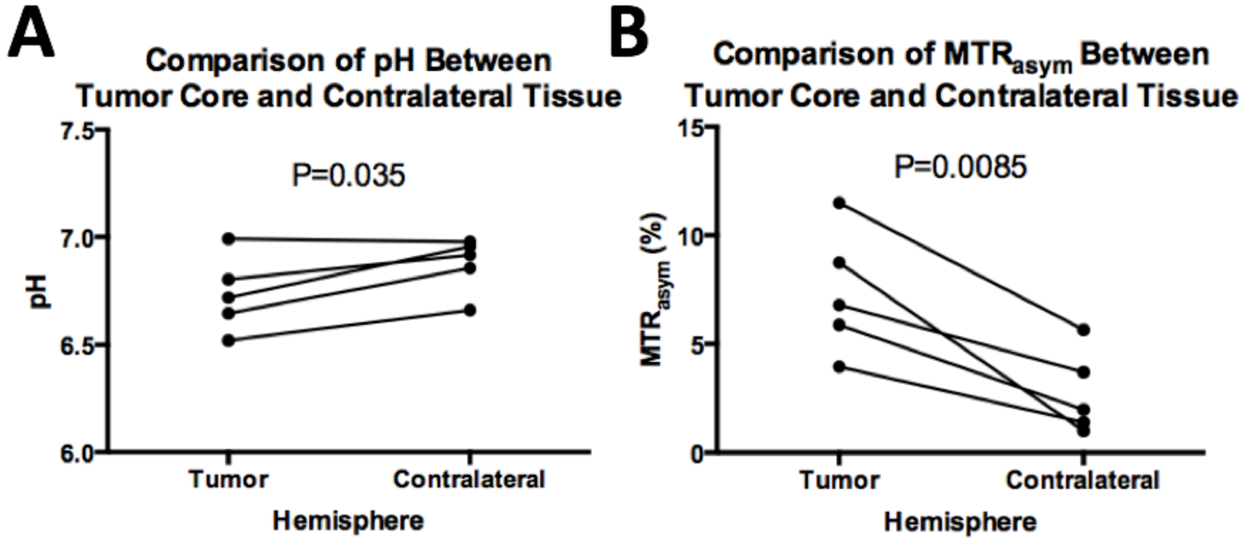

Figure 22. A) In vivo pH measured using a needle-type pH microsensor is lower within the tumor core than in matching contralateral tissue. B) pH-weighted image contrast is higher within the tumor core than in matching contralateral tissue.

Discussion

This study demonstrated the feasibility of measuring pH *in vivo* in an animal model. A handful of previous studies have attempted to measure the pH of brain tissue and glioma tissue *in vivo*. As described by Gerweck et al., Pampus et al. obtained electrode measurements of pH in glioblastoma and normal brain tissue in twenty human patients and found that pH was significantly lower in regions of glioblastoma [7]. That study found an average pH of 6.87±0.23 in glioblastoma and 7.14±0.26 in healthy tissue. Griffiths et al. compiled a number of studies that also used electrode measurements to obtain a pH range of 6.4 to 7.3 in human glioblastomas compared to 6.9 to 7.2 in healthy tissue [8]. Grant et al. constructed a fiber optic pH sensor and detected pH changes within rat brain during injection of sodium bicarbonate and during stroke [110]. However, to our knowledge, our study is the first to compare direct measurements of pH *in vivo* to pH-weighted image contrast on MRI.

As expected, a decrease in pH within the tumor core compared to contralateral tissue was observed, as well as increased pH-weighted contrast in the tumor core compared to contralateral tissue. However, the relationship between MTR_{asym} and pH did not yet yield a satisfactory concurrence with simulated results. There are a number of possible reasons for this outcome.

Anesthetic injection of ketamine and xylazine is often used for performing a nonsurvival surgery such as *in vivo* pH measurement. Previous studies have suggested a drop in brain tissue pH of approximately 0.10-0.16 pH units during ketamine/xylazine-induced anesthesia in mice [111, 112]. Conversely, administration of isoflurane such as that used during pH-weighted imaging has not appeared to cause a significant drop in brain tissue pH in mice [113, 114]. This indicates that differing anesthesia techniques may cause pH characteristics to be altered between imaging and physical pH measurement, leading to errors in our correlations. As such, reconciliation of anesthesia methods may be necessary in future studies. As the MRI protocol typically takes approximately one hour, repeated injection of ketamine/xylazine to maintain stable anesthesia would be difficult; the use of isoflurane during physical pH measurement would be preferred for consistency, as well as maintaining homeostatic pH.

Heterogeneous amine concentration through the normal tissue and tumor regions may also lead to variability in the measured pH-weighted CEST signal. As discussed in Chapter II, it may be possible to perform a correction for amine concentration by performing multi-voxel MR spectroscopy targeted to the glutamine/glutamate peak, although this technique suffers from poor spatial resolution and adds increased scan time.

During our measurements, the pH probe was carefully washed with distilled water between measurements of each hemisphere to remove any tissues from the sensor tip, while keeping it within the tissue for both the peripheral and core measurements of each hemisphere.

Since tissues were clearly seen on the probe tip before washing each time, it may be necessary to remove the probe after each measurement, rather than each hemisphere, to ensure that readings are not affected by tissues from another location.

In vivo pH measurements of brain tissue also have the potential to be affected by respiratory motion, ventricular pulsatile motion, blood flow, and high tissue heterogeneity, among other factors. Respiratory motion can be difficult to keep constant over the course of a twenty-minute experiment when using ketamine/xylazine anesthesia; using isoflurane instead during the physical pH measurement may aid in respiratory consistency in addition to the previously described benefits. Pulsatile motion and blood flow may lead to errors in pH readings that are unavoidable during *in vivo* experiments. Puncturing and damage to the tissue may lead to changes in pH at the site of measurement as well, although this effect is minimized by use of the thin needle-type probe.

For these reasons, intrinsic error in pH measurements is expected and therefore large sample sizes must be used to obtain sufficient statistical power for detecting correlations between image contrast and physically measured pH. Only half (5/10) of the mice included in this experiment could be used to obtain pH measurements due to either death from tumor burden or large bleeds during attempted measurement of pH. As such, the inclusion of a larger sample size is warranted during a repeat of this study. Additionally, error in this experiment can be reduced by using isoflurane anesthesia during physical pH measurement, by cleaning the probe tip following each measurement, and by acquiring spectroscopic data to correct for amine concentration.

CHAPTER IV

Human Studies

The end goal of developing new glioma imaging techniques is to obtain information that can serve as a biomarker for survival, treatment efficacy, or tumor characteristics in human patients. In this chapter, we first validate pH-weighted imaging on clinical scanners using amino acid phantoms and then describe the application of pH-weighted CEST MRI in human glioma patients and explore its capability to serve as such a biomarker.

i. GRE Pulse Sequence Development

As described previously, a GRE readout is a common method for acquiring MRI data. The first pH-weighted CEST sequence we implemented clinically utilized a GRE readout, similar to that used for pre-clinical imaging. A standard GRE sequence was modified using the VB-17, VD-13D, and VD-13A IDEAS platforms provided by Siemens (Siemens AG, Munich, Germany), which allowed us to implement this sequence on Siemens Trio, Prisma, and Skyra MR systems, respectively. Specifically, a CEST saturation pulse was added prior to GRE readout. Parameters such as the number of applied saturation pulses, saturation pulse length, saturation pulse amplitude, the deadtime between saturation pulses, the length of the post-saturation spoiling gradients, and the saturation offset frequencies applied were all made adjustable on the sequence interface for optimal user flexibility. The interface allowing this modification of the saturation pulse train parameters is shown in Figure 23.

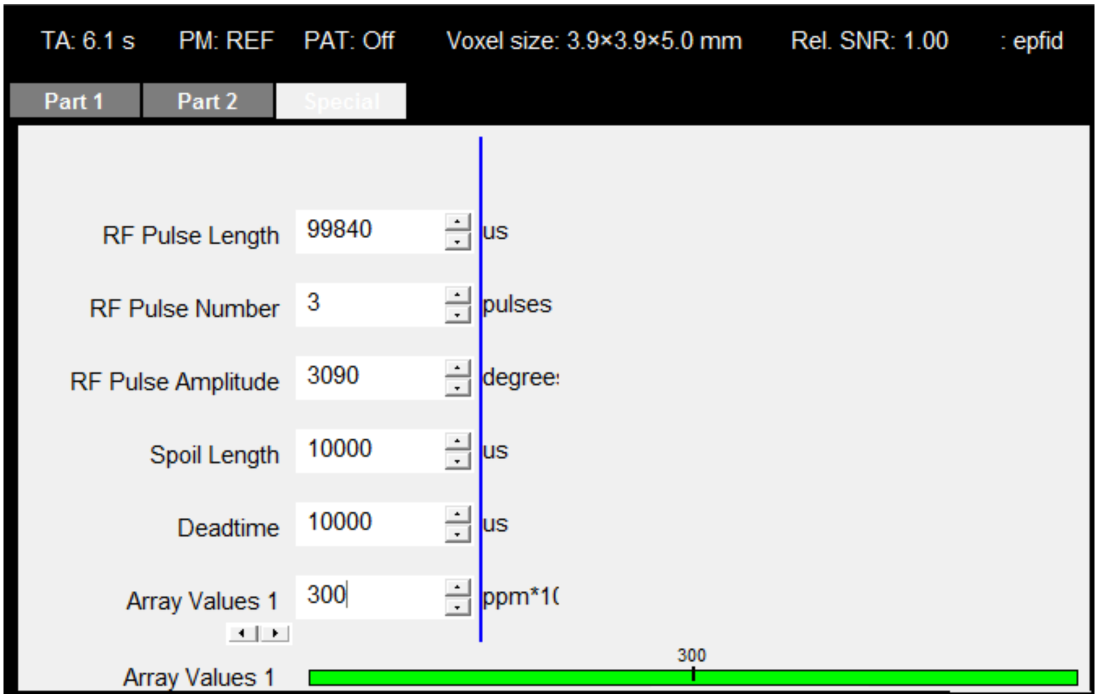

TA: 6.1 s PM: REF PAT: Off Voxel size: 3.9×3.9×5.0 mm Rel. SNR: 1.00 : epfid

RF Pulse Length 99840 us
RF Pulse Number 3 pulses
RF Pulse Amplitude 3090 degree
Spoil Length 10000 us
Deadtime 10000 us
Array Values 1 300 ppm*1
Array Values 1

Figure 23. An interface for customization of the CEST saturation pulse on clinical scanners (Siemens AG, Munich, Germany).

For the CEST-GRE sequence, we used a RF saturation pulse train consisting of 3x100 ms pulses and a deadtime of 10 ms for a total length of approximately 320 ms per pulse train. Since the readout portion of the GRE sequence is only ~15 ms, the majority of the total image acquisition time is a result of the saturation pulses. Because of clinical scan time limitations, tradeoffs are required to be made between the number of acquired spectral points and the number of image slices. Our choice of scan parameters within these limitations is described in further sections. A diagram of the CEST-GRE sequence is shown in Figure 24.

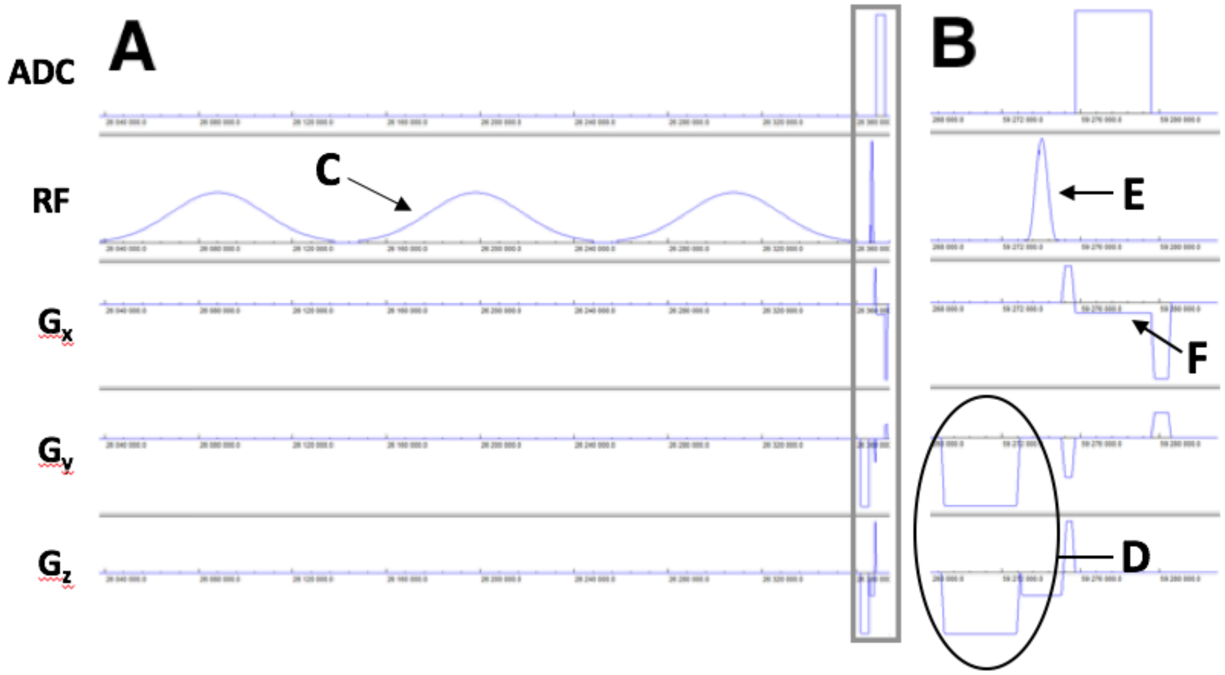

Figure 24. The CEST-GRE pulse sequence diagram, as simulated in POET on the VD-13D IDEAS platform (Siemens AG, Munich, Germany). The five rows shown in the pulse diagram represent the analog-to-digital converter (ADC), the RF amplitude (RF), and the gradient magnitude in the x-, y-, and z-directions (G_x, G_y, G_z). A) A single repetition of the saturation pulse and readout. B) A magnification of the readout portion, which is enclosed by the gray box in (A). C) The off-resonance RF saturation pulse train. D) Spoiling gradients to remove residual transverse magnetization before readout. E) A 90° excitation pulse. F) Readout of a single line of k-space.

ii. B_0 Inhomogeneity

In a real imaging experiment, the B_0 field will not be perfectly constant throughout the imaging sample. This causes issues when collecting CEST data as we are often measuring small signals at small spectral distances from the bulk water frequency. If the bulk water frequency in a particular voxel is shifted from 0 ppm, then we will not be measuring the spectral points we believe we are during a CEST acquisition. This problem can be amplified when taking asymmetry measurements around the bulk water peak, as both measurements will be inaccurate (Figure 25).

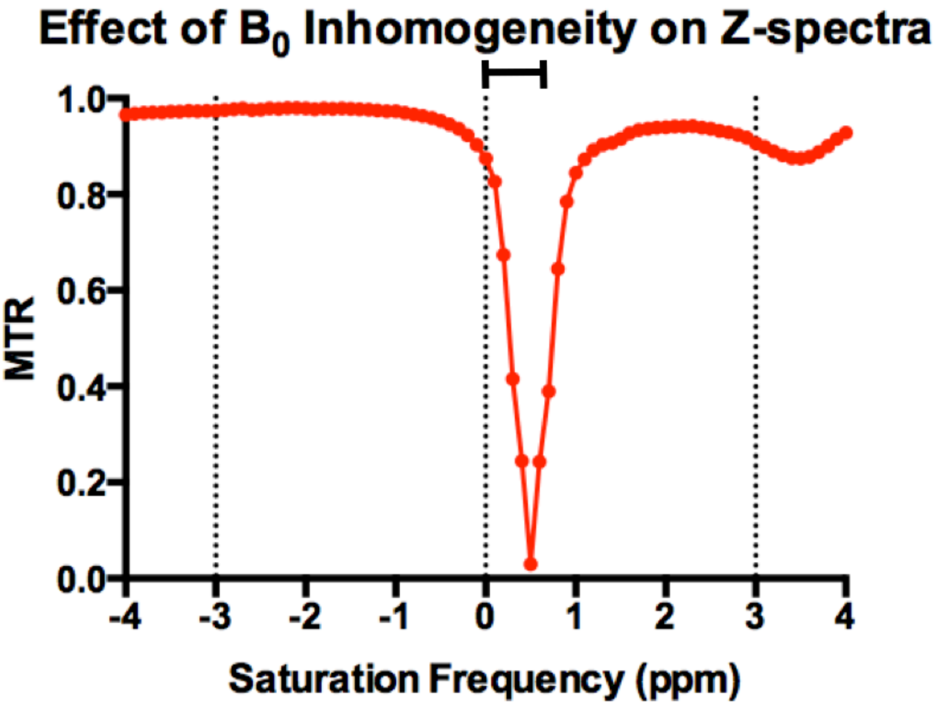

Figure 25. Z-spectra of glutamine dissolved in water for an image voxel with B_0 inhomogeneity. Inhomogeneity in an imaging sample at particular locations causes a proportional linear shift in the z-spectrum at those locations.

Fortunately, B_0 inhomogeneity only induces a linear shift in the z-spectrum. Because of this, if the inhomogeneity shift of each image voxel can be determined, the z-spectra can be corrected on a voxel-wise basis. This is typically done by collecting a number of spectral points in either direction around 0 ppm and determining the frequency of minimum signal intensity, which represents the true bulk water peak for that voxel [115]. The entire z-spectrum for a voxel can then be shifted so that this minimum is set to 0 ppm before asymmetry analysis is performed, as shown in Figure 26.

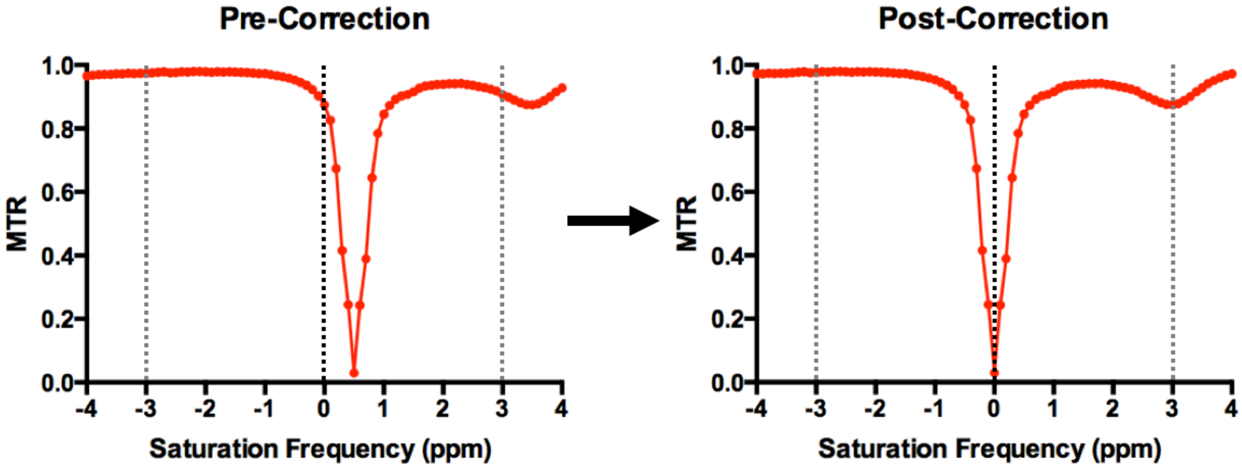

Figure 26. A voxel's z-spectrum is linearly shifted to set the bulk water peak at 0 ppm. Prior to correction, the measured spectral points of ±3.0 ppm would not have accurately measured the asymmetry. After correction, the proper measurement can be obtained.

In phantom samples with no time limitations, we can easily collect as many images as necessary to create a full z-spectrum with high spectral resolution. However, in clinical applications, there is a limit to the number of spectral points that can be acquired within a reasonable scan time. Because of this, data can sometimes only be collected at and around the frequencies of interest (ω, -ω), in addition to around the bulk water peak. In these cases, interpolation must be performed between the acquired data points to correct for the B_0 inhomogeneity shift. Many studies have reduced the number of spectral points collected around ω and -ω to three, a technique called the three-point method [68]; however, better spectral resolution is preferred. As is the case with all MRI sequences, the number of spectral points acquired must be balanced with image resolution, number of slices, number of averages, and other imaging parameters to fit within a clinically feasible scan time.

iii. Phantom Preparation and Imaging

In order to determine the dependence of glutamine CEST on pH and concentration, we prepared 50 mL samples of 25 mM, 50 mM, and 100 mM glutamine in distilled water. For each concentration, 24 samples at different pH varying from 4.0 to 8.6 in intervals of 0.2 were created by titrating 0.1 M HCl or NaOH and using a pH meter accurate to 0.1 pH units. In order to demonstrate that this effect is similar for other neutral amino acids, we prepared a similar set of samples using 100 mM glycine dissolved in distilled water at pH values 4.0–8.6 in units of 0.2, and a set of samples with 100 mM phenylalanine dissolved in distilled water at pH values 4.0–8.6 in units of 0.2.

Due to the large number of samples evaluated, each set of 24 vials with various pH values was split into 3 scans of 8 samples each. The samples were held stationary in a bath of room-temperature water (21°C). For each set of samples, 51 *z*-spectral points were acquired from −5.0 ppm to +5.0 ppm in units of 0.2 ppm. A saturation pulse train consisting of fifteen 100-ms pulses at an amplitude of $B_1 = 2.0$ µT was applied, followed by a 90-degree excitation pulse and GRE readout. Additionally, we explored the CEST effects for various field strengths using a 1.5T Siemens Avanto human MR scanner, a 3T Siemens Trio human MR scanner, and a 7T Bruker Biospec pre-clinical MR scanner.

iv. CEST Post-Processing and Analysis

All CEST data were motion corrected and inhomogeneity corrected prior to analysis. Motion correction was performed using the *mcflirt* function in FMRIB Software Library (Functional Magnetic Resonance Imaging of the Brain; http://www.fmrip.ox.ac.uk/fsl/). Inhomogeneity correction was performed as described previously. For the phantom experiments, a circular region of interest was drawn on each sample and the mean value for each spectral point was calculated to obtain the average *z*-spectra for a sample. $\mathrm{MTR_{asym}}$ at 3.0 ppm was calculated from these *z*-spectra for each sample.

Although the relationship between pH and the resulting CEST signal as described by the Bloch-McConnell equations is quite complicated, the values of $\mathrm{MTR_{asym}}$ at 3.0 ppm within a physiologically relevant pH range (6.0-7.4) resemble a sigmoidal curve with high signal at low pH values and low signal at high pH values, as seen in Chapter II. This type of curve can be described by a simple competitive inhibitor equation:

$$MTR_{asym}@3ppm(pH) = \alpha + \frac{\beta - \alpha}{1 + 10^{\delta(\kappa - pH)}} \tag{18}$$

where α is the $\mathrm{MTR_{asym}}$ at 3.0 ppm for high pH environments, β is the $\mathrm{MTR_{asym}}$ at 3.0 ppm for low pH environments, δ is the sensitivity of $\mathrm{MTR_{asym}}$ at 3.0 ppm to changes in pH, and κ is the pH required for 50% of the maximum span in $\mathrm{MTR_{asym}}$ measurements at 3.0 ppm between high and low pH limits. In this description, the “inhibition” is caused by a lack of CEST peak resolution at higher pH values. In order to test whether there was a difference in $\mathrm{MTR_{asym}}$ at 3.0 ppm as a function of pH between three different amino acids (glycine, glutamine, and phenylalanine), we applied Eqn. 18 to the pH-weighted data from the amino acids separately and tested whether the model parameters (α, β, δ, κ) varied significantly between amino acids.

The CEST *z*-spectrum in pH-varying samples containing glutamine illustrated reduced MTR during off-resonance irradiation around 3.0 ppm and asymmetry of the *z*-spectrum ($\mathrm{MTR_{asym}}$) increased with decreasing pH of glutamine solution (Figure 27), which is consistent with the expected CEST contrast of amine protons on the glutamine molecule undergoing chemical exchange with bulk water.

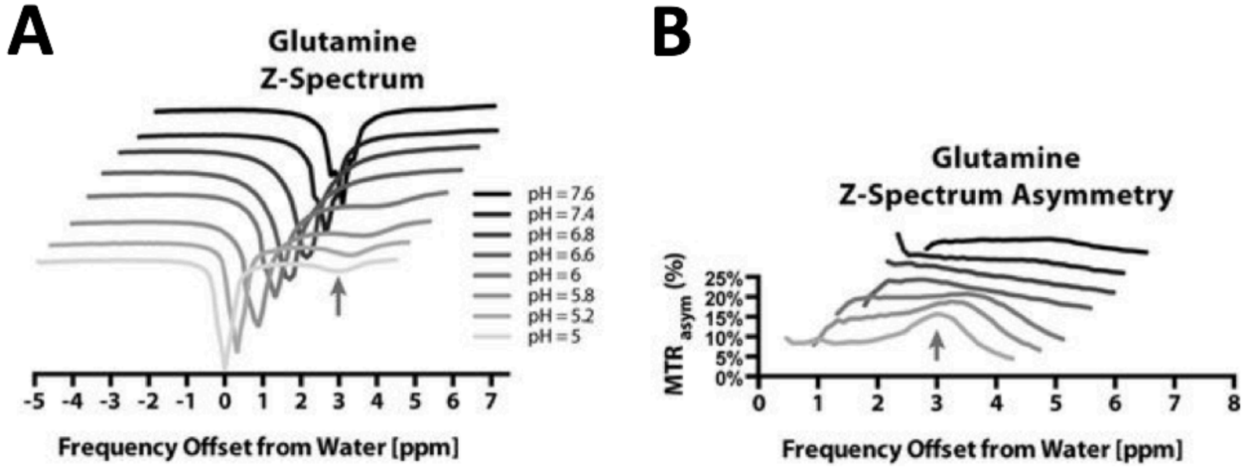

Figure 27. A) A CEST peak at 3.0 ppm increases in size with decreasing pH for 100 mM glutamine in a water solution. B) MTR_{asym} calculated from the data in (A). [15]

This CEST effect and pH-dependency around amine proton resonance also increased with increasing glutamine concentration (Figure 28). As the expected amino acid concentration in normal brain is ~20–25 mM [91], and other similar fast-exchanging amine groups will give rise to additional signal at 3.0 ppm, CEST signal due to these amine protons should be detectable *in vivo*.

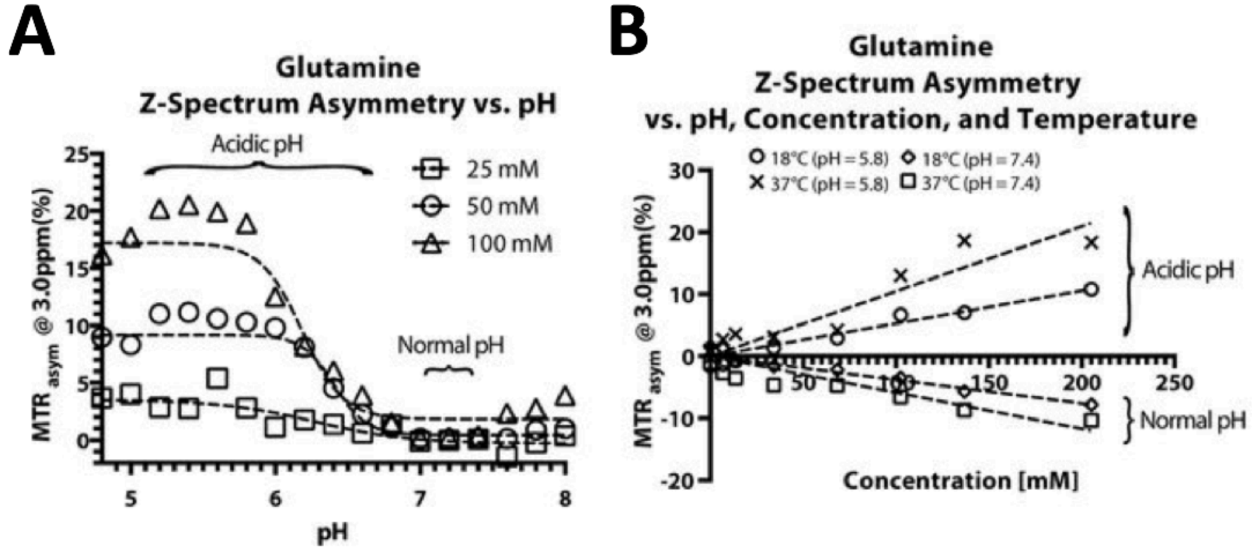

Figure 28. A) The CEST signal increases with decreasing pH and with increasing concentration of glutamine in water solution. B) The dependence of the CEST signal on pH, concentration, and temperature. [15]

The sigmoidal relationship between MTR_{asym} and pH is similar to a cooperative (or inhibitory) exchange process and is consistent with the Bloch–McConnell equations, as shown by our simulations. Interestingly, we observed an apparent contradictory increase in MTR_{asym} at 3.0 ppm with increasing temperature (Figure 28B); this may be explained by the competing effects from spin-spin relaxation (i.e. T_2 relaxation rate), which increases with increasing temperature, reducing the line width and increasing the available NMR signal at a given resonance frequency.

Results of the simple competitive inhibitor equation fit suggest no significant difference in the MTR_{asym} at 3.0 ppm for high pH values between the neutral amino acids (Figure 29; $P>0.05$ for all model parameters), supporting the hypothesis that pH dependence on the amine proton CEST signal is similar between amino acids due to the common backbone amine group they share.

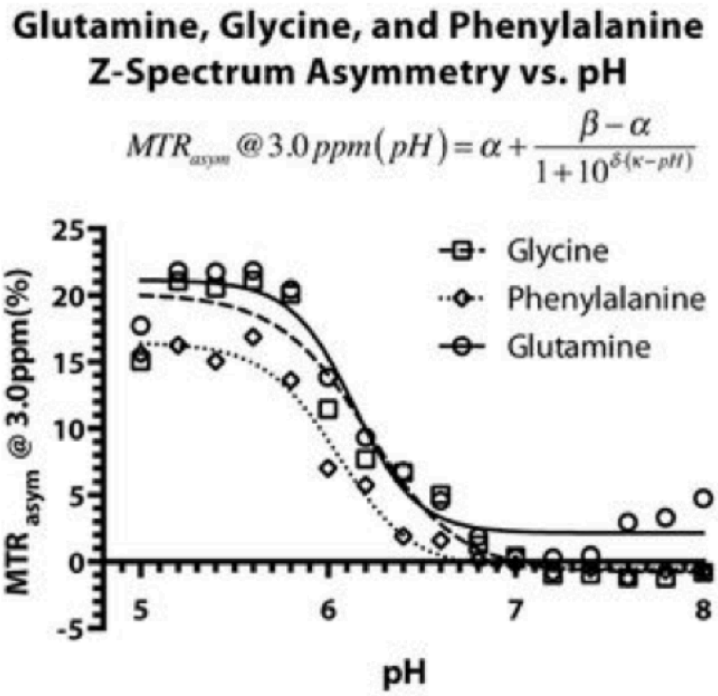

Figure 29. The relationship between MTR_{asym} and pH resembles a sigmoidal curve within a physiologically relevant range for three different amino acids [15].

Next, we explored the dependence of MTR_{asym} and pH on the MR scanner field strength. Using Equation 18 to describe the relationship between MTR_{asym} at 3.0 ppm and pH, results suggested that the pH required for 50% of the maximum span in MTR_{asym} at 3.0 ppm between high and low pH limits, or κ, was significantly lower on 1.5T scanners compared with both 3T and 7T, suggesting that 1.5T MR scanners may not provide adequate CEST signal for the range of pH values typically observed in tumors (Figure 30; nonlinear regression; κ for 1.5T vs 3T, *P=0.0012* and κ for 1.5T vs 7T, *P=0.044*).

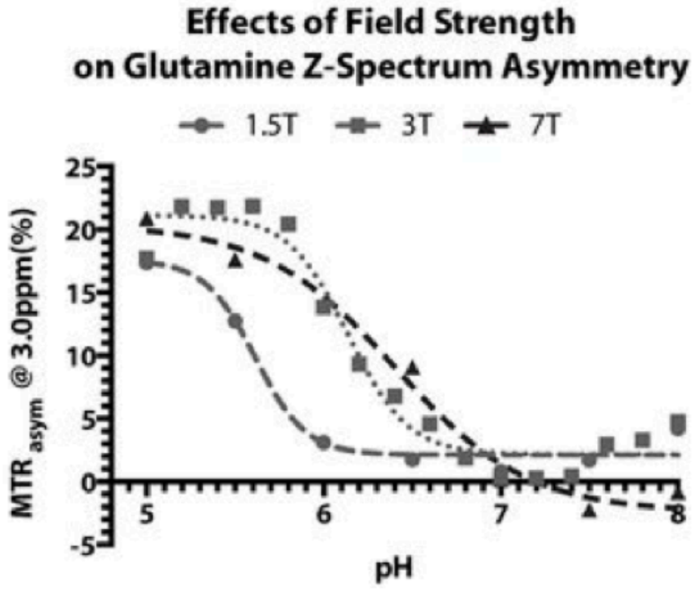

Figure 30. The effects of a scanner's magnetic field strength on the relationship between MTR_{asym} and pH [15].

Results also suggested that the relationship between MTR_{asym} and pH was similar between 3T and 7T scanners for all parameters besides the CEST asymmetry at high pH, which was slightly lower at 7T (Figure 30; Nonlinear regression; α, *P=0.7885*; δ, *P=0.1166*; κ, *P=0.1933*; and β, *P=0.0129*). Additionally, results suggested no difference in the actual sensitivity of MTR_{asym} at 3.0 ppm to changes in pH between the 3 field strengths (δ for 1.5T vs 3T, *P=0.7924*; δ for 1.5T vs 7T, *P=0.1470*, and δ for 3T vs 7T, *P=0.1166*) and no differences between the maximum MTR_{asym} at very low pH (α for 1.5T vs 3T, *P=0.2311*; α for 3T vs 7T, *P=0.7885*; and α for 1.5T vs 7T, *P=0.3422*). Together, these results suggest that pH-weighted MRI using endogenous amino acid CEST should be performed at high field strengths in order to ensure adequate contrast for the range of pH values commonly observed in cancer tissues.

v. pH-weighted Imaging in Human Gliomas

To test the hypothesis that an acidic microenvironment increases resistance to radiation and chemotherapies in human brain tumors, we acquired serial pH-weighted images in 20 patients with newly diagnosed glioblastoma who were treated with concurrent radiotherapy and temozolomide and examined differences in progression-free survival (PFS). All patients had histologically confirmed GBM (WHO grade IV), were compliant with the Health Insurance Portability and Accountability Act, and approved by the institutional review board at UCLA. Patients were evaluated at three time points: post-surgical and prior to radiochemotherapy (baseline); approximately 3 weeks after the start of radiochemotherapy (mid-treatment); and approximately 6–10 weeks after the start of radiochemotherapy or 0–4 weeks after completion of concurrent radiation and chemotherapy (post-treatment). All glioblastoma patients evaluated underwent maximal surgical resection followed by standard treatment with radiotherapy and concurrent temozolomide. Follow-up scans were also obtained in these patients for comparison and radiographic response as determined by the RANO criteria [116].

Clinical Scan Parameters for CEST-GRE

For the clinical CEST sequence used for serial glioblastoma imaging, we acquired 51 spectral points from -5.0 ppm to +5.0 ppm in units of 0.2 ppm. A saturation pulse train of three 100 ms pulses of amplitude $B_1 = 2.0\ \mu T$ was applied prior to GRE readout. An S_0 image was also acquired with $B_1 = 0\ \mu T$ for normalization. Because of clinical time constraints, only one 6 mm slice of image data could be collected. Other scan parameters for the CEST sequence were TE/TR = 2.7/3000 ms, FOV = 300x300 mm, matrix size = 128x128.

These patients also underwent standard clinical imaging consisting of pre- and post-contrast T_1-weighted images, T_2-weighted fluid-attenuated inversion recovery (FLAIR) images, diffusion tensor imaging (DTI), and a dynamic susceptibility contrast (DSC) acquisition. Scan parameters for the T_1-weighted images were TE/TR = 3.6/2100 ms, slice thickness = 1 mm, matrix size = 256 x 200, and FOV = 256 x 200 mm. Scan parameters for FLAIR images were inversion time (TI) = 2500 ms, TE/TR = 85/9000-10810 ms, slice thickness = 3 mm, FOV = 240x240 mm, and matrix size = 320x224. DSC scan parameters were TE/TR = 23/1250 ms, flip angle = 30°, slice thickness = 5 mm, number of slices = 20, matrix size = 128x128. Prior to DSC acquisition, a 0.025 mmol/kg pre-load dose of Gd contrast agent was administered to diminish the T_1 effects of contrast agent extravasation [117]. A 3- to 5-cc/s bolus of Gd-DTPA, administered at a dose of 10–20 cc (0.075 mmol/kg), was used in the acquisition of DSC as well as the subsequent post-contrast T1-weighted images (total of 0.1 mmol/kg). Parametric maps of cerebral blood volume (CBV) and cerebral blood flow (CBF) were calculated using commercially available post-processing software (IB Neuro v2.0, Imaging Biometrics) including contrast leakage correction [118]. DTI scan parameters were TE/TR = 90ms/7000ms, matrix size = 128x128, and b-value = 1000 s/mm^2 collected in 64 non-collinear directions. Additionally, six b=0 s/mm^2 reference images were acquired interleaved with the b=1000 s/mm^2 images. Maps of apparent diffusion coefficient (ADC) [119] were calculated from the DTI data using a monoexponential decay fit.

^{18}F-FDOPA PET and MR Spectroscopy

To demonstrate that CEST contrast at 3.0 ppm is elevated in human brain tumors under conditions where low pH is thought to occur, we assessed a subset of three high-grade gliomas

(WHO III–IV) using pH-weighted MRI, ^{18}F-FDOPA PET, and single-voxel MR spectroscopy. ^{18}F-FDOPA is an amino acid analog tracer that has shown sensitivity to regions of tumor and will be further described in Chapter V. ^{18}F-FDOPA PET scans were acquired using a high-resolution full-ring PET scanner (ECAT-HR; CTI/Mimvista). Patients were instructed to fast for more than 4 h prior to PET acquisition. ^{18}F-FDOPA was synthesized and injected intravenously, with injected doses averaging 125.4 ± 22.9 MBq, 1.54 ± 0.37 Bq/kg. 3D ^{18}F-FDOPA emission data were acquired 10 min after radiotracer injection for a total of 30 min. Data were integrated between 10 and 30 min from injection to obtain 20-min static ^{18}F-FDOPA images following reconstruction. PET images were reconstructed using an ordered-subset expectation maximization iterative reconstruction algorithm consisting of 6 iterations with 8 subsets [120, 121]. Lastly, a Gaussian filter with a full width at half maximum of 4 mm was applied. Uptake levels were normalized to the basal ganglia to highlight areas of abnormal ^{18}F-FDOPA uptake in the tumor. Parameters of single voxel MRS using PRESS were TE/TR = 30/1500ms, voxel size 3x3x3 cm. The presence of lactate was confirmed via inversion of the Lip/Lac peak in a 2nd echo by using an intermediate TE of 135 ms.

Stereotactic Image-Guided Biopsies and Tissue Processing

Stereotactic pH-image–guided biopsies were performed in two patients. Each patient's pH-weighted image was overlaid on the post-contrast T_1-weighted image for localizing of targets. When no contrast enhancing lesion was present, T_2/FLAIR images were used for target localization. The first patient was a suspected low-grade glioma biopsy patient. One region of elevated CEST contrast consistent with low pH and one region of low CEST contrast consistent with normal pH were biopsied. Standard hematoxylin and eosin (H&E) staining was performed as well as immunohistochemistry staining for Ki-67 and HIF1α expression. An H&E stain is the most commonly used stain in immunohistochemistry, causing the nuclei characteristics to appear different between healthy and tumor cells and allowing visualization of the presence of tumor within a tissue section [122]. Ki-67 is a protein that is present during all replicative phases of the cell cycle but is absent from resting cells, and is often used as a marker for tumor cell proliferation [123]. Hypoxia-inducible factor 1-alpha (HIF-1α) is a transcription factor that is upregulated in conditions of hypoxia. As such, it is often used as a marker for hypoxia in tumor tissue [124].

Sections of 5 microns were cut from formalin-fixed paraffin-embedded samples and processed for immunohistochemical detection of Ki-67 (Clone VP-RM04, rabbit monoclonal, 1:100 dilution, Vector Laboratories). Appropriate positive and negative controls were used to ensure good immunohistochemical staining. The second patient was a glioblastoma patient with suspected recurrence. Two regions of elevated CEST contrast consistent with acidic tissue and one region with low CEST contrast were biopsied, then H&E staining was performed and reviewed by a board certified neuropathologist blinded to the specific targets.

Comparison of Acidic Versus Non-Acidic Glioblastoma

In order to assess whether tumors with low pH signatures on CEST at baseline were more likely to have a shorter PFS after treatment with radiochemotherapy, we scored each tumor based on the amount of elevated CEST signal at 3.0 ppm. In particular, we defined “acidic” lesions as containing a substantial proportion (>50%) of positive CEST asymmetry at 3.0 ppm within areas of contrast enhancement and/or T2 or FLAIR hyperintensity. Alternatively, patients were scored as having “non-acidic” lesions if a significant portion of the lesion did not show an elevated

CEST signal. Next, we subjectively scored each lesion as “increasing” or “stable/decreasing” on pH-weighted MR scans before, during, and after radiochemotherapy in order to determine whether changes in the acidic lesion size could be used as an early response metric. Log-rank tests on Kaplan–Meier data were used to describe differences in progression-free survival (PFS) between these patient groups.

v. Patient Results

To test the hypothesis that an acidic microenvironment increases resistance to radiation and chemotherapies in human brain tumors, we performed pH-weighted imaging before, during, and after radiation therapy and temozolomide in 20 patients with newly diagnosed glioblastoma.

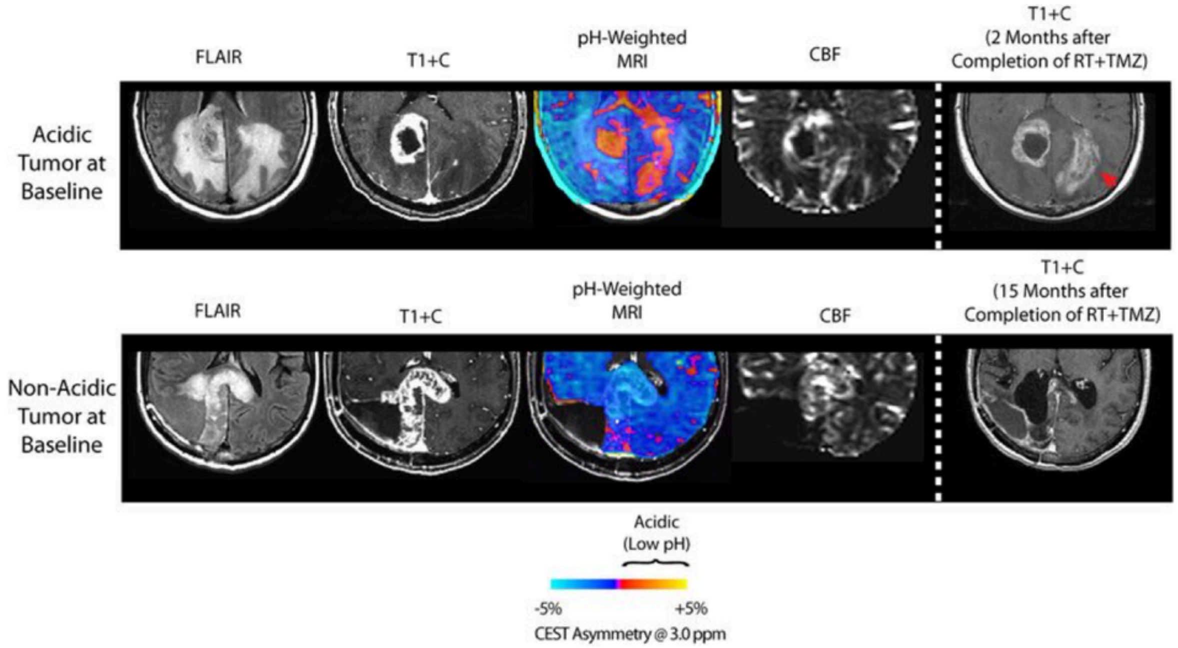

Figure 31. A) MRI data for a GBM patient who showed acidic tumor at baseline and recurred two months following completion of radiochemotherapy. B) MRI data for a GBM patient who did not show acidic tumor at baseline and remained stable 15 months following completion of radiochemotherapy. [15]

Qualitatively, areas with low pH at baseline often forecasted regions of subsequent tumor growth on contrast-enhanced MRI (Figure 31A). Although not completely co-localized, examination of CBF maps in these patients confirmed that regions with acidic signatures often occurred in areas of low perfusion, consistent with a high level of hypoxia.

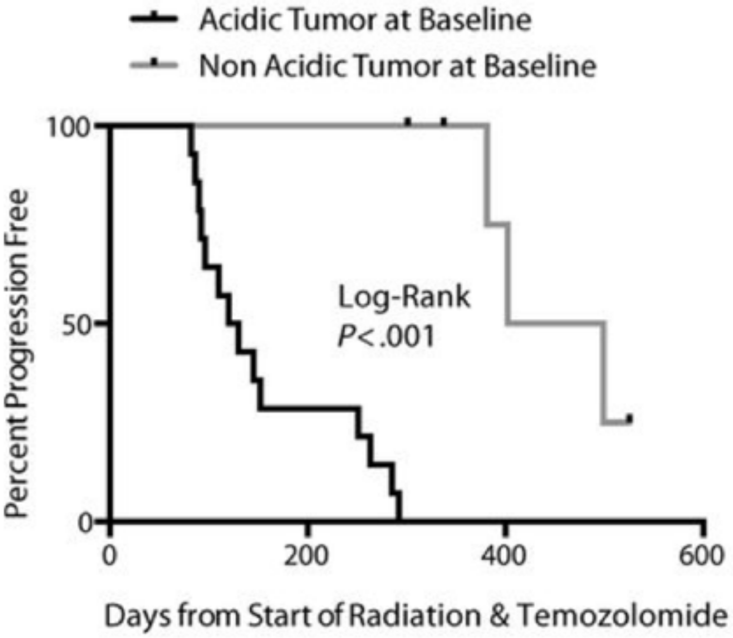

Figure 32. GBM patients with an acidic tumor at baseline (n=14) recur significantly faster than patients with a non-acidic tumor at baseline (n=6). [15]

Quantitatively, patients with tumors that were acidic at baseline following surgical resection but prior to radiation and temozolomide, as defined by a significant region (>50%) of positive CEST asymmetry at 3.0 ppm within areas of contrast enhancement and/or T_2/FLAIR hyperintensity, demonstrated a significantly longer PFS compared with patients lacking significantly acidic tumors (Figure 32; *log-rank,* P < *0.0001; median PFS for acidic tumors vs non-acidic tumors = 125 days vs 450 days*).

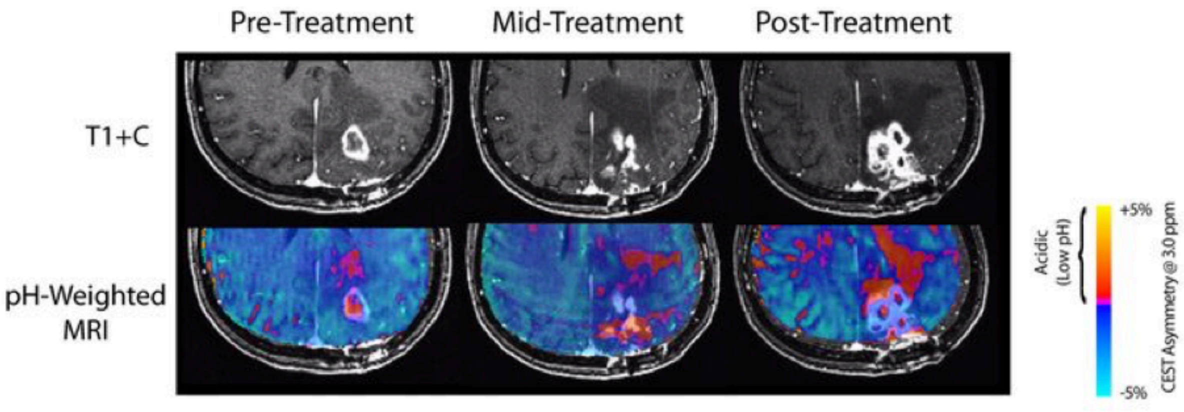

Figure 33. A GBM patient with increasing acidic lesion size, which appears to precede an increase in contrast-enhancing tumor burden in the same region. [15]

Additionally, patients exhibiting an increase in the size of acidic lesions during concurrent radiation and temozolomide therapy (Figure 33) had a significantly shorter PFS from the end of radiation therapy compared with tumors exhibiting stable or decreasing acidic lesion size (Figure 34; *log-rank,* P = *0.0003; median PFS in acidic growing tumors = 68 days vs 339 days*), implying that acidic tumor size may be useful as an early response biomarker in patients with glioblastoma.

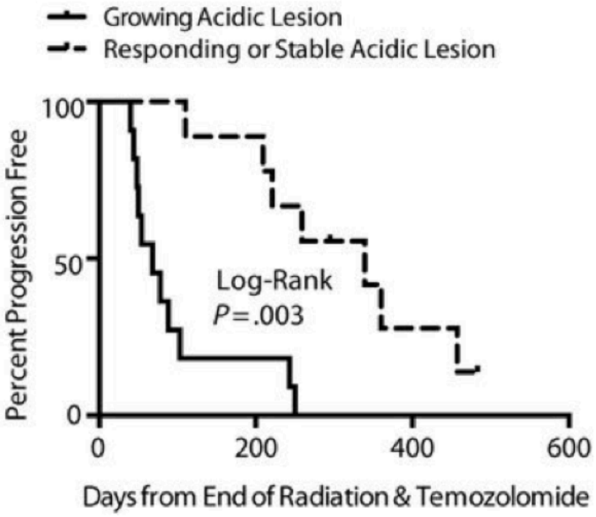

Figure 34. GBM patients with an acidic lesion that increases in size (n=11) recur significantly faster than patients with acidic lesions that remain stable or decrease in size (n=9). [15]

^{18}F-FDOPA PET and MR Spectroscopy

Results from high-grade glioma patients who also underwent ^{18}F-FDOPA PET and MRS demonstrated high MTR_{asym} in regions with elevated ^{18}F-FDOPA PET uptake and elevated lactate concentration (Figure 35), implying that highly aggressive tumors with elevated amino acid uptake for fuel and increased lactic acid in solution from oncologic metabolism under hypoxic conditions will consistently generate an acidic tumor signature using CEST MRI at 3.0 ppm.

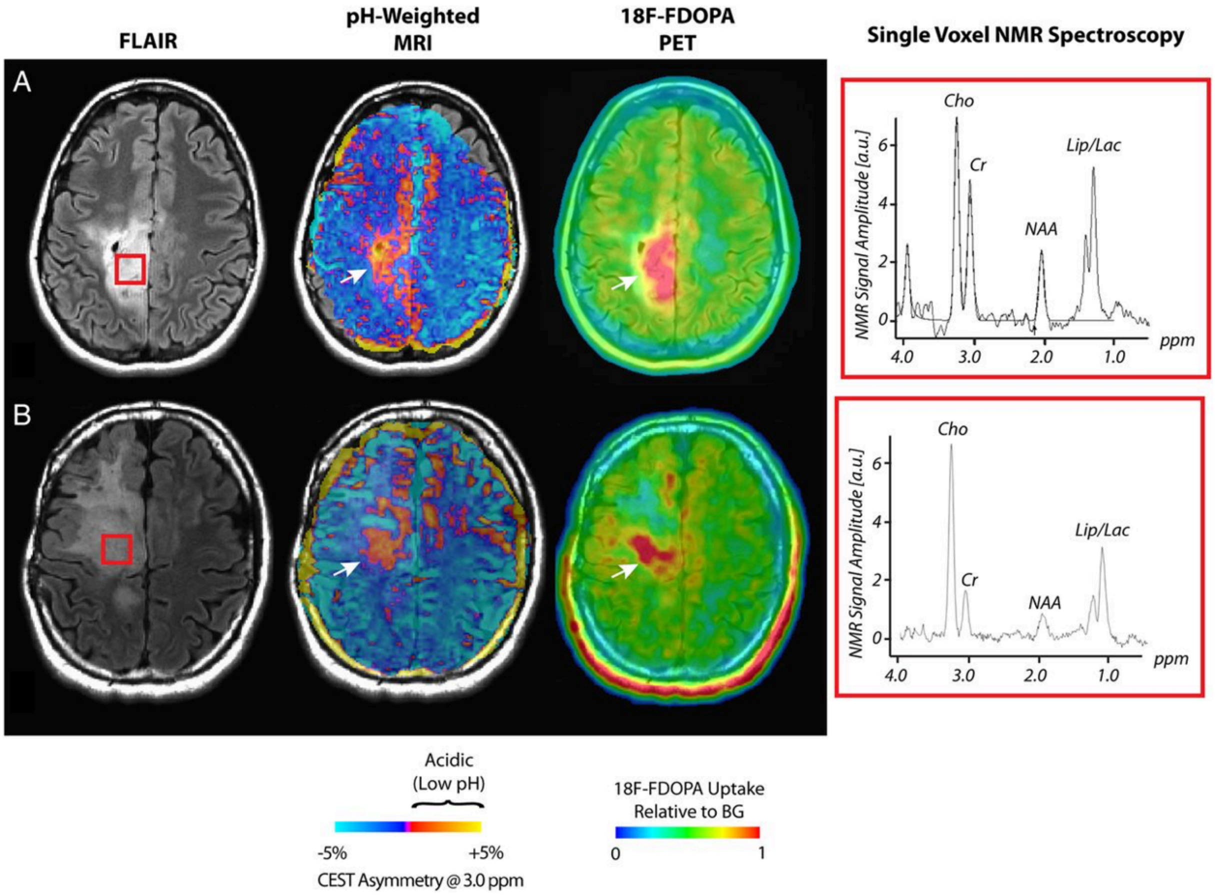

Figure 35. Spatial correspondence between pH-weighted molecular MRI, ^{18}F-FDOPA PET, and MR spectroscopy. (A and B) Two patients with anaplastic astrocytomas showing CEST asymmetry consistent with low pH in regions with confirmed elevated ^{18}F-FDOPA uptake and lactate. From left to right: T$_2$-weighted FLAIR, pH-weighted MRI using amine CEST, ^{18}F-FDOPA PET, and NMR spectrum from the area shown in the red box in FLAIR images. Cho = choline; Cr = creatine; NAA = N-acetyl aspartate; Lip/Lac = mobile lipids and/or lactate. (Both cases were confirmed to contain lactate based on inversion of the Lip/Lac peak by using an intermediate echo time = 135 ms). BG, basal ganglia. [15]

Stereotactic Image-Guided Biopsy Results

To confirm that regions suspected of containing acidic tissue on pH-weighted MRI contained viable tumor, we performed pH-weighted MR-guided biopsies in two patients. The first patient was a 26-year-old male with a large area of T2 hyperintensity, suggestive of tumor, but no contrast enhancement (Figures 36A&B).

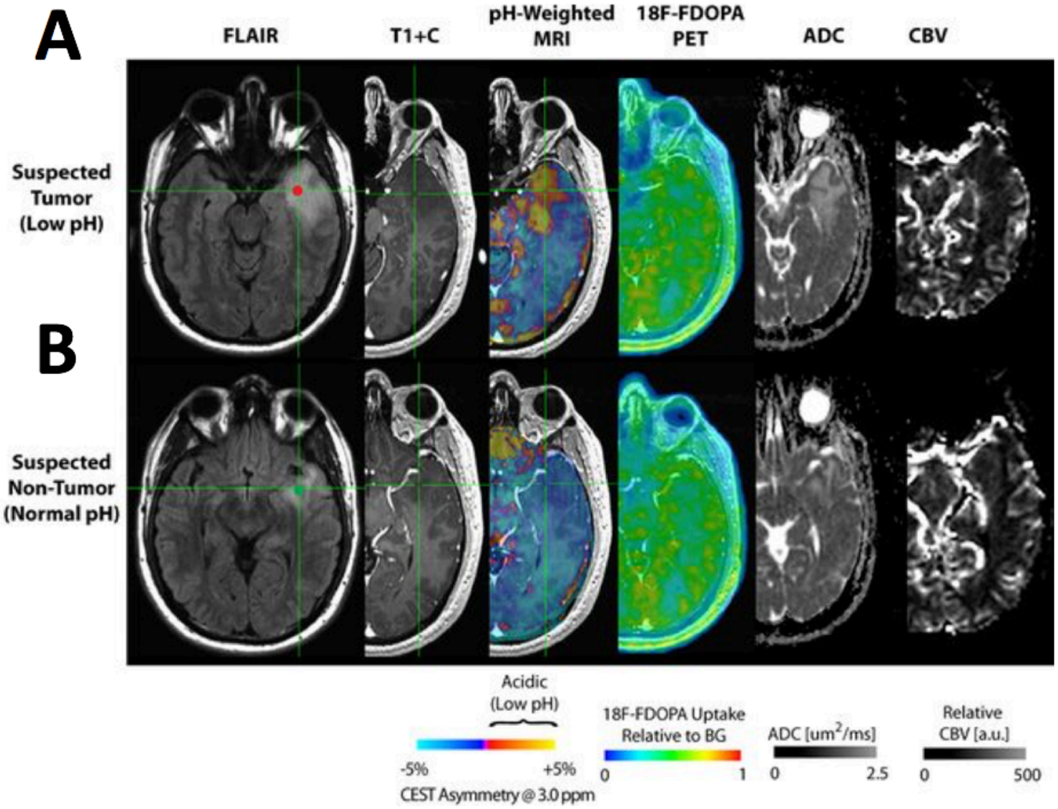

Figure 36. A 26-year-old male patient with a suspected low-grade glioma (WHO grade II). FLAIR images show T_2 hyperintense regions in the left temporal lobe, but no contrast enhancement on post-contrast T_1-weighted images (T1+C) or abnormal ^{18}F-FDOPA PET uptake was observed. Diffusion and perfusion MRI showed restricted diffusion on apparent diffusion coefficient (ADC) maps and no elevated CBV, respectively. pH-weighted MRI in inferior regions (A) showed elevated CEST asymmetry, consistent with regions of low pH. Superior regions (B), however, did not show elevated CEST asymmetry. [15]

^{18}F-FDOPA PET, perfusion MRI, and diffusion MRI were also negative. An acidic signature consistent with tumor on inferior aspects was shown on pH-weighted MRI (Figure 36A), whereas superior regions did not demonstrate this signature (Figure 36B). This suggested a unique contrast mechanism for pH-weighted images compared with anatomical contrast. Biopsy results confirmed that inferior regions contained low-grade glioma tissue with low proliferation rate (Ki-67, ~1%–2%) but high expression of hypoxia-inducible factor-1a, whereas superior regions did not show evidence of tumor (Figure 37).

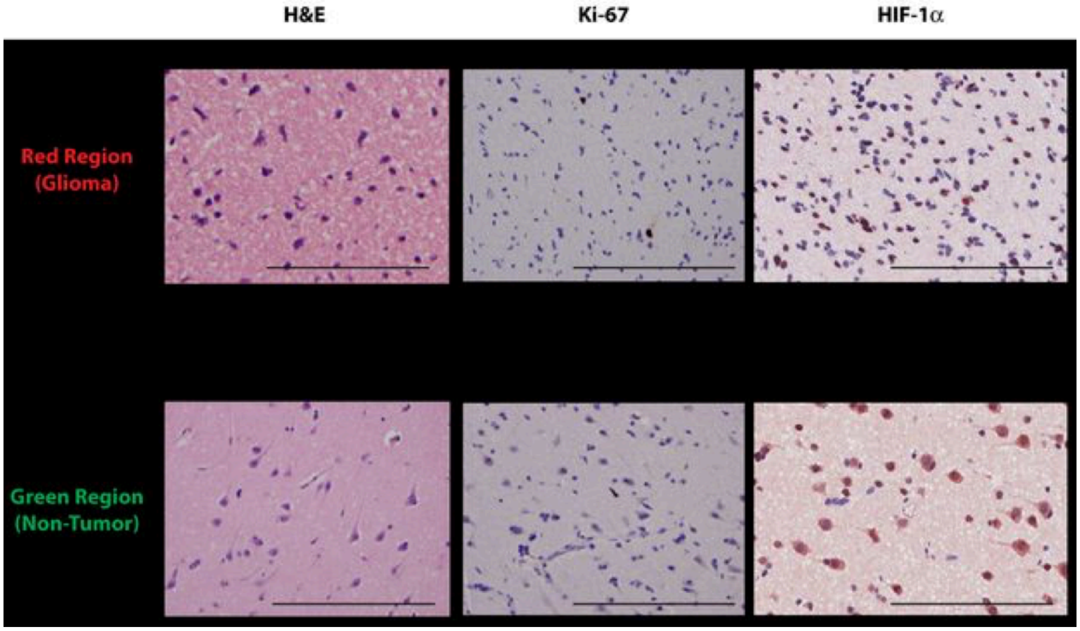

Figure 37. Histology for biopsy samples taken from the regions in red (Figure 36A) were confirmed to contain diffuse astrocytoma cells with low cellularity, low (but present) mitotic figures, and regions of hypoxia. Alternatively, samples obtained from the green region (Figure 36B) were consistent with hypoxic neurons likely hypertrophied from prolonger seizure activity and lacked mitotic figures or morphologic features of tumor. [15]

The second patient was a 47-year-old male with suspected recurrent glioblastoma. Upon scanning this patient, pH-weighted MRI suggested extensive acidic tumor regions and elevated ^{18}F-FDOPA uptake confined to areas of enhancement (Figure 38A).

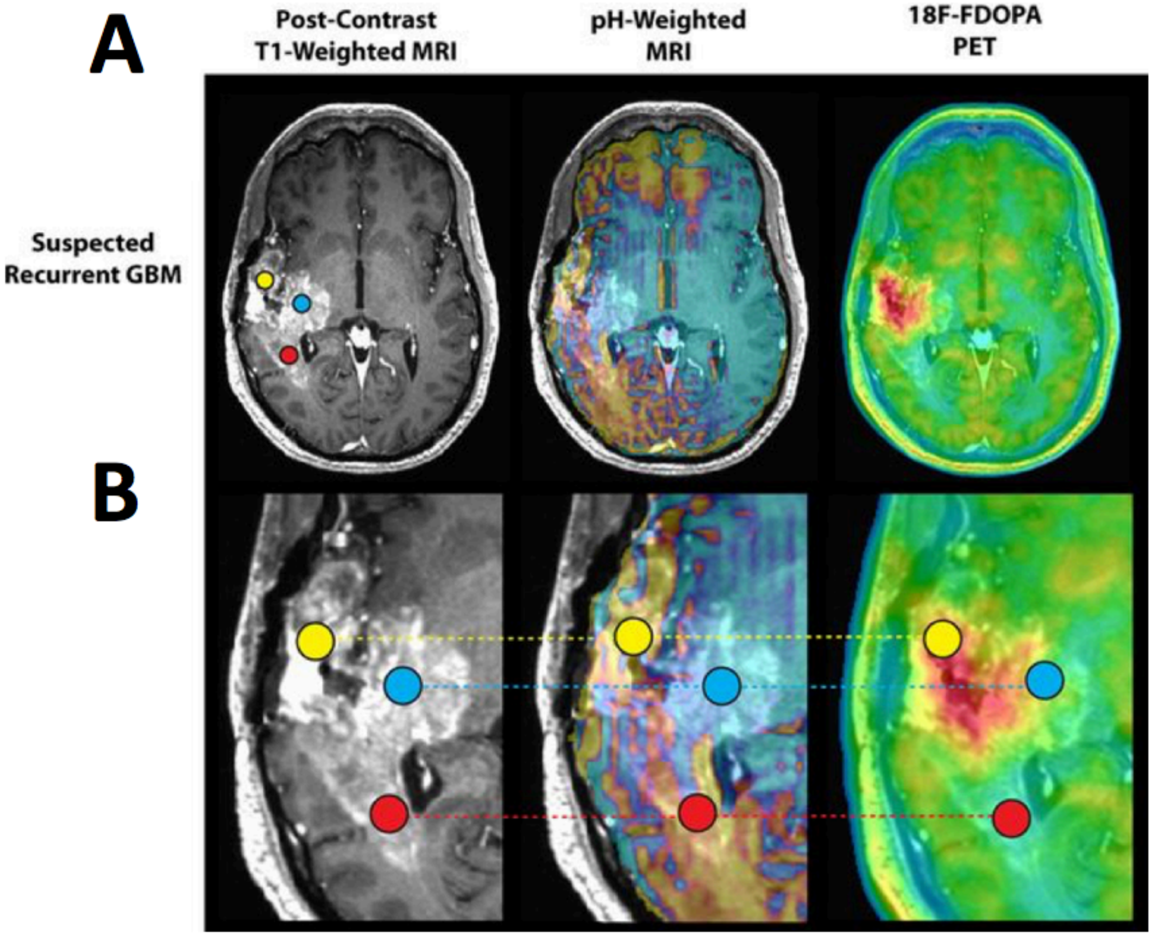

Figure 38. A 47-year-old male patient with recurrent glioblastoma (WHO grade IV). Post-contrast T1+C demonstrated a large extent of contrast-enhancing tissue suspect of recurrent tumor, but pH-weighted MRI and ^{18}F-FDOPA PET showed differing areas of abnormality. Three biopsy locations were obtained: yellow = areas of contrast enhancement, avid ^{18}F-FDOPA PET uptake, and low pH on CEST; blue = areas of contrast enhancement, moderate ^{18}F-FDOPA uptake, and normal pH on CEST; red = contrast enhancement, low pH on CEST and no ^{18}F-FDOPA uptake. [15]

Three biopsies were performed (Figure 38B), and areas that demonstrated acidic tumor signatures were histologically confirmed to contain recurrent tumor (yellow and red targets), whereas areas lacking CEST contrast at 3.0 ppm (blue target) were shown to contain extensive necrosis and macrophage infiltration consistent with treatment effects (Figure 39). Together, these results suggest pH-weighted MRI using amine CEST may provide high specificity for metabolically active tumor regions.

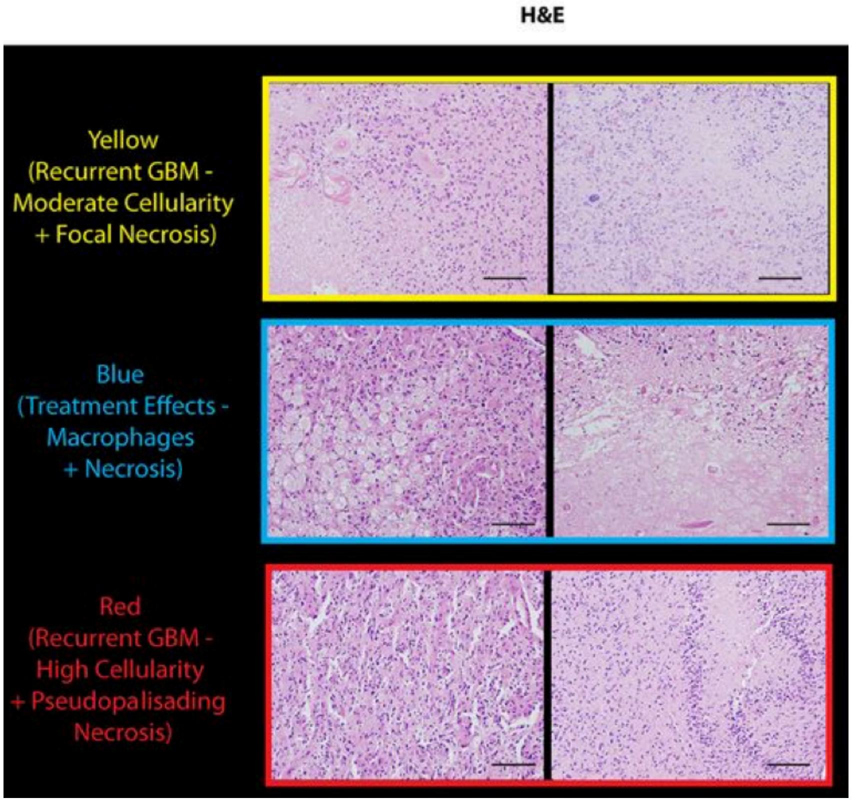

Figure 39. Histology from the biopsy targets shown in Figure 38 showed evidence of recurrent glioblastoma with moderate cellularity and focal necrosis in areas of yellow; evidence of treatment effects including macrophages and extensive necrosis in areas of blue; and high tumor cellularity with pseudopalisading necrosis consistent with recurrent glioblastoma in areas of red. [15]

vii. Discussion

This data supports the hypothesis that CEST imaging of the amine protons in solution can be used as a noninvasive pH-weighted MRI technique for investigation of malignant gliomas in human patients. CEST MRI provides molecular information about imaging targets that cannot be obtained with standard anatomical imaging techniques. We have quantified the effects of pH and concentration on the CEST signal obtained from the amine functional group, whose protons exchange at a much faster rate (thousands of Hz) than amide protons in the more commonly used APT technique (~30 Hz). CEST contrast as defined by MTR_{asym} at 3.0 ppm was shown to increase with both an increase in amino acid concentration and a decrease in pH within a physiologically relevant pH range for cancer tissues (~6.0 to 7.0 pH).

Although the majority of CEST phantom studies in recent years have targeted proteins or creatine, a select few amino acids have also been characterized. Cai et al. [125] characterized the CEST signature of glutamate phantoms and a rat stroke model at 7T, demonstrating that the CEST signal at 3.0 ppm increases with decreasing pH and increasing concentration, consistent with our findings. In separate studies, Cai et al [126], Kogan et al [75], Jin et al [80], and Jones et al [35] all observed a similar relationship between increasing CEST asymmetry at 3.0 ppm and decreasing pH at 7T. However, to our knowledge, our study is the first to demonstrate that the CEST signature of amino acid amine protons can be used as pH-weighted contrast at the more common clinical scanner strength of 3T. Additionally, the current study further documents the CEST signatures for additional amino acids, including glycine and phenylalanine, which have not been previously reported.

Previous studies have explored CEST imaging in human GBM for contrast mechanisms such as APT and nuclear Overhauser enhancement (NOE). For example, Togao et al [58] and

Zhou et al [127] showed that APT can stratify patients by tumor grade and differentiate between radiation necrosis and active tumor, respectively. Additionally, Paech et al [71], Zaiss et al [128], and Xu et al [129] cleverly exploited the NOE effect at high magnetic fields to show novel contrast within active tumor tissues. These studies, however, were performed at high magnetic field strengths (>7T) where NOE and other contrast mechanisms can influence the underlying CEST signal. Thus, the current study, performed at 3T, appears to provide unique molecular information beyond that of APT or NOE.

While APT imaging has become the most prevalent CEST technique implemented in the clinical setting, the slow exchange rate of the amide protons often necessitates a saturation pulse on the order of seconds to generate sufficient contrast [130]. Targeting the faster exchanging amine protons at 3.0 ppm allows for faster saturation of the target protons and shorter scan times per acquisition compared with APT. Further, APT has been shown to decrease with decreasing pH, making sensitivity to acidic tissue difficult to distinguish from other relaxation mechanisms [35, 131]. In comparison, amine CEST effects increase with increasing amino acid concentration and decreasing pH, both conditions that are found in active tumor tissue. However, it is important to note that the increasing effect of amine concentration on the CEST signal only occurs in the presence of a low pH, suggesting that amine CEST may act like a noninvasive "litmus test" for identifying acidic tissues.

Some studies have proposed Lorentzian fitting of the z-spectra rather than asymmetry analysis, with Lorentzian peaks centered on target frequencies of interest (i.e. bulk water at 0.0 ppm, amines at 3.0 ppm, amides at 3.5 ppm, NOE at -3.2 ppm, etc.) [44, 132, 133]. One advantage of this technique is that it does not require a control frequency to calculate the desired contrast. However, this technique does require acquisition of a full z-spectrum throughout the endogenous offset frequency range, rather than acquisition of a subset of data points around a particular target frequency. This may result in fewer data points around the target frequencies, leading to inaccuracy in the measurements of interest. Furthermore, unless every effect is accurately modeled, including pH effects that may change the properties of a peak through spectral blurring, unaccounted effects may lead to a poor fit to the data. For these reasons, conventional asymmetry analysis was used to obtain CEST contrast during our experiments.

There were a few limitations to these human studies that should be addressed. As the CEST acquisition contained between only 1-3 image slices, we were not able to collect pH-weighted coverage of the full tumor. Since the acquisition of this data, technical improvements to our sequence have allowed full brain coverage by leveraging new acceleration techniques. Additionally, the CEST data may be affected by the T_2 properties of the tissue in addition to exchange properties, although our identification of hyperintense pH-weighted regions not corresponding to T_1 or T_2 lesions indicates that mechanisms besides relaxation rates are likely responsible for the observed contrast. Finally, although we had 20 patients with serial pH-weighted imaging, we had only two patients in which biopsy data were available; a larger cohort of biopsy cases is needed to correlate histology with pH-weighted imaging.

Chapter V

CEST-EPI in Human Subjects

While the data collected using our CEST-GRE sequence provided evidence that pH-weighted imaging can be used as a biomarker in human gliomas, it is limited by relatively slow acquisition times and limited coverage compared to other readout techniques. In this chapter, we describe development of an improved pH-weighted MRI sequence and its further application in human gliomas.

i. Echo-Planar Imaging

Although the CEST-GRE sequence was useful for initial phantom experiments and collecting patient data, we are limited by long acquisition times and therefore limits on the brain coverage it can achieve within clinical scan times. Because of this, we designed a CEST sequence that utilizes an echo-planar imaging (EPI) readout [134]. When using an EPI readout, a standard excitation pulse is applied, followed by a readout of the entirety of k-space before the next excitation by rapid switching of the gradients. This allows for a great acceleration in imaging time compared to a GRE sequence, where only one line of k-space is read out per excitation pulse.

Although the EPI sequence has distinct advantages in terms of imaging time, they come with tradeoffs as is typical in MR imaging. EPI sequences are particularly susceptible to fat chemical shift artifacts [135]. These arise because protons on fat molecules have resonance frequencies shifted away from the bulk water resonance; because MRI uses frequency encoding for spatial mapping as described in Chapter I, these differences in frequency can result in a shift in the position of the fat during image reconstruction. Although chemical shift artifacts from fat are not often an issue within the brain tissue itself, fat tissue lining the skull of the brain can form a shifted oval artifact through the brain when using EPI, as seen in Figure 40A. This problem can be mediated by using a direct water excitation pulse for fat suppression, which excites a narrower bandwidth of frequencies around water than a traditional excitation pulse and removes this artifact (Figure 40B).

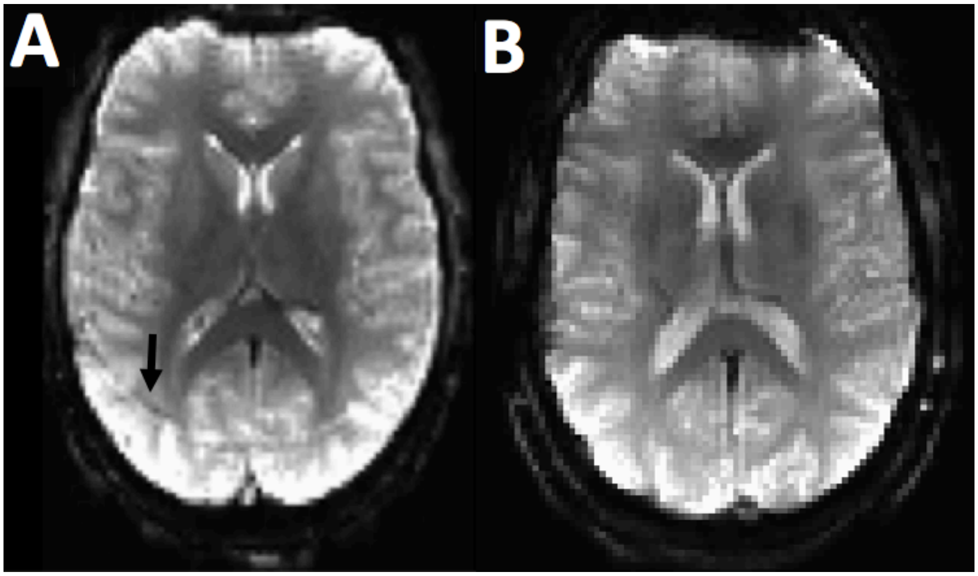

Figure 40. A) EPI with a standard excitation pulse produces a fat chemical shift artifact through the brain (black arrow). B) EPI with a direct water saturation excitation pulse produces an image without this chemical shift artifact.

A direct water excitation pulse has been implemented in our CEST-EPI sequence, as shown in Figure 41.

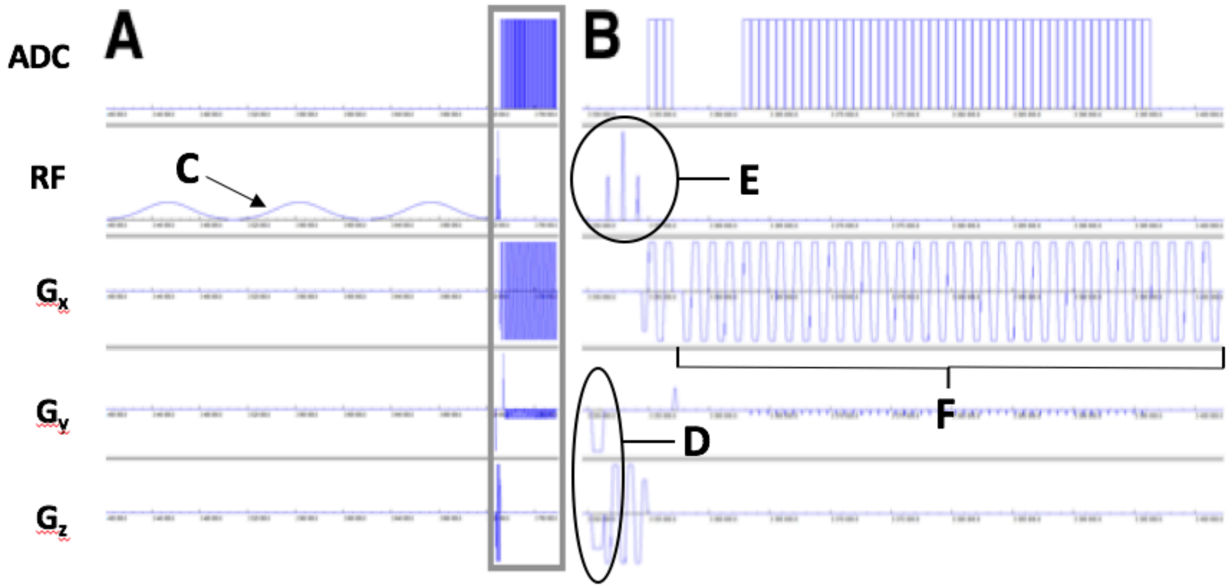

Figure 41. The CEST-EPI pulse sequence diagram, as simulated in POET on the VD-13D IDEAS platform (Siemens AG, Munich, Germany). The five rows shown in the pulse diagram represent the analog-to-digital converter (ADC), the RF amplitude (RF), and the gradient magnitude in the x-, y-, and z-directions (G_x, G_y, G_z). A) A single repetition of the saturation pulse and readout. B) A magnification of the readout portion, which is enclosed by the gray box in (A). C) The off-resonance RF saturation pulse train. D) Spoiling gradients to remove residual transverse magnetization before readout. E) A 1:2:1 spectral-spatial 90° water excitation pulse used to minimize artifacts from fat chemical shift. F) Readout of every line of k-space in the imaging plane.

EPI with gradient echo readout is typically also associated with signal loss in the frontal lobe of the brain, due to susceptibility differences between the brain tissue and the nasal cavity [136] (Figure 42).

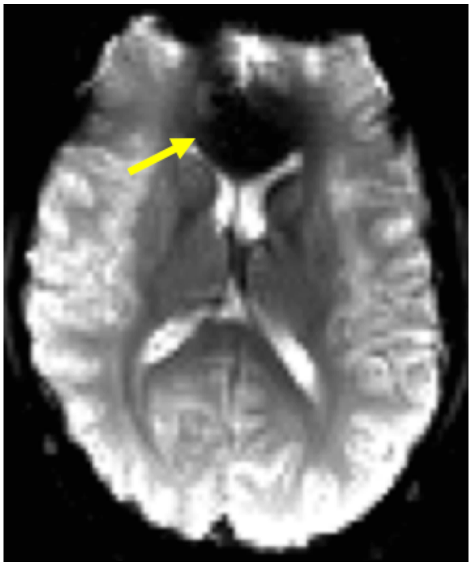

Figure 42. High susceptibility in the inferior frontal region of the brain (yellow arrow) often causes signal loss when using EPI.

ii. Clinical CEST-EPI Sequence Optimization

Effects of Advanced Shimming on Image Quality

Although B_0 inhomogeneity can be corrected for during post-processing of CEST data, it is desirable to reduce inhomogeneity in the acquired data as much as possible. Our Siemens 3T MR systems are capable of performing an advanced B_0 shim prior to data acquisition to improve fidelity to the bulk water resonance throughout the scan. However, this comes at a cost of increased scan time, as this advanced shim takes approximately 90-120 seconds to complete. To determine whether this advanced shimming had a significant effect on centering of the bulk water peak at 0 ppm, we acquired CEST z-spectra in a pure water phantom before and after the application of an advanced shim, with the standard shim used as a baseline. Z-spectral points between -2.0 and 2.0 ppm in units of 0.1 ppm were acquired using a CEST-EPI acquisition with a saturation pulse train of 3x100 ms 6 μT Gaussian pulses. An S_0 scan was acquired with $B_1 = 0$

μT to normalize the z-spectra. For each image voxel, the minimum value in the z-spectra was taken as the observed bulk water peak and the distance between this spectral point and 0 ppm was taken as the B_0 inhomogeneity for that voxel. Within an ROI covering five slices of the water phantom, the inhomogeneity at each voxel was extracted and plotted in a histogram for both the standard and advanced shim scans. A smaller circular ROI was drawn in one corner of the center slice and the mean z-spectra within this circular ROI were extracted for both the standard and advanced shim scans. Results are shown in Figure 43.

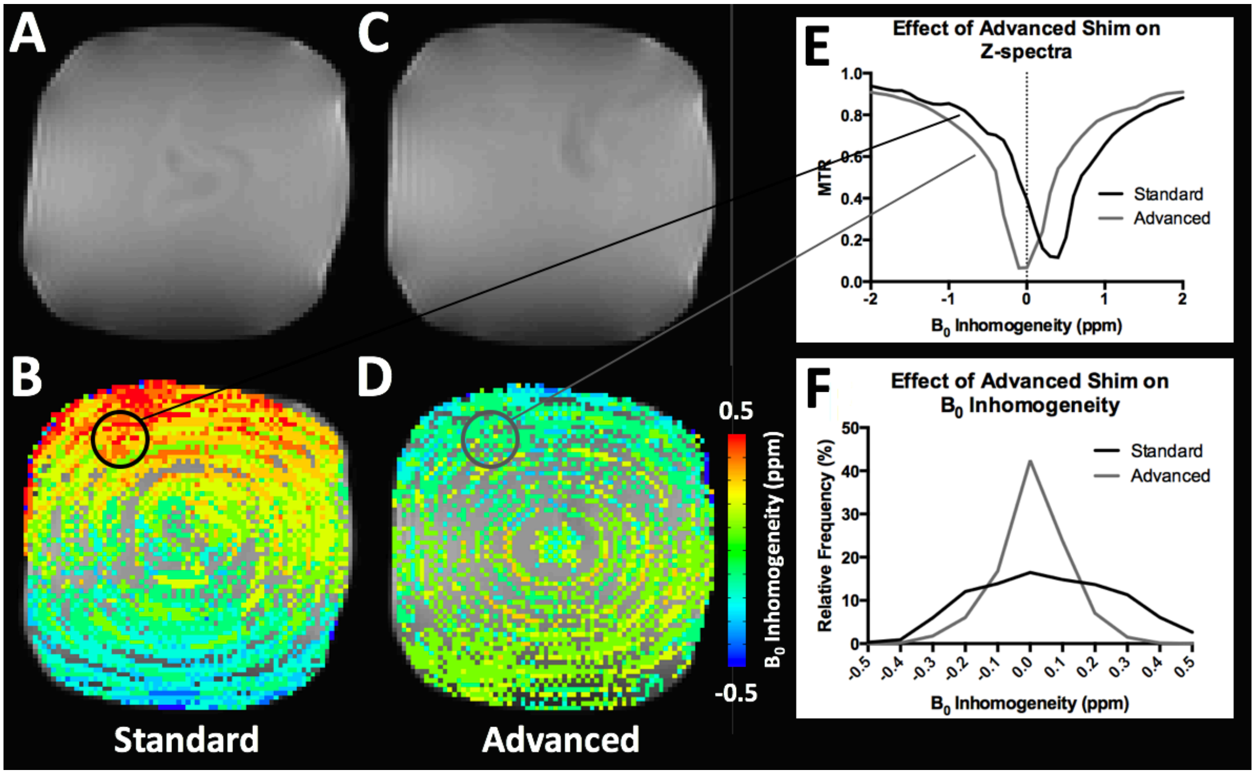

Figure 43. Effects of advanced B_0 shimming on a water phantom. A) Phantom after standard shim. B) Map of B_0 inhomogeneity after standard shim as measured by acquisition of CEST z-spectra. Voxels with no overlaid color have an inhomogeneity of 0 ppm. C) Phantom after advanced shim. D) Map of B_0 inhomogeneity after advanced shim as measured by acquisition of CEST z-spectra. Voxels with no overlaid color have an inhomogeneity of 0 ppm. E) Mean z-spectra within a circular ROI on one slice for both standard and advanced shims. F) Histogram of B_0 inhomogeneity values within a large multi-slice ROI for both standard and advanced shims.

The advanced shim resulted in a qualitative decrease in inhomogeneity throughout the imaging target compared with the standard shim (Figures 43B&D). The advanced shimming causes the measured center of the z-spectra to shift closer to the true bulk water frequency of 0 ppm for many voxels, particularly on the periphery of the imaging target (Figures 43E). Histograms quantitatively showed that advanced shimming results in a larger number of voxels having low inhomogeneity than a standard shim, with almost half of voxels having an inhomogeneity of ~0.0 ppm (Figure 43F). Advanced shimming also resulted in a reduction in image distortion compared with the standard shim (Figures 43A&C). This is likely due to the intrinsic sensitivity of the EPI k-space readout to small B_0 inhomogeneities, which can cause distortion in the resulting image [137]. Because of the advantages in terms of z-spectral centering and distortion reduction conferred when using an advanced shim, we determined that the cost of additional scan time was justified and implemented this advanced shim for all clinical CEST-EPI acquisitions moving forward.

B_0 Inhomogeneity in Human Subjects

Correction for B_0 inhomogeneity requires acquisition of z-spectral points around the bulk water frequency of 0 ppm to determine which offset frequency provides minimum signal; the difference between that minimum frequency and 0 ppm is taken as the inhomogeneity in that voxel. However, when acquiring a subset of spectral points rather than a full z-spectrum as is often necessary during clinical imaging, it is unclear how far away from the bulk water peak that spectral points must be acquired to ensure measurement of the minimum in each voxel for proper inhomogeneity correction. To determine the number of spectral points around the bulk water peak that must be acquired in a human subject, we collected CEST data in a healthy human volunteer using a CEST-EPI acquisition with offset frequencies between -1.0 and 1.0 ppm in units of 0.1 ppm and a saturation pulse train of 3x100 ms 6 μT Gaussian pulses. An S_0 scan was acquired with $B_1 = 0$ μT to normalize the z-spectra. An advanced shim was applied prior to image acquisition to reduce B_0 inhomogeneity throughout the brain. For each image voxel, the minimum value in the z-spectra was taken as the observed bulk water peak and the distance between this spectral point and 0 ppm was taken as the B_0 inhomogeneity for that voxel. Results are shown in Figure 44.

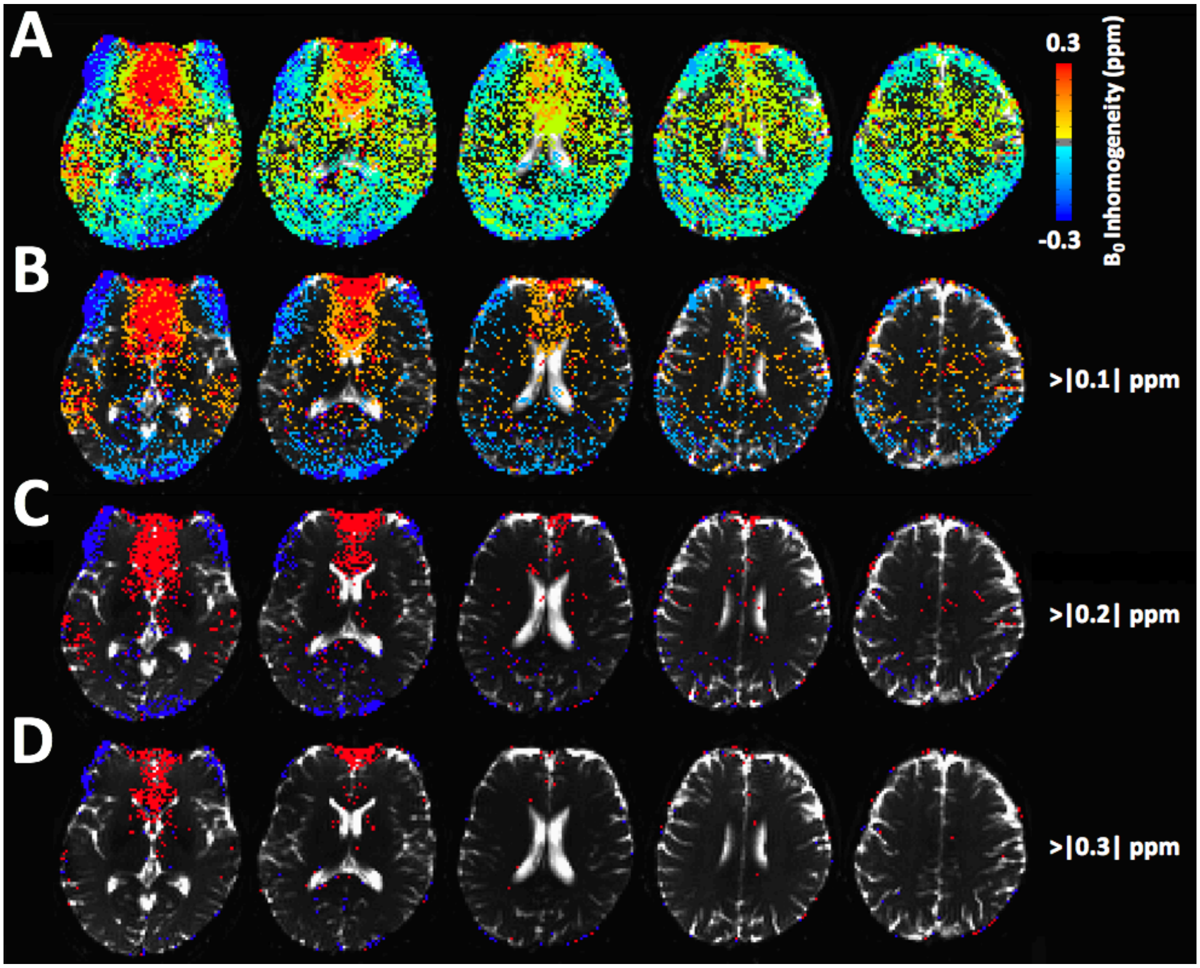

Figure 44. Measurement of B_0 inhomogeneity in a healthy human volunteer. Images A-D are thresholded to visualize the z-spectral distance from 0 ppm that must be acquired to measure the minimum in a particular voxel. Voxels not remaining in the mask are within the stated inhomogeneity threshold; voxels present in the mask are outside of this threshold. A) Voxels with inhomogeneity of >0.0 ppm are visualized. B) Voxels with inhomogeneity of >|0.1| ppm are visualized. C) Voxels with inhomogeneity of >|0.2| ppm are visualized. D) Voxels with inhomogeneity of >|0.3| ppm are visualized.

While the majority of brain voxels had B_0 inhomogeneity of |0.1| ppm or greater (Figure 44A), almost all brain voxels fell within an inhomogeneity range of ±0.3 ppm (Figure 44D). Because of this, we obtained ±0.3 ppm as an appropriate range to acquire data during clinical CEST-EPI acquisitions. The exception to this window is a region of high inhomogeneity superior to the nasal cavity, a feature commonly seen in previous studies [138]. This region is additionally associated with signal dropout on EPI and acquiring further z-spectral points would likely not improve image quality in this region.

Effects of Bandwidth on Image Quality

Although EPI allows for accelerated imaging, it comes with a tradeoff of spatial distortion caused by imperfections in the rapid readout of k-space. These distortions typically increase with increasing TE and decrease with increasing bandwidth [139]. Minimization of TE is also desired to minimize any effects of T_2 weighting in the resulting images. To determine an optimal TE and bandwidth for our EPI sequence, we applied this sequence to a water phantom using TR = 800 ms, matrix size = 128x128, FOV = 256x256 mm, slice thickness = 4 mm with no gap, number of slices = 25, phase encode direction = A>>P. Samples of glutamine and water were placed within the water phantom to visualize the finer effects of spatial distortion. Bandwidth was varied between 798, 1184, and 1628 Hz/pixel and using the minimum TE at each bandwidth (92, 67, and 49 ms, respectively). Bandwidth could not be raised above 1628 Hz/pixel without the sequence failing to run on a clinical scanner. A saturation pulse train (6 µT, +3.0 ppm) was applied prior to readout. Results can be seen in Figure 45.

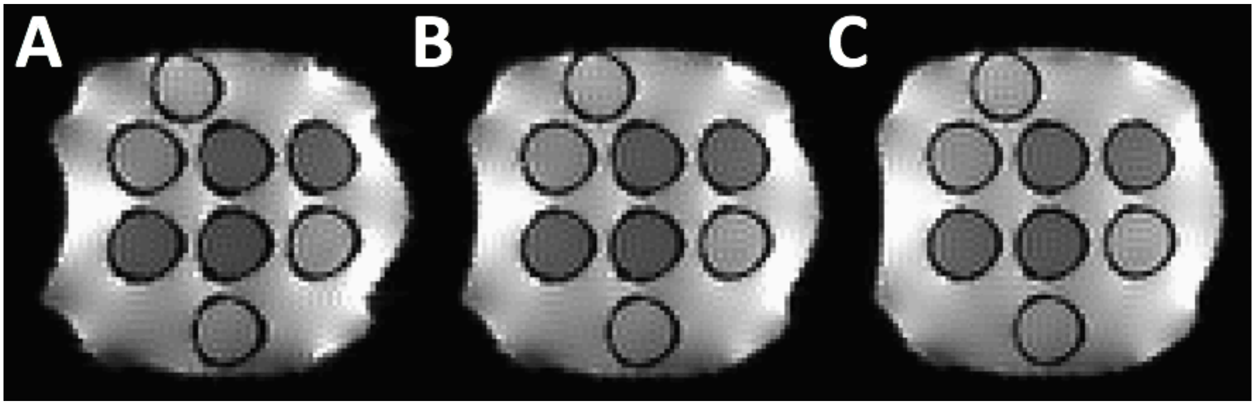

Figure 45. Effects of increasing bandwidth and decreasing minimum TE on a phantom of water and glutamine. A) 798 Hz/pixel, TE=92 ms; B) 1184 Hz/pixel, TE=67 ms; C) 1628 Hz/pixel, TE=49 ms. A reduction in EPI distortion is seen at higher bandwidth and lower TE.

As expected, an increase in bandwidth and subsequent decrease in minimum TE resulted in a decrease in distortion in the frequency encode direction (R>>L). Therefore we used the maximum allowable bandwidth (1628 Hz/pixel) in all future EPI applications.

We also tested the influence of a common acceleration technique termed generalized autocalibrating partially parallel acquisition (GRAPPA) on our EPI sequence [140]. GRAPPA allows for image acquisition using undersampled k-space, which allows for use of a shorter TE by reducing the length of the echo train, further reducing distortion artifacts as well. However, high GRAPPA acceleration comes at a cost of a reduced signal to noise ratio (SNR). A GRAPPA factor of 2 was chosen for our CEST-EPI sequence. An example of the benefits of GRAPPA is shown in Figure 46.

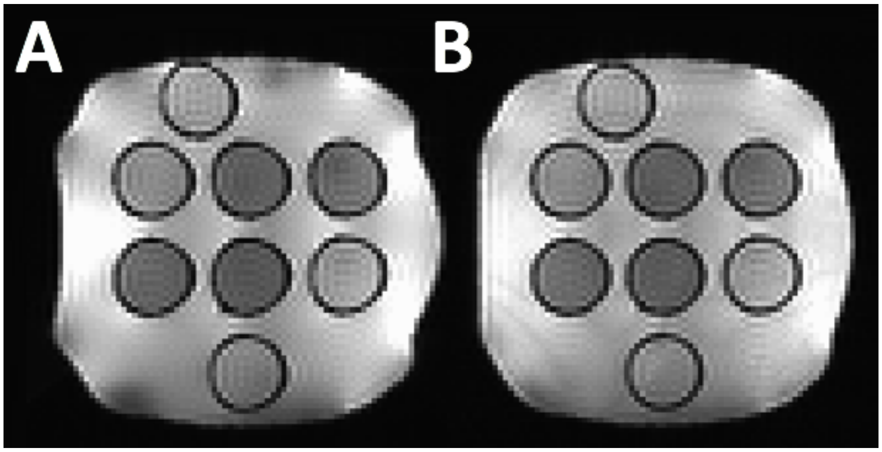

Figure 46. A) A phantom of water and glutamine imaged with CEST-EPI with no GRAPPA acceleration (bandwidth = 1628 Hz/pixel, TE=49 ms. B) The same phantom imaged with a GRAPPA factor of 2 and subsequent reduced TE (bandwidth = 1628 Hz/pixel, TE=27 ms). Activation of GRAPPA and subsequent reduction in TE further reduces image distortion.

Effect of Saturation Pulse Amplitude on Traditional MT

Previous studies have reported an increase in the CEST asymmetry in normal brain tissue with increasing saturation pulse amplitude B_1 [141]. To test whether this trend was true for our clinical CEST-EPI sequence, a healthy volunteer underwent pH-weighted imaging while varying the saturation pulse amplitude between 1 and 6 μT. A single S_0 scan with $B_1 = 0$ μT was used to normalize all data. An ROI was drawn in a region of NAWM as defined on the S_0 image and the mean and standard deviation of MTR_{asym} within the NAWM region were calculated. Results are shown in Figure 47.

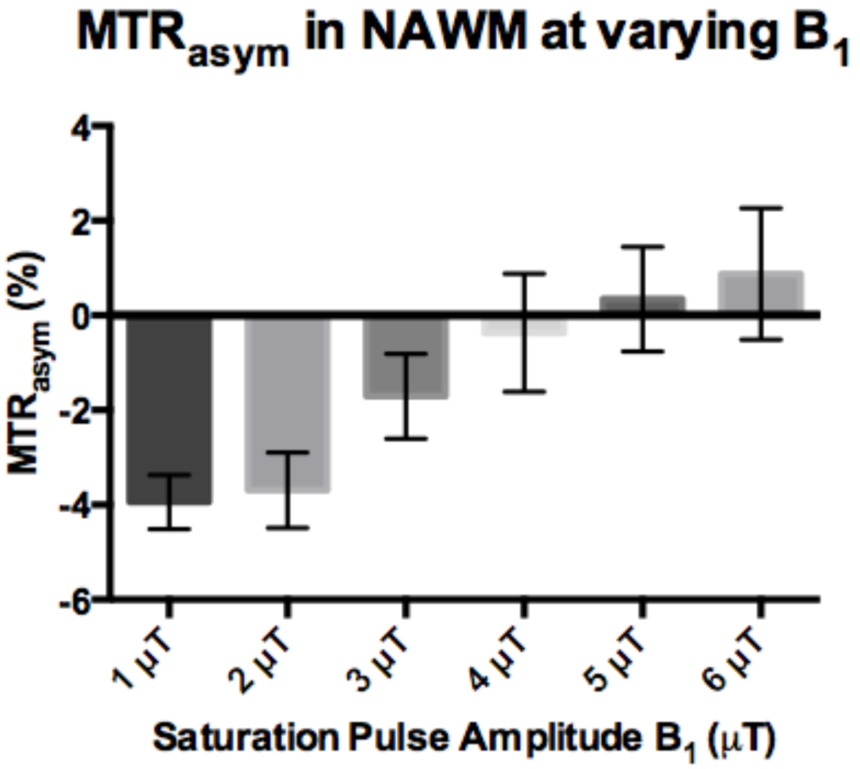

Figure 47. MTR_{asym} in NAWM of a healthy volunteer at varying saturation pulse amplitude. MTR_{asym} increases with increasing B_1, likely due to traditional magnetization transfer effects. Error bars denote standard deviation of MTR_{asym} values with the ROI.

As expected, results showed an increase in asymmetry within healthy tissue with increasing B_1 (Figure 47). A small positive baseline asymmetry can therefore be expected from our clinical CEST-EPI sequence when using saturation pulse amplitudes of 6 µT.

iii. Clinical CEST-EPI Sequence Parameters

Parameters for the final CEST-EPI sequence used in patient data collection moving forward were as follows: TE/TR = 27/375 ms, matrix size = 128x128, FOV = 256x256 mm, GRAPPA = 2, bandwidth = 1628 Hz/pixel, slice thickness = 4 mm with no gap, number of slices

= 25, phase encode direction = A>>P. A saturation pulse train of 3x100 ms 6 μT Gaussian pulses separated by a deadtime of 10 ms was applied prior to water-selective excitation and readout. The total time for the readout per repetition for our CEST-EPI sequence was approximately 60 ms for a TE of 27 ms. This sequence once again uses spoiler gradients prior to the excitation pulse to destroy any residual transverse magnetization. The saturation offset frequencies were swept from -3.5 to -2.5 ppm, from -0.3 to 0.3 ppm, and from 2.5 to 3.5 ppm in units of 0.1 ppm for a total of 29 spectral measurements. The acquisition time for this scan was 5:00, and this scan was run twice on each patient. An S_0 image was also acquired by keeping all parameters the same and reducing the B_1 amplitude to zero (number of averages = 4), with an acquisition time of 1:04. Therefore, the total acquisition time for pH-weighted imaging was 11:04. The 100 mm of total slice coverage was enough for whole brain coverage in all glioma patients imaged thus far.

Following data acquisition, all data was motion corrected using the *mcflirt* function in FMRIB Software Library (Functional Magnetic Resonance Imaging of the Brain; http://www.fmrip.ox.ac.uk/fsl/). Voxel-wise inhomogeneity correction was performed by taking the point of lowest signal intensity between -0.3 and 0.3 ppm and setting to 0 ppm for each voxel, and shifting the z-spectrum accordingly. The reference (-ω) frequency image was then obtained by taking the integral of the B_0-corrected -3.2, -3.1, -3.0, -2.9, and -2.8 ppm images, and the target frequency image was obtained by taking the integral of the B_0-corrected 2.8, 2.9, 3.0, 3.1, and 3.2 ppm images. The difference between these images were then divided by the S_0 image to obtain maps of MTR_{asym}, as given by Eqn. 13.

iv. Healthy Subjects

The clinical CEST-EPI sequence was first applied in healthy controls to determine feasibility. Five healthy subjects received the clinical CEST-EPI protocol, which was applied twice. Maps of $\mathrm{MTR}_{\mathrm{asym}}$ were calculated separately for each run of the sequence, and were then averaged together. CEST data was registered to a 1.0 mm isotropic T1-weighted brain atlas (Montreal Neurological Institute 152). An ROI was drawn within a region of NAWM for each patient and the mean $\mathrm{MTR}_{\mathrm{asym}}$ was extracted from this region. Results are shown in Figure 48.

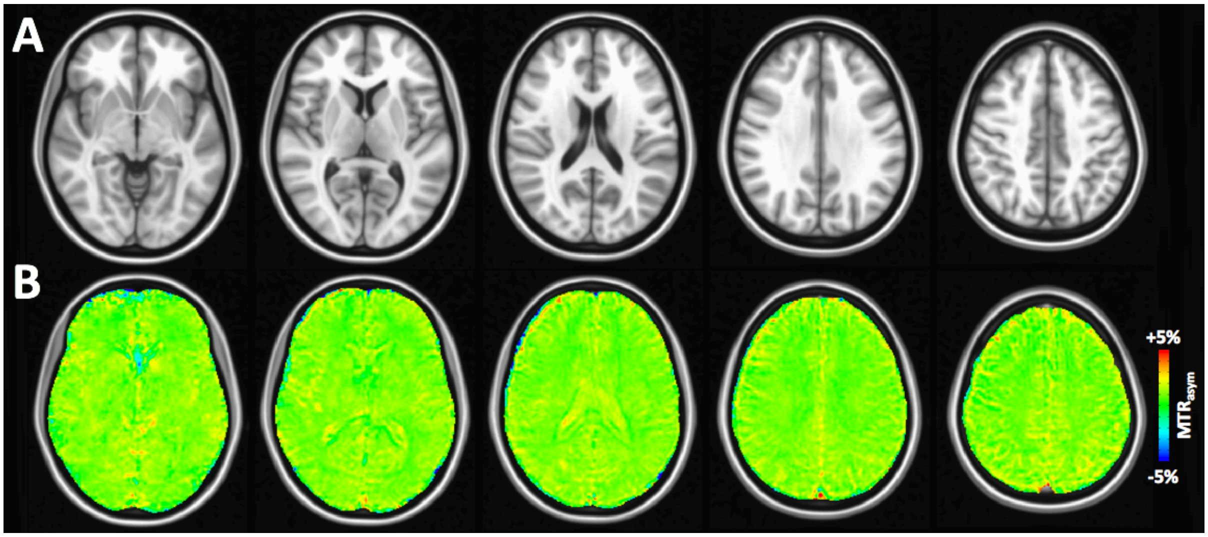

Figure 48. pH-weighted data acquired in healthy human subjects using our clinical CEST-EPI sequence. A) A T_1-weighted healthy brain atlas. B) Maps of $\mathrm{MTR}_{\mathrm{asym}}$ are fairly homogeneous throughout the brain tissue.

The values of $\mathrm{MTR}_{\mathrm{asym}}$ within NAWM showed a small positive asymmetry, with a mean of 0.82±0.05%. This standard deviation is relatively small, and reflects the homogeneity seen throughout maps of $\mathrm{MTR}_{\mathrm{asym}}$ in healthy subjects.

v. CEST-EPI for Biopsy Targeting

As described in Chapter IV, histology from biopsy samples targeted using our CEST-GRE sequence showed that regions of high pH-weighted CEST contrast contained tumor and regions of low CEST contrast did not. While these results were promising, biopsy samples were only obtained in two patients, and the CEST-GRE sequence was limited to only identifying biopsy targets within a narrow range of tumor coverage. Because of this, histology from CEST-targeted biopsies involving a larger patient cohort and a full-coverage scan was necessary to explore this technique further. Therefore, we implemented pH-weighted CEST-EPI in the clinical scan protocol that patients receive for pre-operative planning prior to undergoing surgery.

Eighteen patients with suspected gliomas were enrolled in this study. All patients gave informed consent and this trial was compliant with the Health Insurance Portability and Accountability Act and approved by the institutional review board at our institution. All patients received anatomical MRI on a 3T MR system (Siemens 3T Prisma) that included pre- and post-contrast (Gd-DTPA at a dose of 0.1 mmol/kg body weight; Magnevist) axial T1-weighted "Magnetization-Prepared Rapid Gradient Echo" (MPRAGE), axial T_2-weighted, axial FLAIR, and volumetric T_2-weighted "Sampling Perfection with Application optimized Contrasts using different flip angle Evolution" (SPACE) sequences. In addition to anatomical MRI, patients received 64-direction DTI and DSC-MRI as described in Chapter IV. A subset of patients also received a dual-echo T_2-weighted sequence that was used for quantitative T_2 mapping (TE=9/108 ms, TR=6000 ms). Maps of CBV and CBF were calculated using established perfusion algorithms [142, 143]. ADC maps were calculated from DTI data as well.

Patients also received the pH-weighted CEST-EPI scan as described previously. Patients then underwent surgery or surgical biopsy as clinically indicated between 1 and 21 days after imaging (mean = 7.8±6.1 days). Prior to surgery, CEST-EPI data was post-processed and registered to the post-contrast MPRAGE image. All other anatomical scans were registered to the post-contrast MPRAGE image as well. T_1 subtraction maps were calculated from the pre- and post-contrast MPRAGE images to improve delineation of gadolinium enhancement [144]. Within regions of FLAIR and gadolinium enhancement on the anatomical images, targets for biopsy were manually defined; one or two targets were typically chosen in regions of high MTR_{asym}, and another one or two targets were chosen in regions of low MTR_{asym}. Regions of intermediate MTR_{asym} were generally avoided to maximize the differences in tissue characteristics. Targets consisted of a sphere 5 mm in diameter, and spheres were placed as to not have any overlap within the lesion. We attempted to place a maximum of four ROIs for each patient; however, the size of the lesion often allowed for only two or three ROIs, and one low-grade patient only had space for a single ROI. During pre-operative planning, the neurosurgeon ensured that ROIs were not placed in any eloquent areas or within tissue that was not being resected. Following placement of the ROIs, the target images were uploaded to the surgery suite and used intraoperatively to select tissue samples for biopsy.

Histologic Markers

Standard H&E staining, KI-67 staining, and HIF-1α staining was performed as described previously on biopsy samples taken from the surgical patient cohort. In addition, stains were performed to quantify the presence of VEGF, cluster of differentiation 31 (CD31), and cluster of differentiation 133 (CD133). VEGF is often used as a marker of angiogenesis, which typically accompanies high levels of hypoxia and acidosis [145]. CD31 is a protein that is expressed in certain tumors and is typically used to show the presence of endothelial cells, which can correlate to the degree of tumor angiogenesis [146]. CD133 is a protein that acts as a stem cell marker in tumor tissue [147]. All of these markers were able to provide qualitative information through visualization of the stain results, as well as quantitative information through the use of cell counting algorithms.

For each biopsy sample, the number of positive nuclei pixels within both the whole section area and tumor area was calculated. The whole section area was determined by the amount of tissue on the slide, and the tumor area was the subset of this tissue determined to be tumor by a histopathologist (Figure 49). The number of positive nuclei divided by both the whole section area and tumor area was also calculated for each sample.

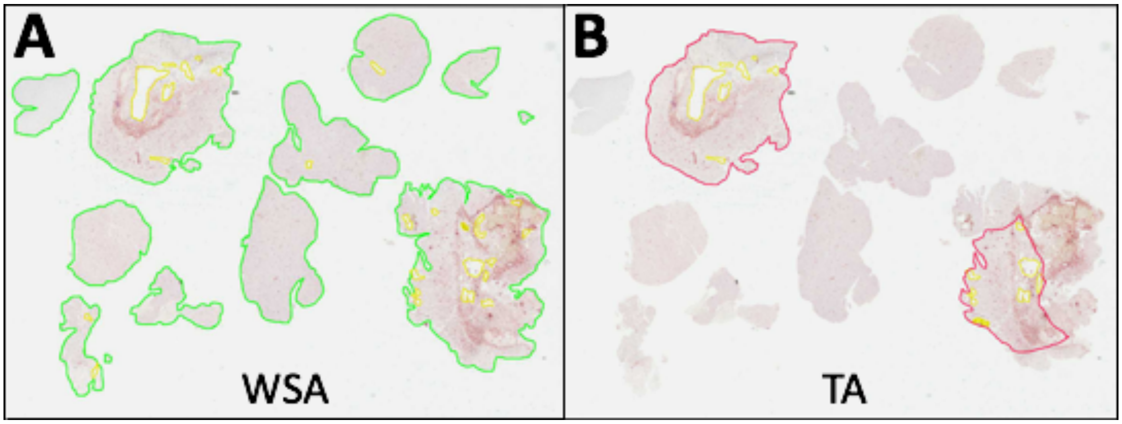

Figure 49. A tissue slide from a glioma patient biopsy used for histochemical analysis. A) The whole section area (WSA), delineated in green, consists of all tissue on the slide. B) The tumor area (TA), delineated in red, is a subset of the WSA that is identified as tumor.

To test whether the histology data were normally distributed, we first applied a Shapiro-Wilk normality test to all histologic marker measurements. We found that none of the markers had a normal distribution of NSPP in either the whole section area or the tumor area ($P<0.05$ for all measurements). We then paired low $\mathrm{MTR}_{\mathrm{asym}}$ and high $\mathrm{MTR}_{\mathrm{asym}}$ biopsy samples within the same patient and the same type of enhancing region (i.e. either FLAIR or T1+C); twelve of these pairs were available for comparison. We applied a Wilcoxon matched-pairs signed rank test to determine whether the number of strong positive pixels (NSPP) was greater in areas of high $\mathrm{MTR}_{\mathrm{asym}}$ than in areas of low $\mathrm{MTR}_{\mathrm{asym}}$ for CD31, CD133, Ki67, HIF-1α, and VEGF stains. We also tested whether the tumor area itself was larger in areas of high $\mathrm{MTR}_{\mathrm{asym}}$.

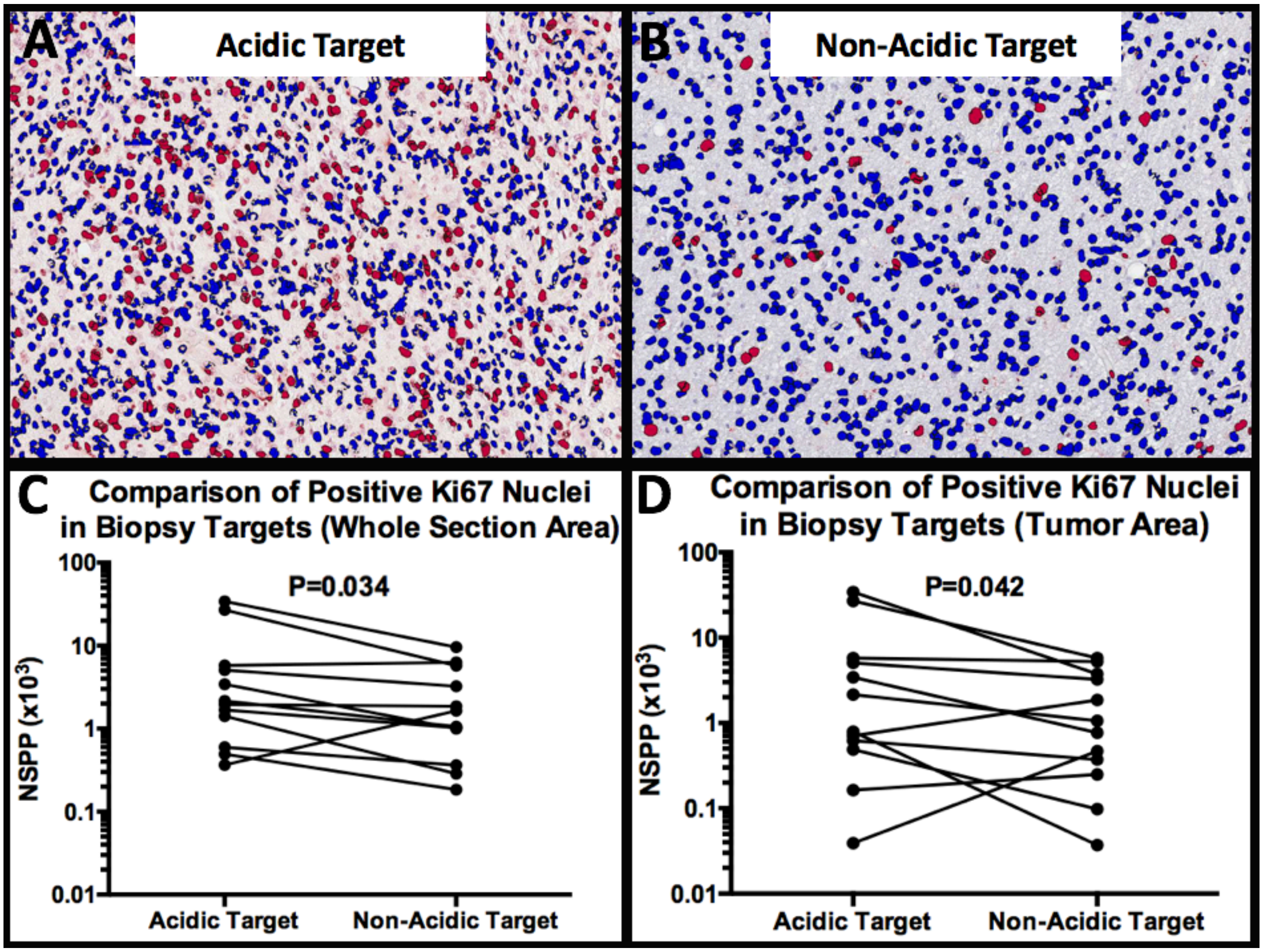

Figure 50. A) Ki67 stain for a biopsy target within an acidic region of a GBM. B) Ki67 for a biopsy target within a non-acidic region of the same GBM. Across the patient cohort, acidic biopsy targets had a significantly greater number of positive Ki67 nuclei in acidic targets compared with non-acidic targets for both the C) whole section area (WSA) and D) tumor area (TA). NSPP = number of strong positive pixels.

Results from Ki67 staining showed a significantly higher number of proliferating nuclei in acidic regions compared with non-acidic regions for both the whole section area (Figure 50C, *P=0.034*) and the tumor area (Figure 50D, *P=0.042*). This is an intuitive result as areas of higher tumor proliferation are expected to be more acidic. Results from HIF-1α staining did not show a significant difference between the number of positive nuclei between acidic and non-acidic targets, but interestingly did show that acidic biopsy targets had a significantly larger amount of tumor in the sample (Figure 51, *P=0.0186*). Similarly, the difference between tumor area in acidic and non-acidic biopsy targets was trending towards significance for the Ki67 stains as well (*P=0.0522*). While not a result of the markers themselves, these results may be due to the association between increased acidity and tumor growth at these biopsy sites. Stains for CD31 and CD133 did not reveal any significant correlations, and VEGF staining did not reveal up-regulation in any of the biopsy samples measured.

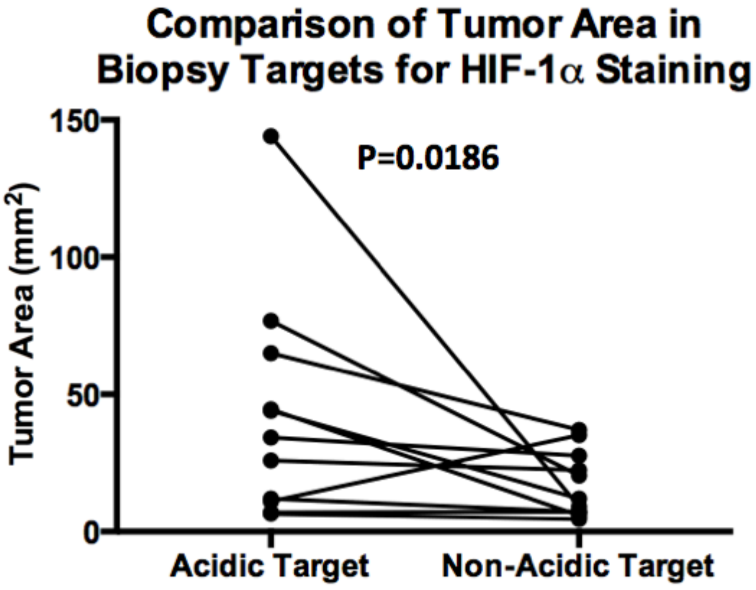

Figure 51. Comparison of the tumor area in acidic and non-acidic biopsy samples used for HIF-1α staining. Acidic biopsy samples have a significantly higher tumor area than non-acidic biopsy samples. This result remained significant (*P<0.05*) even when the acidic data point with the largest tumor area was removed.

One limitation inherent to acquiring image-defined biopsy targets is displacement of the tissue during surgery. When removing tissue, the biopsy target may shift significantly, resulting in uncertainty in the location of the measurement. Despite this, we have shown that image-guided biopsies can identify regions of increased Ki67 activity in a relatively small patient sample. A larger cohort of patients is needed to determine whether other histologic markers are elevated in regions of acidity as well.

vi. $\mathrm{MTR}_{\mathrm{asym}}$ Within Tumor Regions

In addition to biopsy target selection, tumor lesions on T1+C and FLAIR images were contoured to measure acidity characteristics of these tumor regions prior to surgery. Tumor contours were drawn using a semi-automated thresholding method. Briefly, a large ROI was drawn fully covering the tumor region. A thresholding step was then applied to retain voxels above a certain intensity, which varied for each image. Manual editing was then performed to further refine the tumor contour.

Because this patient cohort contained a mix of low- and high-grade tumors, T1+C enhancement was present on only eight out of eighteen biopsy patients. For these eight patients, a paired t-test was applied to determine whether $\mathrm{MTR}_{\mathrm{asym}}$ in regions of T1+C enhancement differed from $\mathrm{MTR}_{\mathrm{asym}}$ within the FLAIR lesion. Results are shown in Figure 52.

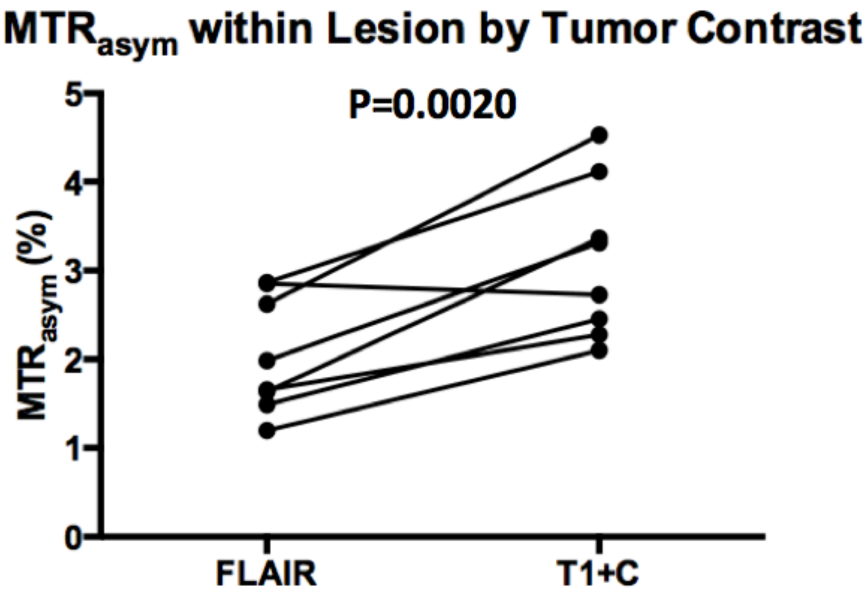

Figure 52. MTR$_{asym}$ within the region of enhancement on either FLAIR or gadolinium-enhancing images, as measured using our pH-weighted clinical CEST-EPI sequence (n=8). Regions of gadolinium enhancement have significantly higher MTR$_{asym}$.

MTR$_{asym}$ was significantly greater in regions of T1+C enhancement than in FLAIR enhancement (*P=0.0020*). This is likely due to the region of T1+C enhancement being more specific to aggressive, acidic high-grade tumor that has broken down the blood-brain barrier, while FLAIR enhancement can encompass both tumor and edematous tissue that may not be acidic.

We next aimed to determine whether MTR$_{asym}$ differed between different tumor grades. Because grade II and III tumors often do not show T1+C enhancement, the tumor region was defined by FLAIR enhancement in all patients for consistency. A one-way ANOVA test was performed to determine whether grade II, III, and IV tumors showed different tumor MTR$_{asym}$. Results are shown in Figure 53.

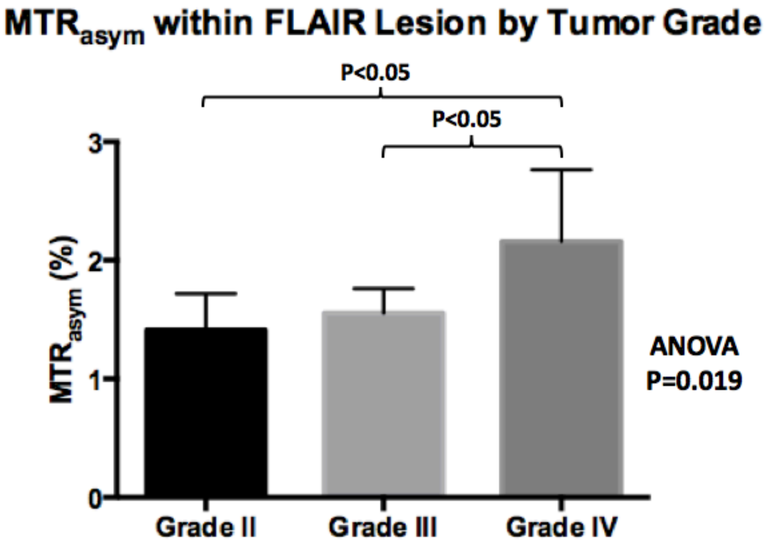

Figure 53. MTR$_{asym}$ within the region of FLAIR enhancement for grade II (n=4), grade III (n=7), and grade IV (n=7) tumors. One-way ANOVA showed a significant difference between tumor grades, likely due to increased MTR$_{asym}$ in grade IV tumors.

One-way ANOVA showed the three groups did significantly differ (Figure 53, *P=0.019*), with Tukey's multiple comparison tests showing that most of the variance appears to come from higher MTR$_{asym}$ in grade IV tumors compared with grades II and III (Grade II vs Grade III, *P>0.05*; Grade II vs Grade IV, *P<0.05*; Grade III vs Grade IV, *P<0.05*).

Grade III and IV tumors were then combined so as to compare low- and high-grade tumors using an unpaired t-test, although the low-grade tumor group was underrepresented with only four tumors compared to fourteen high-grade tumors. Grade II and III tumors were also combined to compare against grade IV tumors using an unpaired t-test. Results are shown in Figure 54.

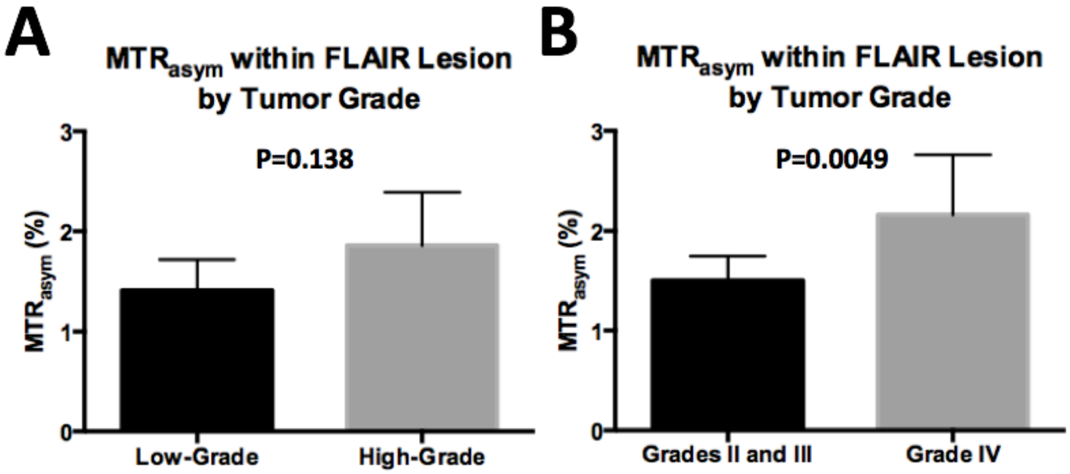

Figure 54. A) MTR$_{asym}$ within the region of FLAIR enhancement for low-grade (n=4) and high-grade (n=14) tumors. We did not observe a significant difference between the two groups. B) MTR$_{asym}$ within the region of FLAIR enhancement for grades II and III (n=11) and grade IV (n=7) tumors. MTR$_{asym}$ was significantly higher for grade IV tumors.

We did not observe a significant difference between low- and high-grade tumors (*P=0.138*). However, we did observe that grade IV tumors have significantly higher MTR$_{asym}$ within the FLAIR-enhancing region than grade II or III tumors (*P=0.0049*). Grade IV tumors are characterized by higher levels of hypoxia, vascularization, and proliferation than grade II and III tumors, which are traits associated with acidity. Therefore, it is intuitive that grade IV tumors display higher MTR$_{asym}$ on pH-weighted images.

Survival data for these pre-surgical patients are incomplete, as this data was acquired within 9 months of this writing and only four out of eighteen patients had progressed. However, when qualitatively looking at the data, we did not notice consistent trends between pre-surgical MTR$_{asym}$ within the T1+C or FLAIR enhancing regions and follow-up data. This may be due to this data being acquired pre-surgically, rather than post-surgically as the previous glioblastoma data had been when using the CEST-GRE sequence. This may indicate that even if a tumor is acidic, if that entire area is resected, it is the characteristics of the remaining tissue that indicate whether a patient will have short or long PFS. This data was also only acquired at a single time point, rather than at follow-up time points like the previous glioblastoma study. Because of this, a study using CEST-EPI at time points after surgical resection is warranted to determine whether the trends seen in our previous glioblastoma study are replicable.

However, there were some interesting cases in which acidic regions on pH-weighted images appeared to preempt the appearance of contrast enhancement on T1+C images. Figure 55 shows one example of a glioblastoma patient that had high acidity within a contrast enhancing lesion, but also had a highly acidic lesion nearby in a region that did not have T1+C enhancement and had some FLAIR enhancement but did not appear overly aggressive. This patient's region of T1+C enhancement was resected during surgery. Approximately 7 weeks after surgery, this patient had grown a large, necrotic enhancing lesion in the previous region of acidity.

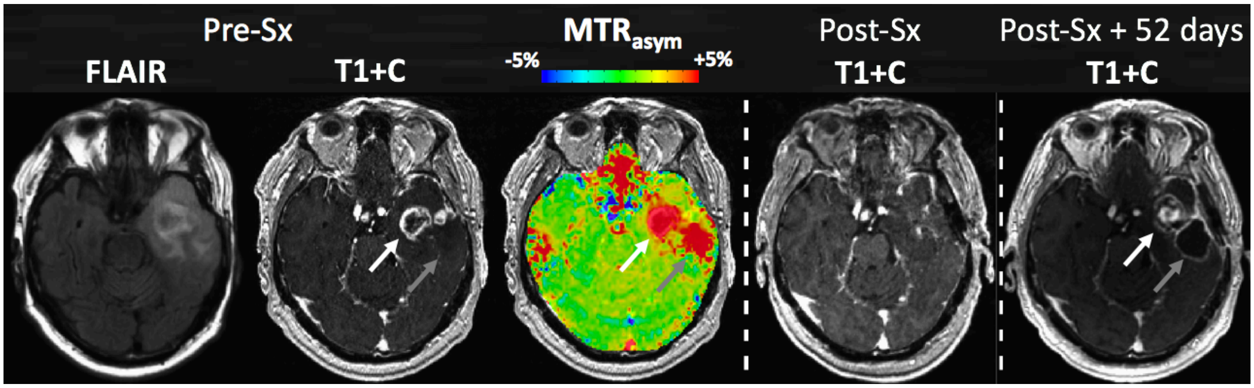

Figure 55. A glioblastoma patient with a contrast-enhancing lesion (white arrow) on T1+C at baseline (Pre-Sx). pH-weighed CEST-EPI showed elevated acidity within an adjacent region that did not appear contrast-enhancing on T1+C (gray arrow). Immediately after surgery, almost no T1+C enhancement remained (Post-Sx). However, several weeks after surgery, a contrast-enhancing lesion had developed in the adjacent region of acidity, which had not been resected.

Although not every patient who grew a new lesion of T1+C enhancement after surgery was predated by a strong acidic lesion at that location, our lack of serial or post-surgical data may have resulted in missing the appropriate time point for that information, again warranting further study with serial whole-brain data.

vii. Repeatability

An important aspect of developing new imaging techniques is verifying the repeatability of the obtained image contrast. Repeatability can describe the amount of intra-patient variability between data acquired either days apart or within the same day [148]. Within-day measurements may be taken back-to-back during the same scan session or after a short period of time in which the patient is removed from the scanner after the first measurement and repositioned before scanning again, a method referred to as the “coffee break” experiment [149]. Fortunately, the clinical CEST-EPI acquisition consists of two separate runs of the sequence, which are typically used for averaging and are separated by a one-minute S_0 acquisition. Comparison of the image contrast generated by the two runs of this sequence can provide a measure of the back-to-back repeatability of this technique.

To compare the signal intensity between two runs on a voxel-wise basis, the values of MTR_{asym} from each run were extracted from the FLAIR-hyperintense region of each of the 18 patients in the surgical biopsy study. This data underwent linear regression using a total least-squares (TLS) algorithm in Matlab. Results are shown in Figure 56.

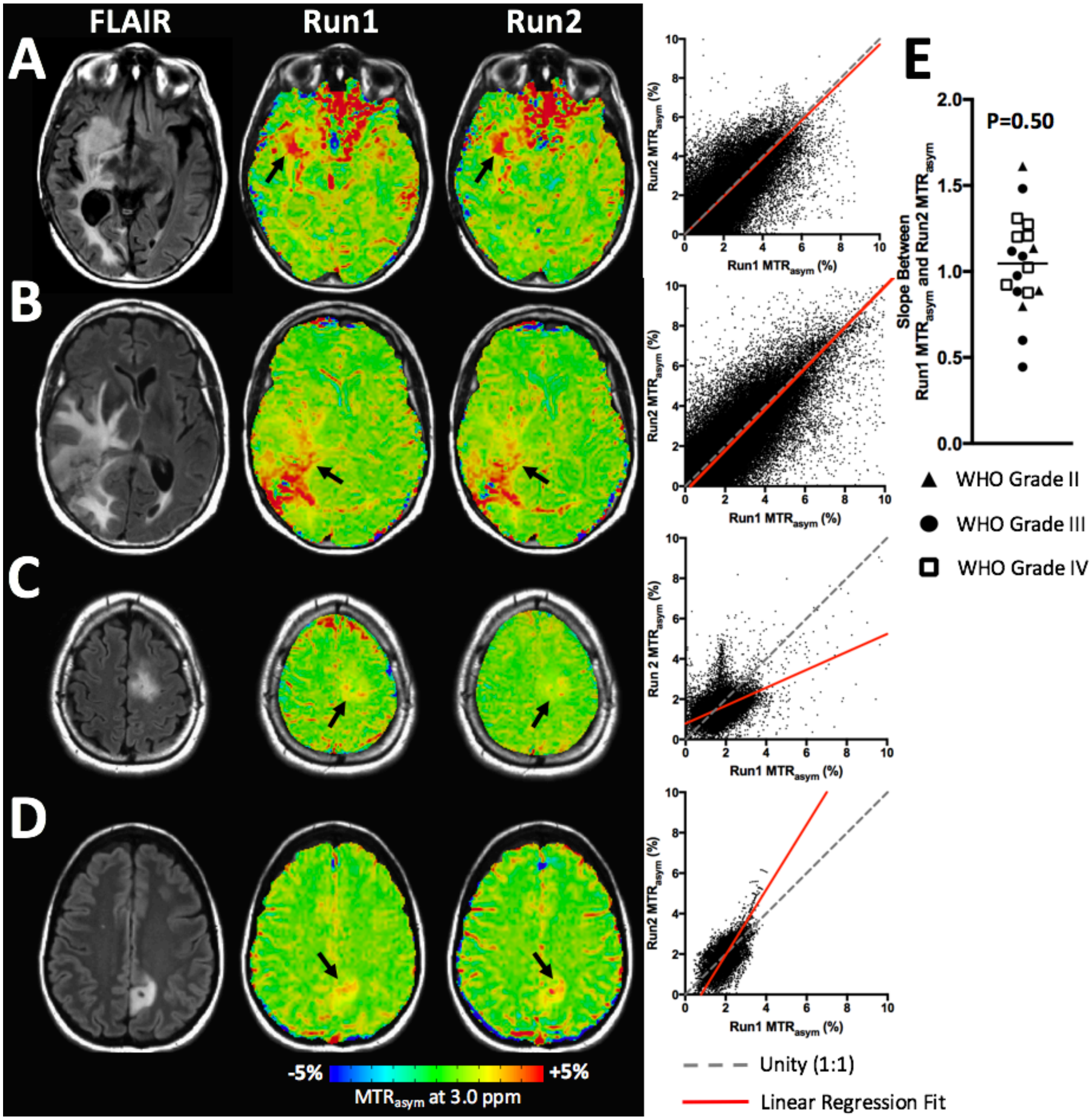

Figure 56. (A-D) Four glioma patients who received pH-weighted imaging. Scatterplots show a voxel-wise comparison of MTR_{asym} between runs, while the red line shows a linear fit to the data. Patients A&B showed high fidelity to a slope of unity while patients C&D did not. pH-weighted image contrast typically appeared similar between runs but appeared to vary between runs for some smaller, less acidic tumors. E) The slopes between Run1 and Run2 for all 18 patients. The mean slope across all patients was not significantly different from unity.

Across the patient cohort, slopes were not significantly different from unity (Figure 56E; mean slope = 1.05±0.29; *P=0.50*), suggesting there are not systematic differences between the runs. However, the slope in some cases differed from expected (Figures 56C&D). Qualitative inspection of these lesions suggested although they in some cases identified similar areas of elevated acidity, the magnitude of MTR_{asym} in these regions could vary, leading to a deviation from unity of over 50% between the two. This effect appeared more prevalent in smaller, less acidic tumors (Figures 56C&D) compared to larger, more acidic tumors. In these larger tumors, acidic contrast typically appeared similar between the two runs (Figures 56A&B).

To quantitatively identify acidic voxels using maps of MTR_{asym}, a region of contralateral NAWM was contoured on FLAIR images for each of the 18 patients used in the surgical biopsy study. MTR_{asym} was pulled from all voxels in this NAWM region from both runs for all 18 patients. These values were combined into a composite histogram to obtain the distribution of NAWM values across all patients. A 95% confidence interval was calculated for this distribution [150], which had an upper MTR_{asym} cutoff of 1.83%. Any voxels above this value were characterized as "acidic". We then applied this threshold to the FLAIR-hyperintense region for all 18 patients, for both runs of the sequence. By using the second run as a reference to the first, the number of true positive (TP), true negative (TN), false positive (FP), and false negative (FN) voxels within each FLAIR lesion were calculated. From this, four common metrics of tumor contour similarity were calculated: the Dice coefficient (2*TP/[2*TP+FP+FN]), sensitivity (TP/[TP+FN]), specificity (TN/[TN+FP]), and accuracy ([TN+TP]/[TN+TP+FP+FN]), for each patient [151]. Because neither run is inherently superior to the other, the first run was then used as a reference to the second and calculation of sensitivity and specificity was repeated, taking the mean sensitivity and specificity between the two runs as the final value. The Dice coefficient and accuracy remain the same regardless of which run is used as the reference. The acidic fraction for each run was then obtained by dividing the acidic volume by the total volume of the FLAIR lesion and the intraclass correlation coefficient (ICC) of these acidic fractions was calculated [152]. Results for all patients are shown in Figure 57.

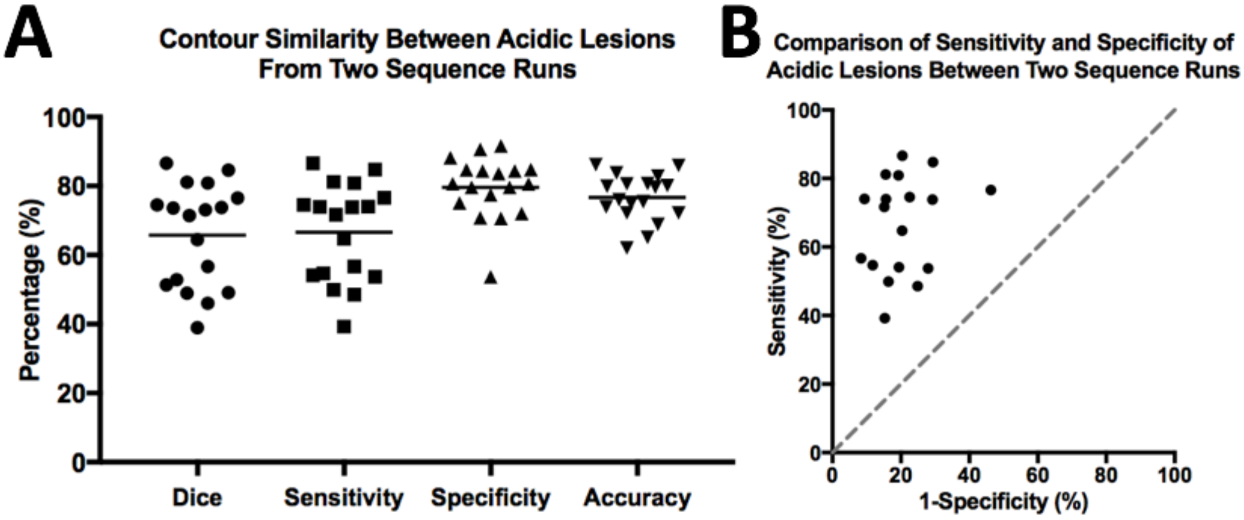

Figure 57. A) Four measures of contour similarity (Dice coefficient, sensitivity, specificity, and accuracy) between acidic volume contours calculated from two runs of the clinical CEST-EPI sequence. B) A comparison of the sensitivity and specificity of acidic or non-acidic voxels in one run being identified correctly when using the other run as a reference.

This patient cohort had a mean Dice coefficient of 66±14%, a mean sensitivity of 67±14%, a mean specificity of 80±9%, and a mean accuracy of 77±7%. The higher values of specificity and accuracy compared with the Dice coefficient and sensitivity suggest the acidic threshold is fairly selective and consistently classifies many voxels within the lesion as non-acidic, but may miss detection of some voxels which should be classified as acidic. A comparison of the acidic fractions between runs yielded an ICC of 0.87±0.09, which differed significantly from zero (*P<0.0001*) and is regarded as a high correlation [153-155].

There are a number of reasons pH-weighted contrast may change between runs. Head motion during either of the runs may result in misalignment of the z-spectral volumes prior to asymmetry analysis. Although these data are motion corrected prior to analysis, artifacts from misalignment may persist. Even when z-spectral volumes within a run are aligned, head motion between the runs may result in a shift in the location of acidic lesions as well, as both runs are registered to anatomical images using the same transform. Additionally, this analysis was performed only for a single run of the CEST-EPI sequence; for all other analyses, both runs are averaged after calculation of MTR_{asym}. A true analysis of the repeatability of our data would involve comparisons of these averaged scans. For a more complete description of the repeatability of pH-weighted image contrast for this particular protocol, future collection of four repeated acquisitions in patients is necessary. Removal and repositioning of the subject prior to the repeat scans (i.e. the coffee break experiment) may also allow for a more robust measure of repeatability compared to back-to-back scanning.

viii. Comparison of Common Quantitative Imaging Contrasts

A goal in the development of novel imaging techniques is to provide unique or supplemental contrast compared with currently available image contrasts. Therefore, we compared this pH-weighted imaging technique against common imaging techniques including quantitative T_2 mapping, diffusion imaging, and perfusion imaging. Maps of ADC, T_2, CBF, and CBV were registered to each patient's FLAIR image. Maps of CBF and CBV were normalized by drawing an ROI in a region of NAWM and dividing the values of each map by the mean value within the NAWM region. Values of ADC, T_2, CBF, and CBV were then pulled from the FLAIR-enhancing region and plotted against MTR_{asym} on a voxel-wise basis.

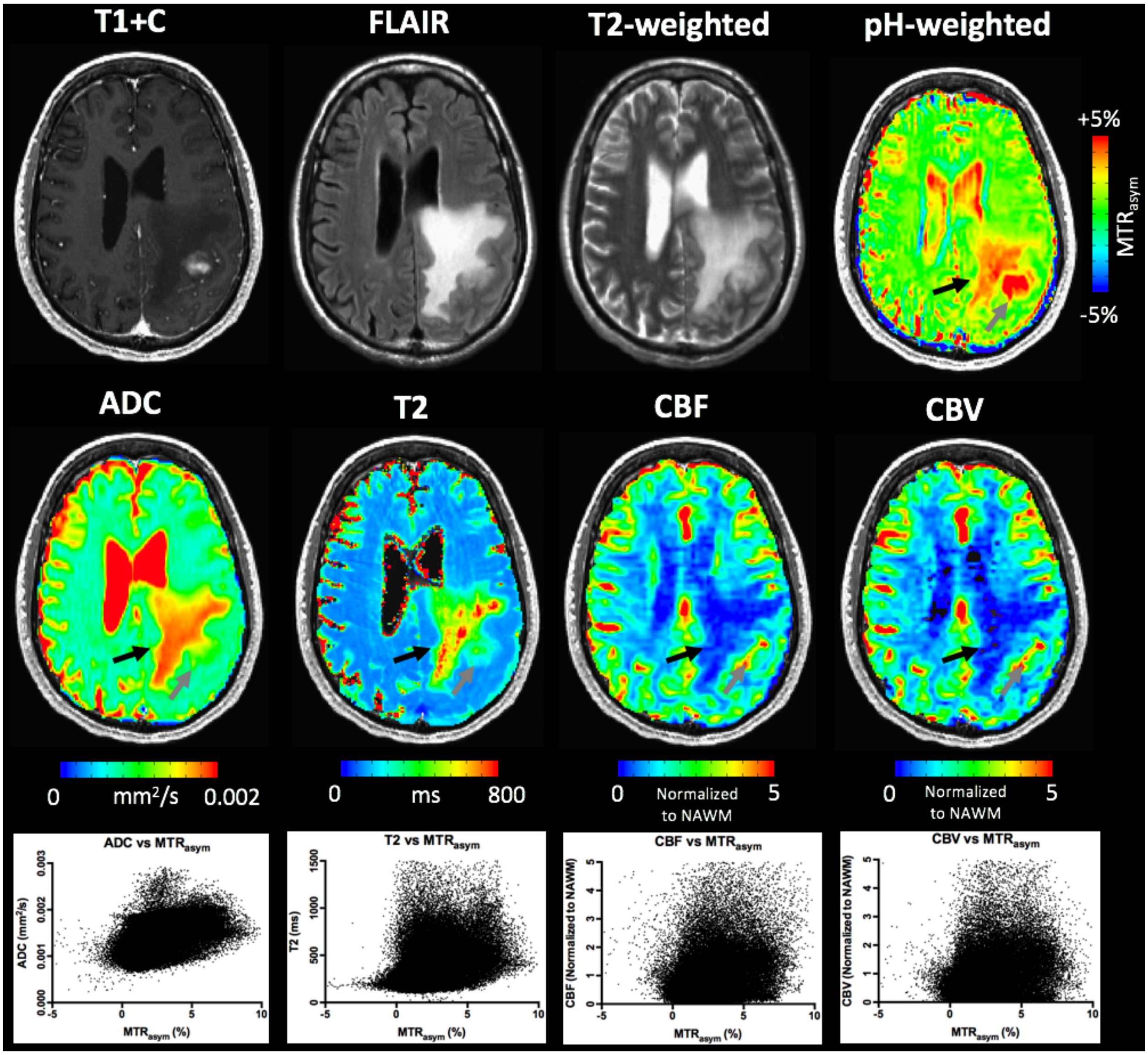

Figure 58. Comparison of quantitative image contrasts in a patient with GBM. Anatomical images show a gadolinium-enhancing nodule along with a larger region of FLAIR enhancement. The FLAIR-enhancing region shows elevated MTR_{asym}, ADC, and T2, along with hypoperfusion on CBF and CBV maps (black arrow). pH-weighted imaging shows a highly acidic lesion in the gadolinium enhancing nodule that is not hyperintense on ADC or T_2 maps (gray arrow). Scatterplots show an apparent trend between MTRasym and ADC but not T_2, CBF, or CBV.

Results for a patient with GBM are shown in Figure 58. pH-weighted MRI showed a highly acidic lesion in the area of T1+C enhancement and more diffuse acidity in the region of FLAIR enhancement. ADC and T_2 maps both showed elevated values within the FLAIR-enhancing region, but did not show highly elevated values in the highly acidic nodule. This suggests that pH-weighted imaging provides unique contrast compared to these two metrics. Despite this, scatterplots showed an apparent trend between increased ADC and increased MTR_{asym}. This trend was not visible on T_2 scatterplots. Perfusion imaging showed decreased CBF and CBV within the FLAIR-enhancing region. This suggests hypoxia in this region, which may result in increased acidity as seen on pH-weighted images. However, a relationship between MTR_{asym} and increased CBF or CBV were not apparent on scatterplots.

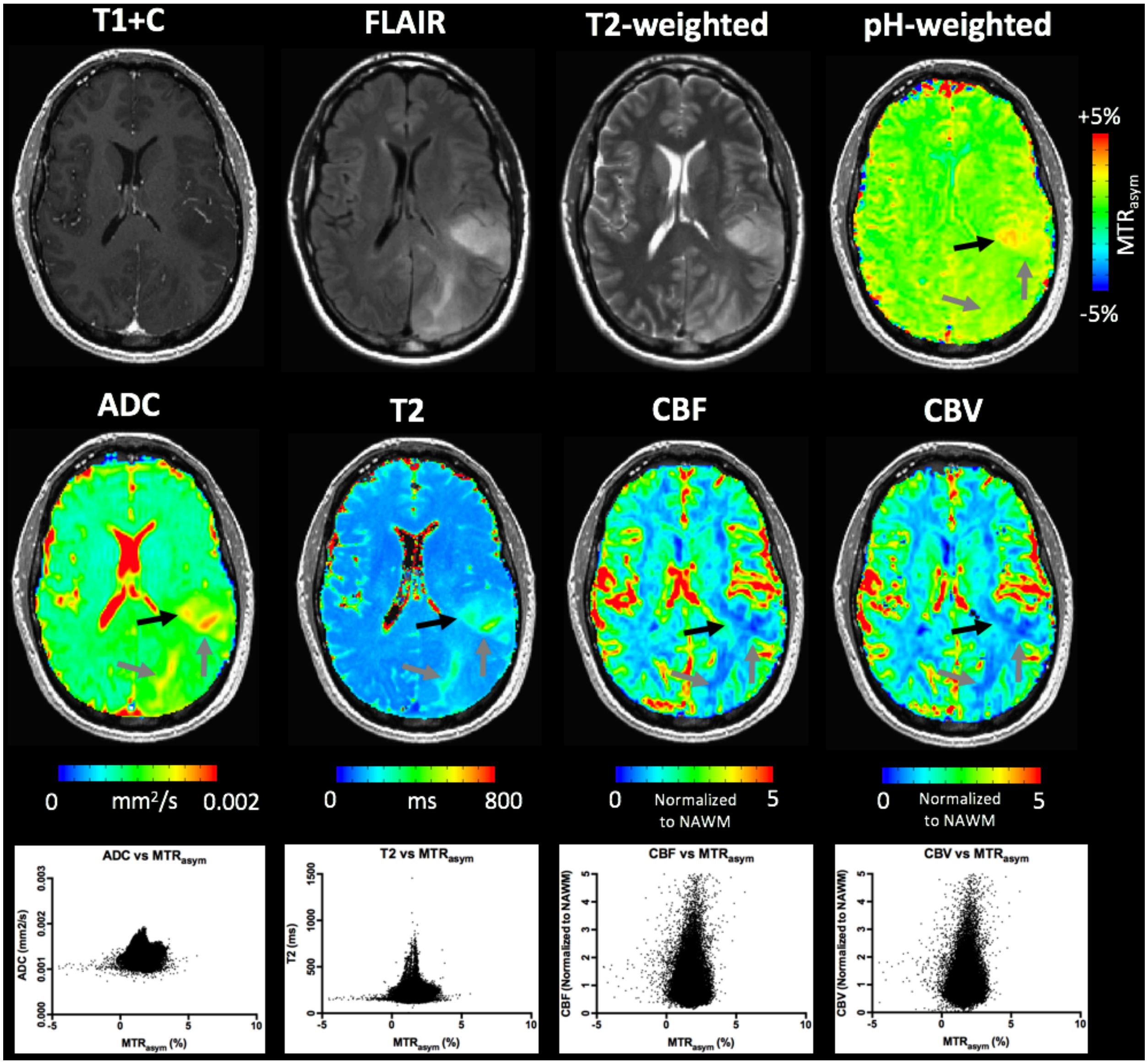

Figure 59. Comparison of quantitative image contrasts in a patient with anaplastic glioma. Anatomical images show a diffuse area of FLAIR enhancement. An acidic nodule can be seen that is also hyperintense on ADC and T_2 maps (black arrow). However there are two additional lesions present on ADC and T_2 maps that are not present on pH-weighted MRI (gray arrows). Maps of CBF and CBV largely show hypoperfusion in the FLAIR-enhancing area. Scatterplots did not show any apparent relationship between MTR_{asym} and the other four quantitative imaging metrics.

Results for a patient with anaplastic glioma are shown in Figure 59. pH-weighted MRI showed a small acidic lesion within one region of FLAIR enhancement but not the remaining diffuse FLAIR enhancement. ADC and T_2 maps both appeared to show elevated contrast in this acidic region as well as two other non-acidic regions within the FLAIR-enhancing area. Scatterplots did not show any apparent relationship between MTR_{asym} and ADC or T_2. Perfusion maps again showed decreased CBF and CBV within the FLAIR-enhancing area, although the scatterplots again did not show an apparent relationship between MTR_{asym} and CBF or CBV.

These examples indicate that pH-weighted MRI provides unique contrast compared with other quantitative MRI techniques. Survival analysis of this patient cohort is warranted once survival data are complete to determine whether pH-weighted MRI can show increased predictive value of PFS and OS compared to these more traditional quantitative contrasts.

ix. ^{18}F-FDOPA PET in Surgical Biopsy Patients

PET imaging using ^{18}F-FDG is the most commonly used radiotracer method for examining metabolic activity of malignant tumors. Despite its widespread use in oncology, ^{18}F-FDG often provides relatively poor contrast in the brain between background tissue and tumor because of high uptake in normal brain tissue [156]. 3,4-dihydroxy-6-[^{18}F]-fluoro-L-phenylalanine (^{18}F-FDOPA) is an amino acid analog PET radiotracer. Compared with ^{18}F-FDG, ^{18}F-FDOPA has shown improved contrast between tumor and normal brain tissue in patients with high-grade glioma because of elevated amino acid transportation in malignant tumor cells [157]. We have previously shown that ^{18}F-FDOPA PET uptake can serve as a biomarker for survival in GBM patients undergoing treatment with bevacizumab [150] (Figure 60).

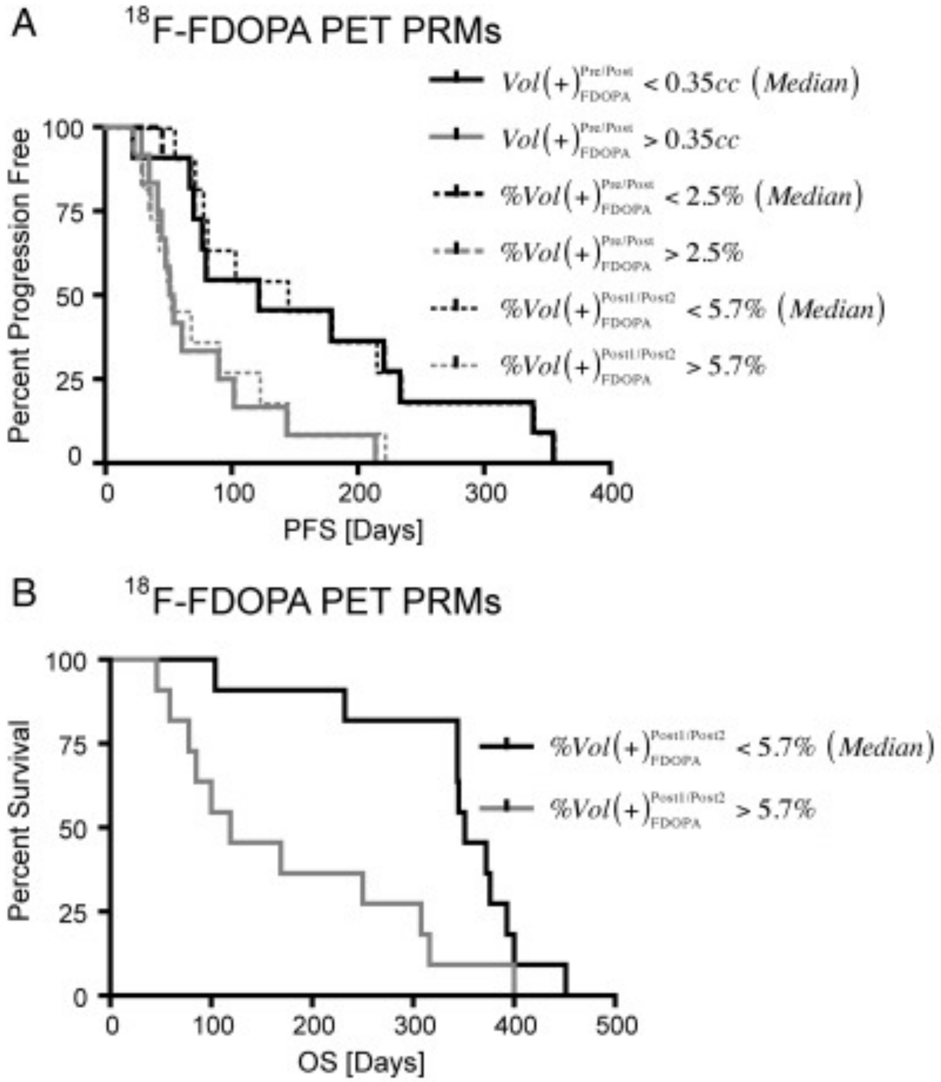

Figure 60. Quantitative analysis of serial ^{18}F-FDOPA PET data can be used to stratify overall (A) and progression-free (B) survival in GBM patients (n=24) [150]. Stratifications shown in this figure have a statistical significance of $P<0.05$.

In addition, other studies have shown that ^{18}F-FDOPA can be predictive of tumor grade and proliferative activity [158]. We therefore hypothesized that regions of increased ^{18}F-FDOPA uptake may correlate with regions of increased pH-weighted contrast. This correlation may also occur due to the fact that ^{18}F-FDOPA is an amino acid analog, and amines of the type found on amino acids are targeted during pH-weighted imaging. Because ^{18}F-FDOPA PET imaging requires the use of an exogenous and radioactive tracer, noninvasive and endogenous imaging methods like amine CEST are preferred for identifying these regions of tumor. Furthermore, CEST MRI has higher spatial resolution than PET imaging in general, allowing for finer delineation of the tumor contrast. During the course of our human subject data collection, ^{18}F-FDOPA PET data were acquired whenever possible.

Quantitative Comparison of ^{18}F-FDOPA Uptake With Acidic Tissue

Eight patients received ^{18}F-FDOPA PET imaging within one month of their pre-operative MRI, which included pH-weighted CEST-EPI. Previous studies have shown that ^{18}F-FDOPA data can be normalized to the basal ganglia to account for differences in body weight and injected dose, as the basal ganglia take up a large amount of the tracer that is relatively consistent across the population [150]. Therefore, all ^{18}F-FDOPA PET data were normalized by drawing an ROI on the basal ganglia and extracting the mean uptake value from this ROI. If the tumor region approached the location of the basal ganglia, that hemisphere's ganglion was not used. After normalization, PET data was registered to the patient's T1+C image. As each of these patients had FLAIR data acquired as well, each FLAIR image was registered to its corresponding T1+C image. Tumor contours were then drawn on each FLAIR image using the semi-automated thresholding method described previously. FLAIR data were used because five of these tumors were non-enhancing on T1+C images. For each voxel within the FLAIR-hyperintense region, normalized ^{18}F-FDOPA PET uptake as well as MTR_{asym} at 3.0 ppm were extracted and plotted against each other for each patient. Linear regression was then performed on the data to determine whether there was a positive relationship between MTR_{asym} and ^{18}F-FDOPA uptake. Scatterplots for all eight patients are shown in Figure 61.

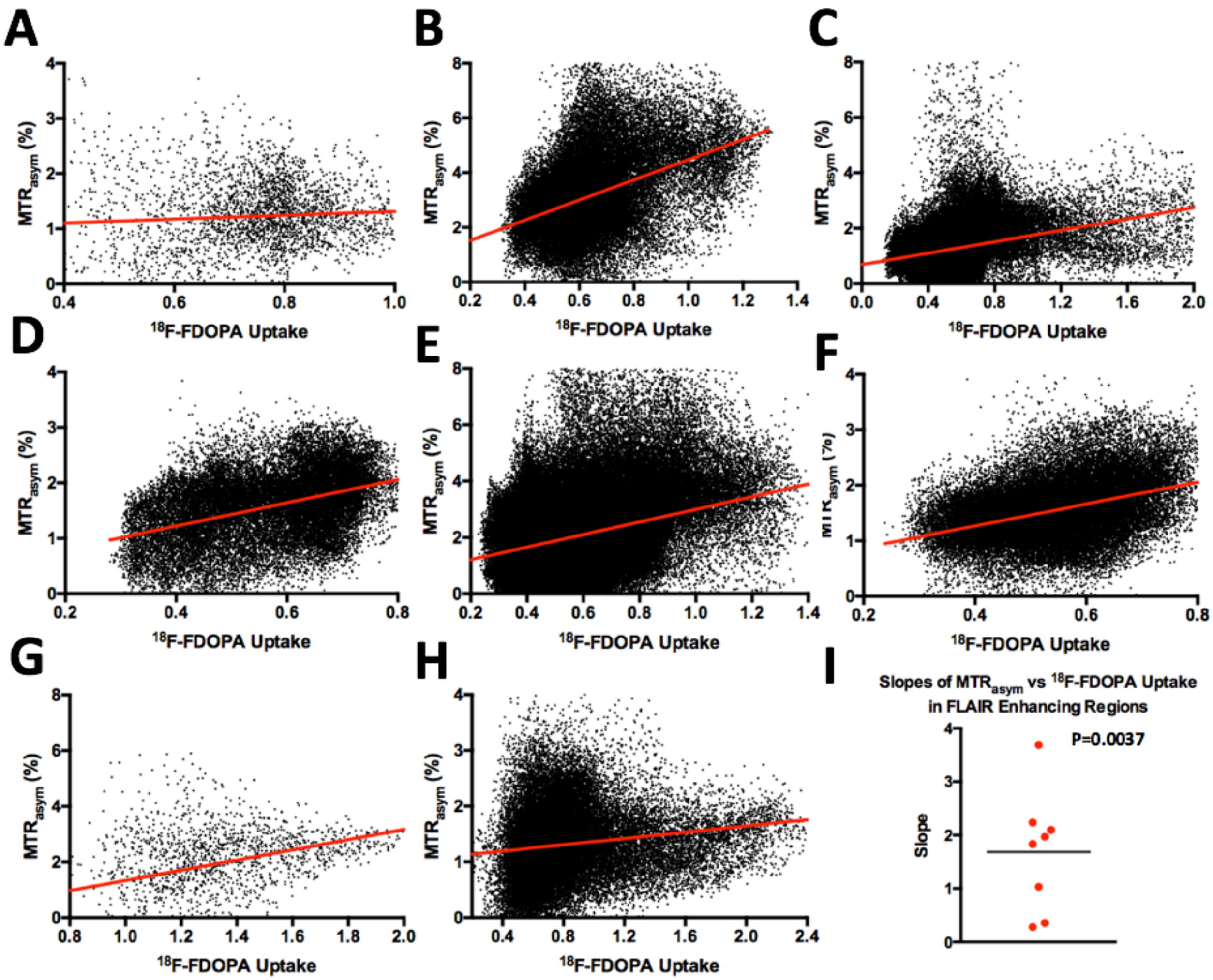

Figure 61. (A-H) Scatterplots comparing ^{18}F-FDOPA uptake to MTR$_{asym}$ on a voxel-wise basis within the FLAIR-enhancing regions of eight glioma patients. Axes differ between patients to provide the best visualization of the data for each patient. ^{18}F-FDOPA uptake has been normalized to uptake in the basal ganglia (BG). The slope obtained by linear regression of the data is shown in red. I) The slopes obtained by linear regression of the data for patients A-H are all greater than zero.

For all eight patients, the slope between MTR$_{asym}$ and ^{18}F-FDOPA uptake within the FLAIR-enhancing region was positive (Figure 61), suggesting a general trend between increased ^{18}F-FDOPA uptake and increased MTR$_{asym}$. A one-sample t-test revealed that these slopes differed significantly from zero, with a mean of 1.69±1.12 (Figure 61I; *P=0.0037*), supporting this hypothesis.

To further test this quantitatively, both the upper 20% threshold and lower 20% threshold for ^{18}F-FDOPA uptake values within the FLAIR-enhancing region was calculated for each patient. Mean MTR$_{asym}$ values within these regions were then calculated separately, hypothesizing that the region of high ^{18}F-FDOPA uptake values would have higher mean MTR$_{asym}$ than the region of low ^{18}F-FDOPA uptake values. A paired t-test was used to determine whether high-uptake and low-uptake regions had significantly different MTR$_{asym}$.

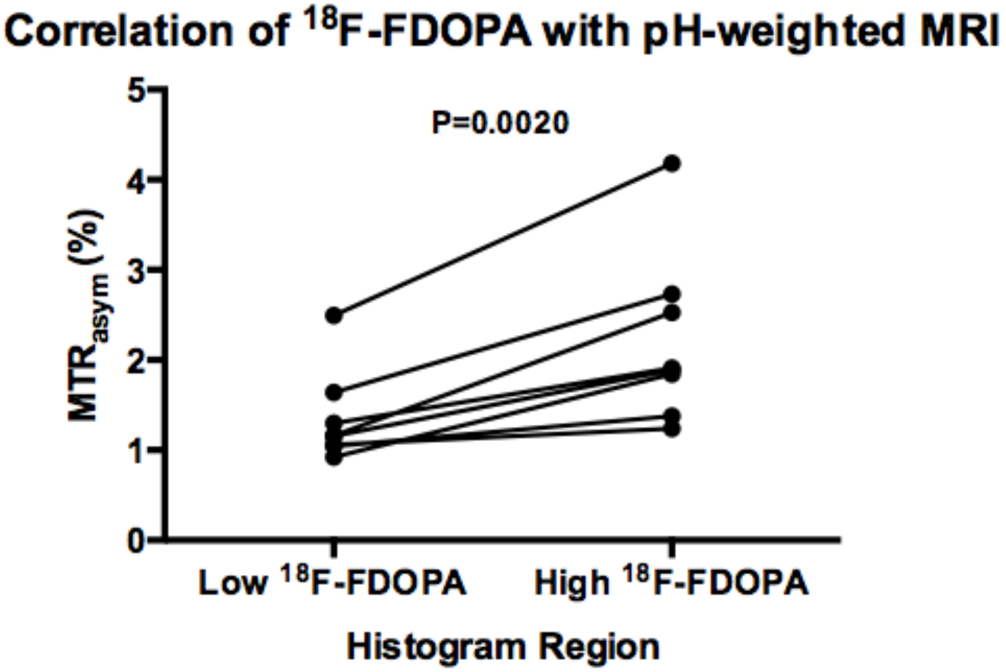

Figure 62. Within the FLAIR-enhancing region of eight glioma patients, MTR$_{asym}$ is higher within the upper 20% of ^{18}F-FDOPA uptake values than within the lower 20% of ^{18}F-FDOPA uptake values, indicating an overall correlation between ^{18}F-FDOPA uptake and acidity as measured by pH-weighted MRI.

Results showed that regions of high tracer uptake had significantly higher MTR_{asym} than regions of low tracer uptake (Figure 62, *P=0.0020*). Additionally, MTR_{asym} was higher in high-uptake regions than in low-uptake regions for all eight patients with available ^{18}F-FDOPA PET data. Examples of patients with pH-weighted MRI and ^{18}F-FDOPA PET data are shown below.

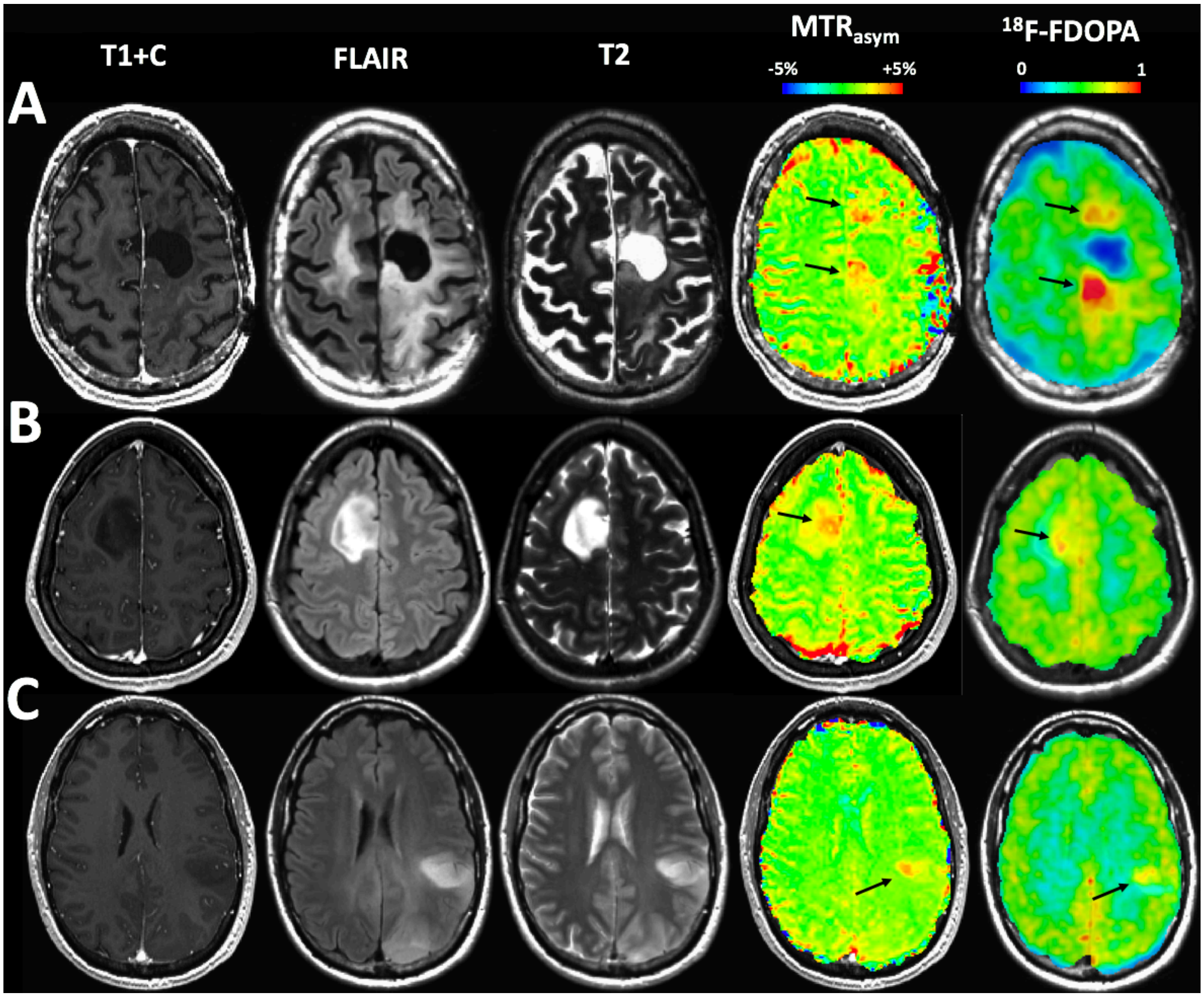

Figure 63. Three malignant glioma patients with ^{18}F-FDOPA lesions co-localized with acidic lesions seen on pH-weighted MRI (black arrows). ^{18}F-FDOPA uptake is normalized to the basal ganglia.

Qualitative Comparison of ^{18}F-FDOPA PET and pH-weighted MRI in Human Gliomas

Figure 63 shows three patients with ^{18}F-FDOPA lesions closely matching acidic lesions seen on pH-weighted imaging. In all three of these cases, the tumor was an anaplastic oligoastrocytoma (WHO grade III) and was non-enhancing on T1+C but enhancing on FLAIR. Figure 63A shows two distinct lesions co-localized on both pH-weighted MRI and PET anterior and posterior to an abnormally large ventricle. While both of these regions are enhancing on FLAIR, there are many other regions enhancing on FLAIR that do not display these elevated acidic or elevated ^{18}F-FDOPA uptake characteristics. Figures 63B&C appear to show a nodule within the FLAIR lesion that is enhancing on both pH-weighted MRI and PET, while other FLAIR-enhancing regions appear normal on pH-weighted MRI and PET.

However, pH-weighted data appeared to provide unique information compared with PET in two out of the eight patients examined. Figure 64 shows two patients with GBM. The patient in Figure 64A appears to have a large posterior lesion in the right hemisphere on both pH-weighted MRI and PET. However, another lesion can also be seen on PET superior to this that is not apparent on pH-weighted MRI. Conversely, the patient in Figure 64B shows a single lesion on PET within the FLAIR-enhancing area, but appears to show two distinct regions of high acidity on pH-weighted MRI. This suggests that although pH-weighted MRI and ^{18}F-FDOPA are often sensitive to the same lesions, they can sometimes provide complimentary information as well.

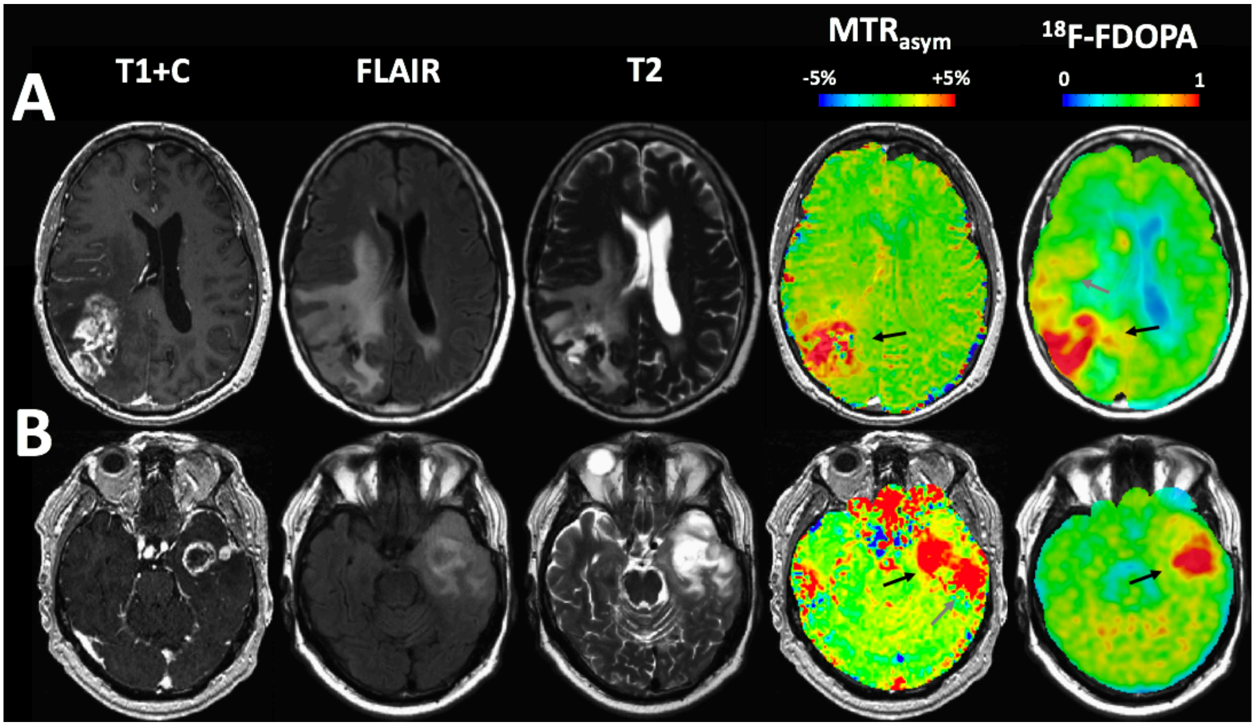

Figure 64. Two GBM patients each with an ^{18}F-FDOPA lesion that is co-localized with an acidic lesion seen on pH-weighted MRI (black arrows). Patient A has an additional lesion seen on PET that is not present on pH-weighted MRI (gray arrow), and patient B has an additional lesion seen on pH-weighted MRI that is not present on PET (gray arrow). ^{18}F-FDOPA uptake is normalized to the basal ganglia.

x. pH-weighted Imaging in Patients Treated with Bevacizumab

GBMs and other malignant gliomas flourish and accelerate their growth rates by both co-opting existing vasculature and inducing neovascularization [159, 160], primarily through the overexpression of vascular endothelial growth factor (VEGF). VEGF is a signal protein that stimulates angiogenesis, and its overexpression can allow for the growth of new blood vessels to supply tumors with an adequate blood supply as they increase in size. Because of this, a class of therapeutics has been developed to combat the formation of these new blood vessels. Bevacizumab is a humanized monoclonal antibody to VEGF and is currently the only anti-angiogenic agent FDA-approved for use in recurrent in GBM [161]. Bevacizumab is often used as a second-line treatment when standard radiotherapy and concurrent temozolomide has failed. As anti-angiogenic agents are expected to have a significant and direct impact on tumor vasculature, there is a growing interest in biomarkers for evaluating the changes in tumor characteristics following treatment.

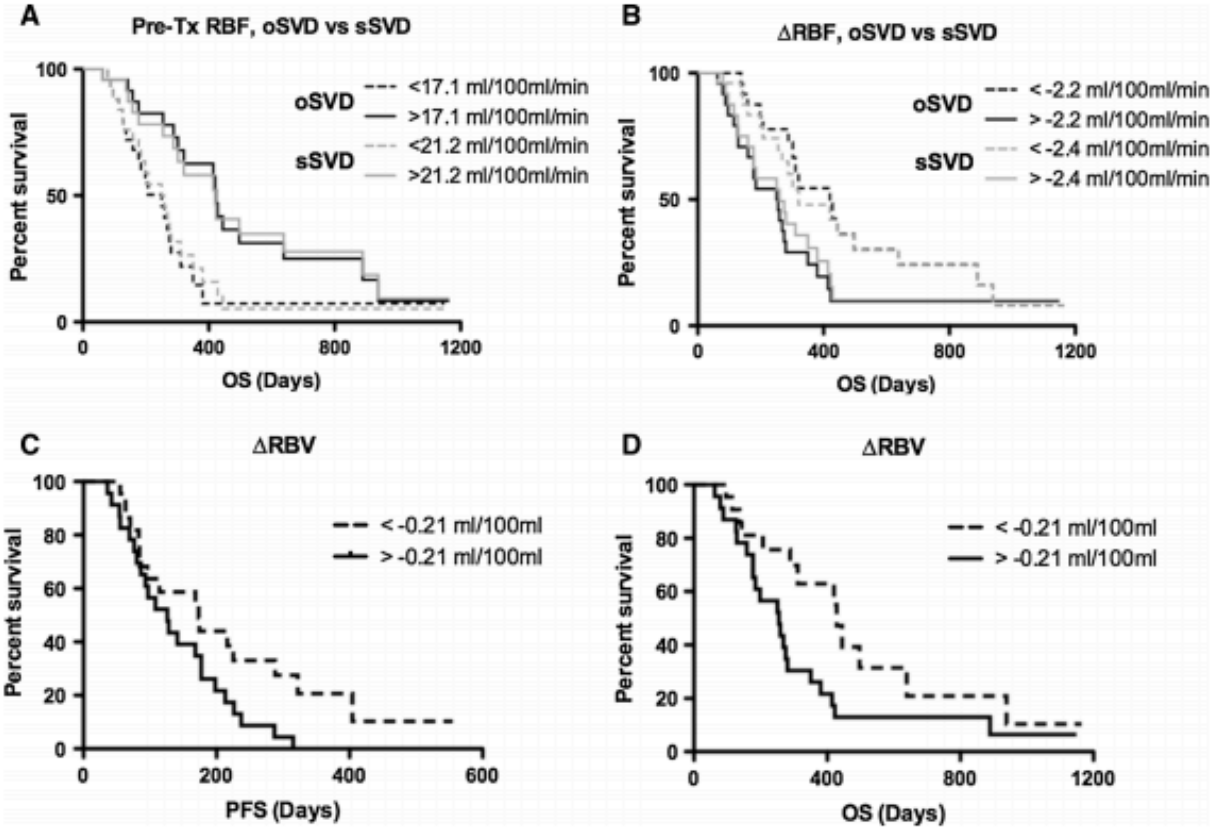

Figure 65. Changes in relative CBV (RBV) and relative CBF (RBF) following treatment with bevacizumab can stratify GBM patients (n=45) by overall and progression-free survival [162]. oSVD and sSVD represent perfusion deconvolution methods that are discussed in the publication.

We have recently shown that changes in cerebral blood volume (CBV) and cerebral blood flow (CBF) can stratify GBM patients by overall and progression-free survival following treatment with bevacizumab [162] (Figure 65). Although our results suggested that a decrease in CBV and CBF following treatment was associated with an improved prognosis, it remains unclear whether the anti-angiogenic therapy results in increased hypoxia in the tumor region or whether it results in a normalization of the vasculature by removing leaky and abnormal blood vessels while repairing the blood-brain barrier. Some evidence exists that either situation might occur depending on the individual patient. As acidity of the microenvironment is a downstream characteristic of hypoxia as described earlier, we might expect changes in hypoxia to result in changes in pH-weighted image contrast following treatment with bevacizumab. Therefore, we implemented pH-weighted CEST-EPI in GBM patients undergoing treatment with bevacizumab to determine what changes occurred.

Data Acquisition in Bevacizumab Patients

Treatment with bevacizumab often results in a reduction in the volume of tumor contrast enhancement, CBV, and CBF as the vasculature is normalized and the growth of leaky blood vessels is inhibited. As these changes in the tumor microenvironment may cause alterations in pH, we tested whether pH-weighted image contrast changes following bevacizumab treatment, and whether growing acidic regions on serial CEST MRI scans can be predictive of future tumor growth as seen on anatomical MRI.

Patients with recurrent GBM who were selected for treatment with bevacizumab were enrolled in this prospective study. All patients gave informed consent and this trial was compliant with the Health Insurance Portability and Accountability Act and approved by the institutional review board at our institution. As of this writing, three patients have been enrolled. All patients received anatomical MRI on a 3T MR system (Siemens 3T Prisma) that included pre- and post-contrast (Gd-DTPA at a dose of 0.1 mmol/kg body weight; Magnevist) axial T_1-weighted two-inversion contrast MPRAGE (MP2RAGE), axial T_2-weighted, and axial FLAIR sequences. In addition to anatomical MRI, patients received multi-b-value DWI with b-values ranging from 0 to 5000 s/mm^2; q-space imaging, another form of DWI that was not used in this analysis; and DSC-MRI. Patients also received a pH-weighted CEST-EPI scan. Enrolled patients received a pre-treatment scan within one week prior to bevacizumab treatment and a post-treatment scan approximately six weeks following the start of treatment. Standard clinical scans were then acquired following these research scans whenever clinically indicated.

For each time point, CEST-EPI data was post-processed as described previously to generate maps of MTR_{asym}. FLAIR and T_2-weighted images were registered to the post-contrast MPRAGE image, with the second inversion of the MP2RAGE sequence used as the MPRAGE image. T_1 subtraction maps were calculated by normalizing the pre- and post-contrast MPRAGE images to z-score images, registering the pre-contrast image to the post-contrast image, and then subtracting the pre-contrast image from the post-contrast image [144]. This T_1 subtraction map technique has the effect of increasing the contrast-to-noise of contrast enhancement in the tumor region compared to the surrounding tissue as well as reducing unwanted T_1 shortening effects. The tumor region was contoured on both FLAIR and post-contrast T_1-weighted images using a semi-automated thresholding method. The mean MTR_{asym} value was extracted from within these contours to determine whether the pH-weighted contrast changes following treatment. Also, serial images including follow-up clinical images were qualitatively examined to determine whether changes in pH-weighted CEST MRI could be predictive of future tumor growth.

Bevacizumab Patient Results

All three patients showed a reduction in $\mathrm{MTR_{asym}}$ within the FLAIR-hyperintense region following treatment, with a mean reduction of 0.53±0.45%. All three patients also showed a reduction in $\mathrm{MTR_{asym}}$ within the contrast-enhancing region following treatment, with a mean reduction of 0.79±0.83%. Qualitatively, we observed an overall decrease in acidity following treatment within the tumor region (Figure 66).

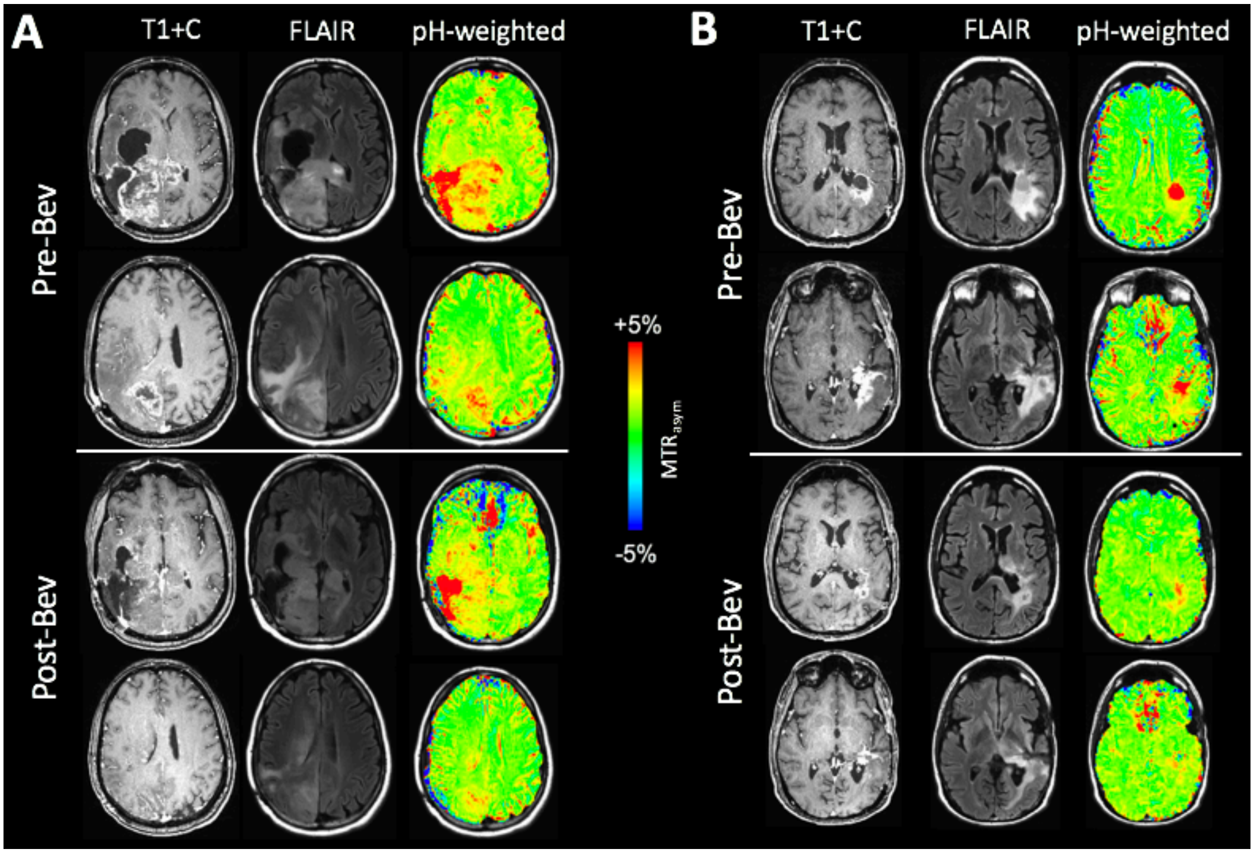

Figure 66. Anatomic and pH-weighted data for two recurrent GBM patients (A&B) both before and after treatment with bevacizumab. A reduction in pH-weighted image contrast within the tumor region is seen following bevacizumab therapy in both patients.

Interestingly, we also saw that in two of the three patients, the appearance of an acidic lesion preceded the appearance of a contrast-enhancing lesion in the same location. Figure 67 shows a bevacizumab patient with a highly acidic necrotic core at baseline and post-treatment, who develops a smaller acidic lesion adjacent to the necrotic core on the post-treatment scan, despite a lack of contrast enhancement on the T_1 subtraction image. At two follow up time points, a contrast-enhancing lesion has appeared in that location and appears to be growing in size.

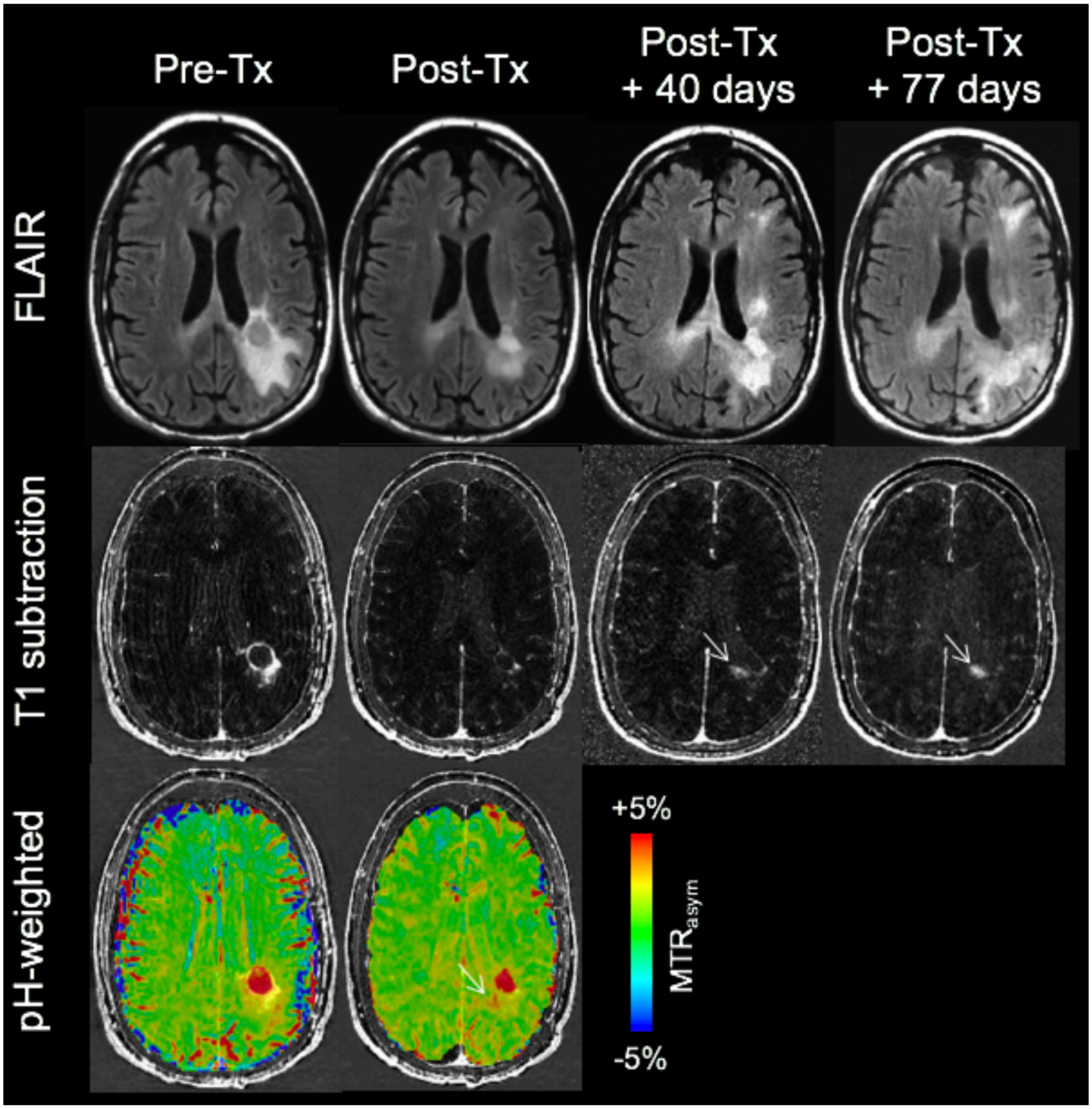

Figure 67. Serial anatomic and pH-weighted data for a recurrent GBM patient treated with bevacizumab.

Figure 68 shows a bevacizumab patient with a contrast-enhancing lesion at baseline that that shows greatly reduced contrast enhancement following treatment. The contrast-enhancing lesion shows a strongly acidic signature at baseline, and although the post-treatment scan also shows an acidic lesion in this region, it shows a reduction in acidity compared to baseline.

However, the post-treatment scan also shows an acidic lesion appearing superior to the right ventricle, despite a lack of contrast enhancement in this region on the T_1 subtraction image. After two follow-up time points, a contrast-enhancing lesion has again appeared in this area and appears to be growing in size, while the region that showed a reduction in acidity following treatment is not developing further contrast enhancement. Similar to the results from the cohort of patients imaged using single-slice CEST-GRE, these results suggest that changes in acidity as measured with serial CEST-EPI can be predictive of future tumor growth.

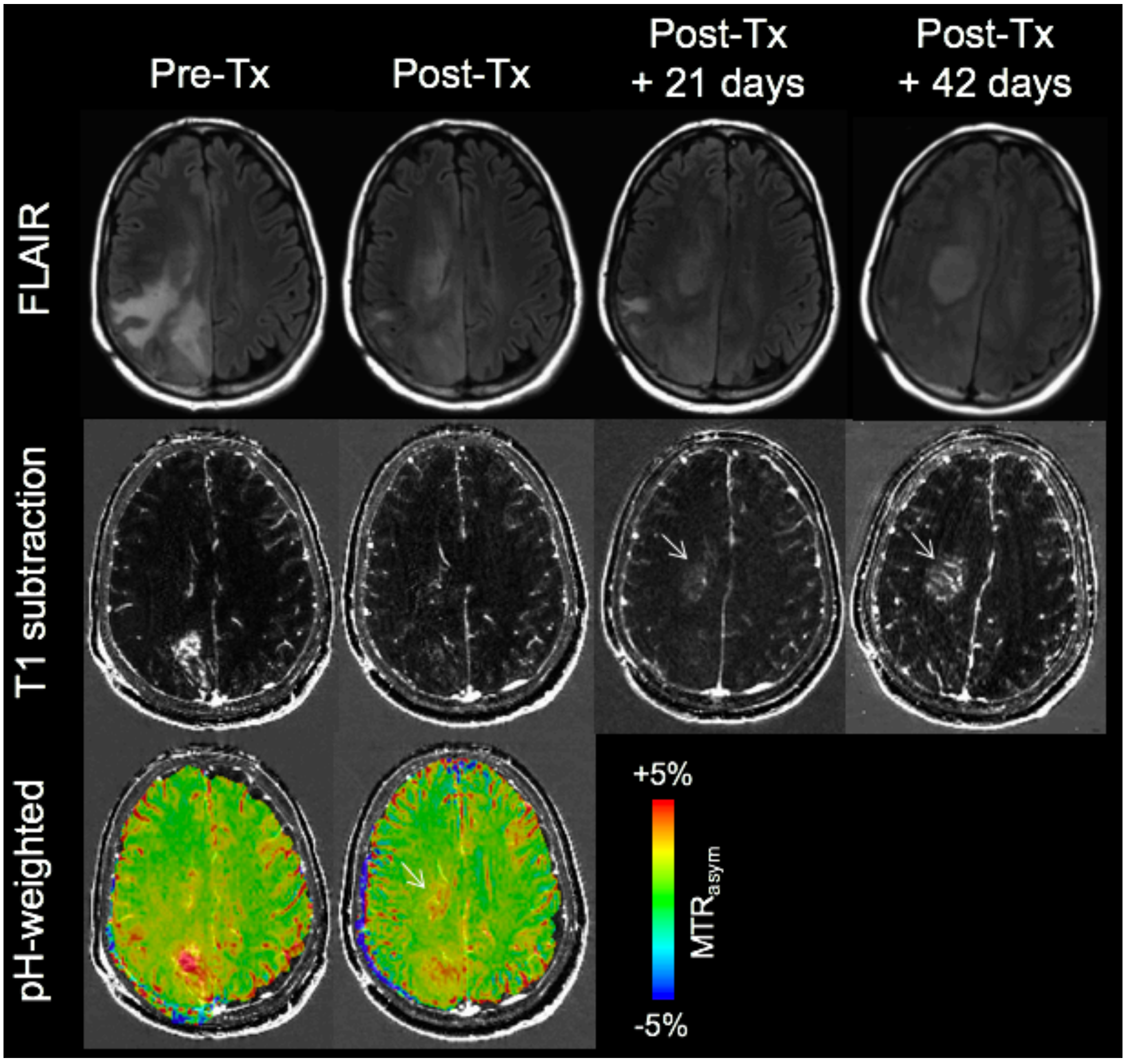

Figure 68. Serial anatomic and pH-weighted data for another recurrent GBM patient treated with bevacizumab.

CHAPTER VI

Advanced CEST Techniques

Development of novel and creative imaging techniques is essential to forward progress in the radiological sciences. In this chapter, we explore two recently developed advancements that build upon pH-weighted CEST imaging.

i. Multi-Echo CEST-EPI

Our group has recently developed a quadruple-echo EPI readout for use in dynamic susceptibility contrast (DSC) perfusion imaging. This readout employs two gradient echoes at 14.0 ms and 34.1 ms, followed by an asymmetric spin echo at 58.0 ms and a standard spin echo at 92.4 ms. From this information, the readout echoes can be used to calculate quantitative T_2* maps [163] from the gradient echo data and T_2 maps from the spin echo data. By implementing this quadruple echo readout in our CEST-EPI sequence, we can obtain these spin echo contrasts in addition to the first two echoes which provide a similar information to our traditional CEST-EPI readout. As short and long echoes are sensitive to more and less restricted water molecules, respectively, these echoes can in theory provide information on different tissue components.

Multi-echo CEST EPI was implemented clinically in a cohort of five glioma patients, replacing the standard CEST-EPI sequence acquired in patients prior to surgery and used for biopsy target selection. Scan parameters were TE = 14.0/34.1/58.0/92.4, TR = 428 ms, matrix size = 128x104, FOV = 256x217 mm, GRAPPA = 3, bandwidth = 1628 Hz/pixel, slice thickness = 4 mm with no gap, number of slices = 25, phase encode direction = A>>P, number of runs = 2. A saturation pulse train of 3x100 ms 6 μT Gaussian pulses separated by a deadtime of 10 ms was applied prior to water-selective excitation and readout. The saturation offset frequency was swept from -3.5 to -2.5 ppm, from -0.3 to 0.3 ppm, and from 2.5 to 3.5 ppm, in units of 0.1 ppm for a total of 29 spectral measurements. An S_0 image was also acquired by keeping all parameters the same and reducing the B_1 amplitude to zero (number of averages = 4).

Although contrast was in some cases similar between the four echoes, some patients displayed more highly acidic lesions at longer echo times. An example is shown in Figure 69. At a short echo time of 14 ms, a small lesion is visible in the left hemisphere. However, at higher echo times, the original lesion shows increasingly higher contrast and additional lesions appear in the right hemisphere. This may be due to these regions having less restricted water molecules that that are more highly weighted using longer echoes.

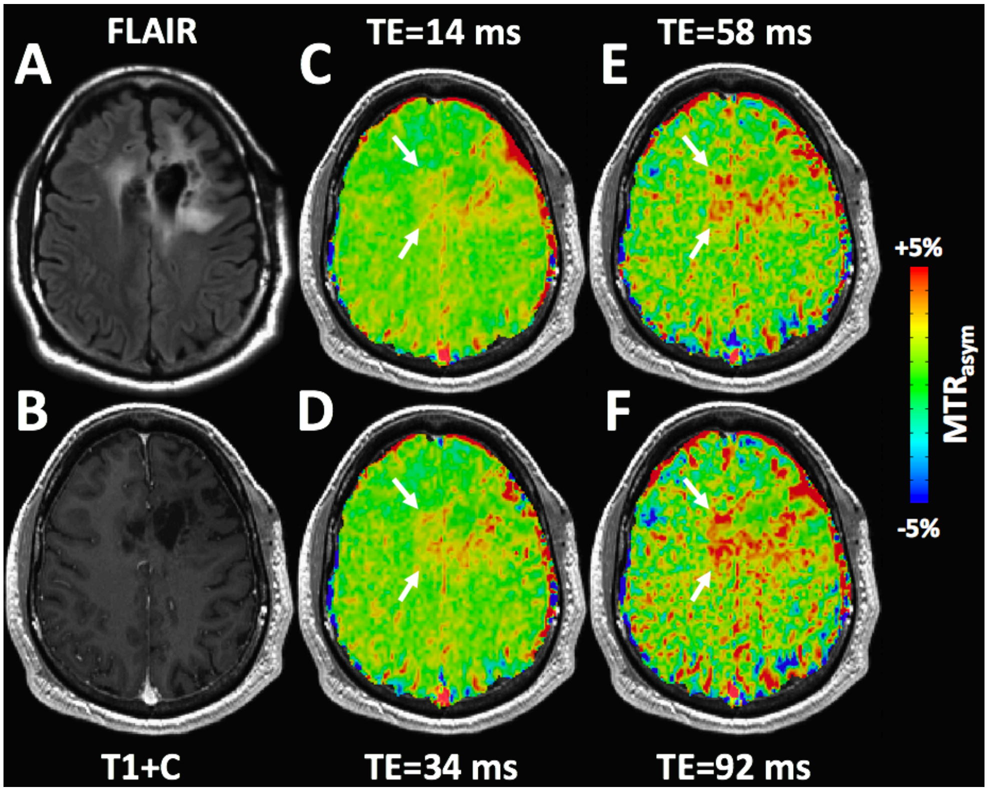

Figure 69. Comparison of MTR_{asym} calculated with four different echoes using a multi-echo CEST-EPI readout in a high-grade glioma patient. Some regions (white arrows) appear more acidic when measuring contrast using longer echoes.

To determine the effect of differing echo time on the noise characteristics within tissue, ROIs were drawn within regions of NAWM for all patients. The mean value of MTR_{asym} along with the standard deviation of MTR_{asym} was pulled from the NAWM region for each patient and each echo. We observed that while the mean value of MTR_{asym} remaining fairly constant, the noise increased with increasing echo time (Echo 1, $MTR_{asym} = 1.00\pm0.64\%$; Echo 2, $MTR_{asym} = 1.03\pm0.72\%$; Echo 3, $MTR_{asym} = 1.07\pm1.05\%$; Echo 4, $MTR_{asym} = 1.06\pm1.41\%$). This is an intuitive result as waiting longer to record the echo data will result in lower SNR.

ii. Quantitative pH Mapping

When processing pH-weighted data, the resultant values of MTR_{asym} calculated for each image voxel are a nonlinear function of the variables described in Equation 11. Variables related to the saturation pulse train, image acquisition parameters, and proton resonance frequencies are known when imaging, leaving the relaxation rates of tissue and the amine pool, as well as the amine concentration and exchange rate, unknown. The amine relaxation rates T_{1b} and T_{2b} have been shown to have a negligible effect on the resulting contrasts within a typical range of unbound metabolite values (Figure 14). Therefore, the remaining unknown variables are T_{1a}, T_{2a}, and the amine concentration and exchange rate. The exchange rate is dependent upon pH as given by Equation 17. The relaxation rates T_{1a} and T_{2a} can be measured for each voxel by a series of anatomical T_1-weighted and T_2-weighted images, respectively. While we currently have no accurate method for measuring the amine concentration on a voxel-wise basis, it can be estimated as 50 mM for the purpose of these calculations as described in Chapter II, leaving pH as the only unknown variable influencing MTR_{asym}. Therefore, using our CEST simulation in conjunction with maps of $\mathrm{MTR_{asym}}$ generated by our pH-weighted CEST-EPI sequence, we can quantitatively estimate pH in each voxel if T_{1a} and T_{2a} in that voxel are also known.

Quantitative pH maps in Human Subjects

CEST-EPI data were acquired in five clinical glioma patients using the multi-echo pH-weighted CEST sequence described previously. For T_1 measurement, a series of four spin-echo inversion-recovery EPI sequences were acquired with a TE/TR = 85/10000 ms and variable inversion times (TIs) of 50, 400, 1100, and 2500 ms. The data were fit using a nonlinear least-squares algorithm (*lsqnonlin*) in Matlab via the inversion recovery signal equation

$$M = M_0(1 - 2e^{-TI/T_1} + e^{-TR/T_1}) \tag{19}$$

to obtain a quantitative map of T_1. For T_2 measurement, the 14 ms and 92 ms echoes of the S_0 multi-echo readout were used to calculate a T_2 map. The data were fit to the exponential signal equation

$$M = M_0(1 - e^{-TR/T_1})e^{-TE/T_2} \tag{20}$$

using Matlab. T_1 maps were then resampled to the resolution of the CEST data. No resampling of T_2 maps was necessary because they were calculated from the S_0 image.

The clinical CEST-EPI simulation described in Chapter II was used to estimate pH for each image voxel. T_1 and T_2 for each voxel were input into the simulation using an initial condition of pH=7.0. The difference between the resulting value of $\mathrm{MTR_{asym}}$ and the experimentally measured value of $\mathrm{MTR_{asym}}$ was then minimized on a voxel-wise basis using the *lsqnonlin* function in Matlab to obtain quantitative pH maps. The region of abnormal FLAIR enhancement for these patients was contoured using a semi-automated thresholding method as described previously and values of MTR_{asym} as well as quantitative pH were pulled from this region for all voxels and compared to examine the relationship between the two contrasts.

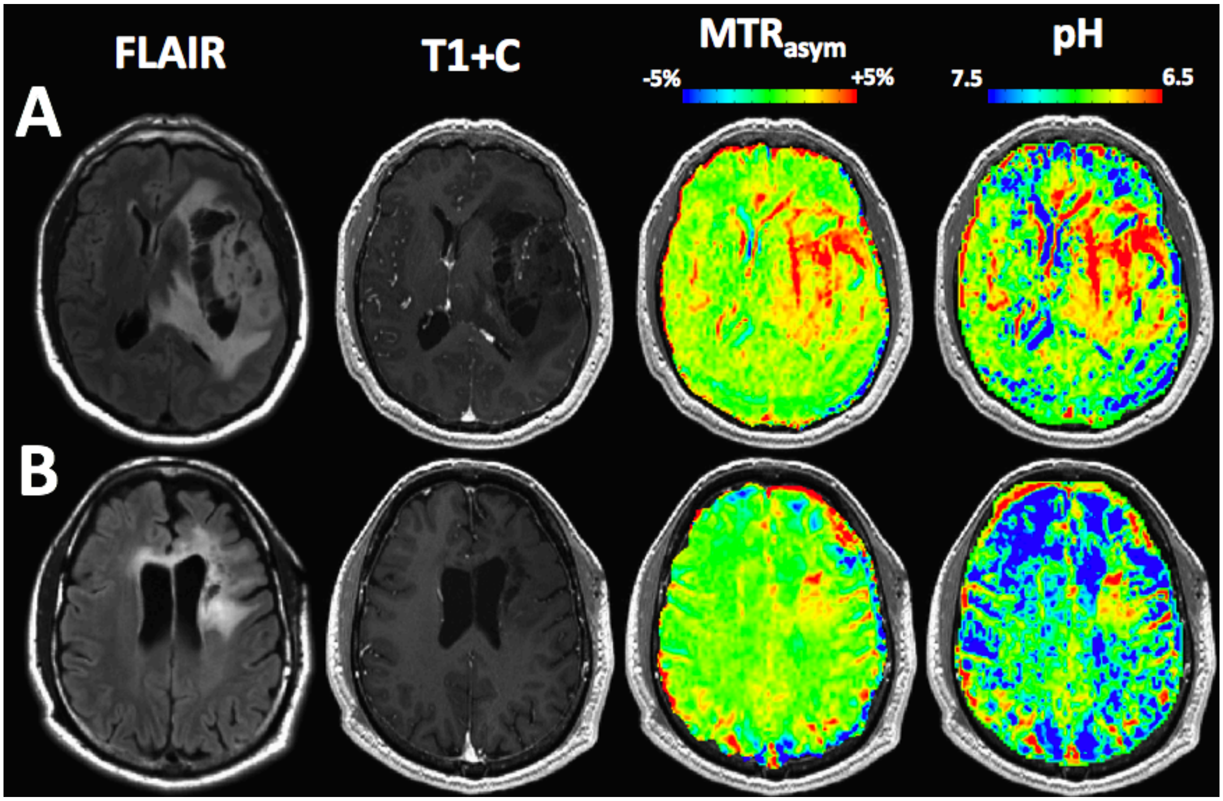

Figure 70. Quantitative pH maps in two high-grade glioma patients (A&B) and their comparison with pH-weighted images expressed by MTR_{asym}. Regions of acidity appear consistent between pH-weighted and quantitative pH images.

Two examples of quantitative pH maps are shown in Figure 70. Results showed that although healthy tissue appeared to be more differentiated from tumor tissue, the area of acidity seen did not appear significantly different between pH-weighted images and quantitative pH maps. Because these quantitative pH maps are corrected for T_1 and T_2 effects by incorporating them into the simulation, this indicates that although the CEST effect is dependent on T_1 and T_2 properties at low pH, the effects of T_1 and T_2 do not significantly alter the observed contrast or areas of acidity seen on pH-weighted images. Nonetheless, quantitative pH maps are a better way to display information about heterogeneous acidity, as units of pH are more intuitive and correction for T_1 and T_2 effects is more robust.

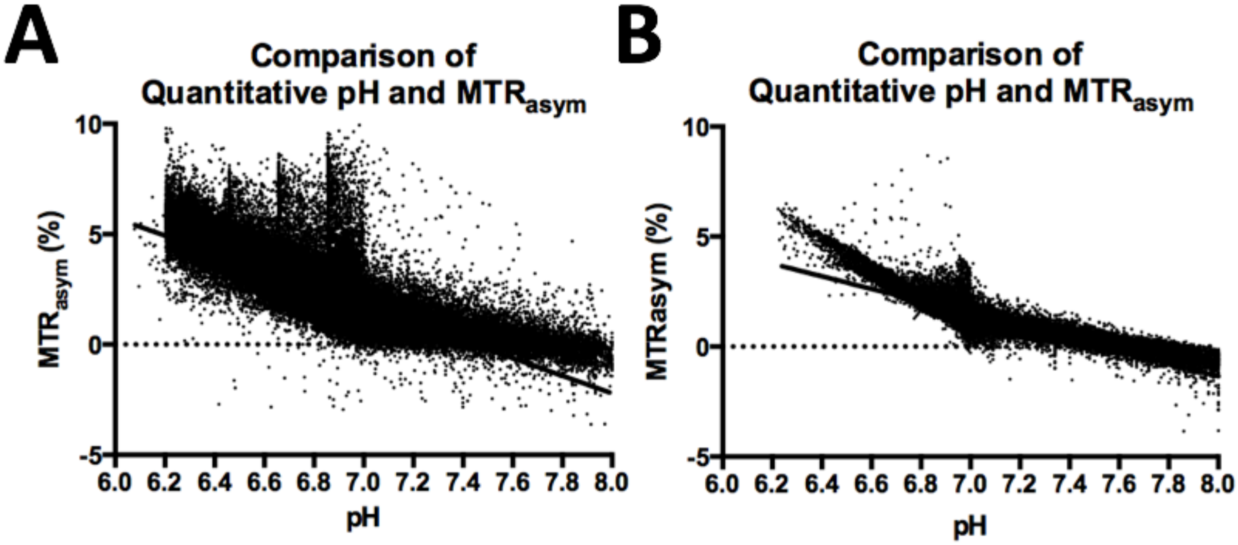

Figure 71. Comparison of MTR_{asym} on pH-weighted images and pH on quantitative pH maps for the two high-grade glioma patients (A&B) shown in Figure 70. The dotted line represents $MTR_{asym} = 0\%$. The solid line represents a linear fit to the data.

A comparison of MTR_{asym} and quantitative pH for all image voxels within the FLAIR-enhancing lesion of two high-grade glioma patients is shown in Figure 71. Linear regression showed that the slope for both comparisons was significantly different from zero ($P<0.0001$), although the data did not appear linear and rather appeared to have a more negative slope between pH values of 6.2 and 7.0 than between 7.0 and 8.0. This is reasonable to expect due to the more negative slope between MTR_{asym} and pH at pH values below 7.0 as seen in simulations. The vertical variance in MTR_{asym} at each pH value is likely due to the effects of compensating for T_1 and T_2 in our quantitative pH model, as regions of high T_1 or T_2 and high MTR_{asym} may result in the same pH value as a region of lower T_1 or T_2 and a lower MTR_{asym}.

Quantitative pH Mapping in Mice

The quantitative pH mapping technique was then applied to pH-weighted MRI data acquired in a mouse tumor model as described in Chapter III, Section iv. On a subset of three mice, in addition to collection of the MSME sequence for T_2 mapping, a series of three T1-weighted fast low-angle shot (FLASH) sequences were acquired with flip angles of 10º, 20º, and 30º. Other parameters were TE/TR = 3.8/135 ms, FOV = 2x2 cm, matrix size = 256x256, slice thickness 1 mm, slices = 11, bandwidth = 44642 Hz, total acquisition time = 1:08. The data were fit to Eqn. 19 using Matlab to generate a T_1 map. The T_1 map and T_2 map were then registered to the CEST data and downsampled to a resolution of 128x128 to improve processing time. Quantitative pH maps were calculated using the *lsqnonlin* function in Matlab as described previously. An ROI was then drawn encompassing the brain over all five slices of CEST data. Values of MTR_{asym} and pH were pulled from this ROI and compared on a voxel-wise basis.

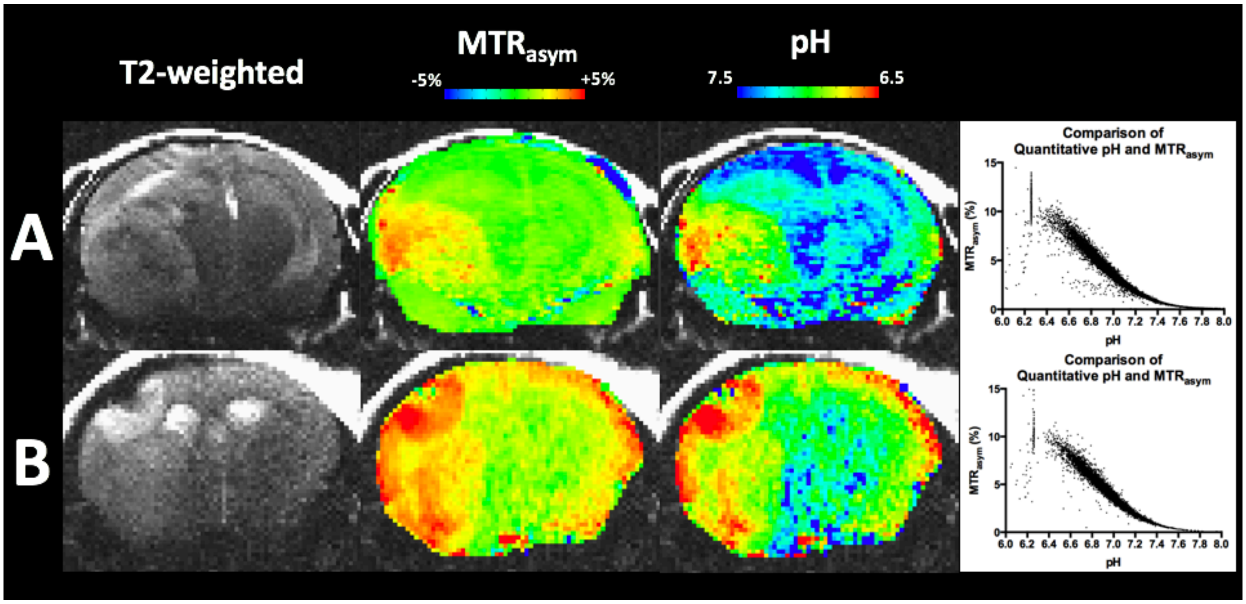

Figure 72. Quantitative pH maps in glioma-bearing mice (A&B) and their comparison with pH-weighted images expressed by MTR_{asym}. Regions of acidity appear fairly consistent between pH-weighted and quantitative pH images. Scatterplots comparing MTR_{asym} to quantitative pH on a voxel-wise basis for each mouse are shown on the right.

Quantitative pH maps for two mice are shown in Figure 72. Similar to human data, the contrasts provided by maps of MTR_{asym} and pH were fairly similar. Scatterplot data again showed a relationship between MTR_{asym} and pH that resembled the simulation data.

Some previous studies have attempted to correct for T_1 relaxation effects in CEST experiments. Zaiss et al. proposed a simple voxel-wise linear correction of T_1 when using a novel inverse z-spectra method of calculating CEST contrast in a stroke model [164]. This T_1 correction was then also applied in human glioblastoma at 7T [128]. However, to our knowledge, our technique is the first to implement a correction for T_2 during analysis of quantitative CEST data. Our technique also utilizes a nonlinear correction for T_1 and T_2 derived from the Bloch-McConnell equations rather than a simple linear correction.

One limitation of this model is that it appears to produce very few pH values below approximately 6.2 for either human or pre-clinical imaging. This is likely due to the peak that occurs at a pH of approximately 6.2 in the simulated curve of MTR_{asym} versus pH at both field strengths that is used as the basis of this algorithm. Because our quantitative pH solver uses an initial condition of pH=7.0, the algorithm does not proceed past this peak in most cases. Although tissue pH values below 6.2 are likely uncommon, pH values just below 6.2 would be expected to have similar values of MTR_{asym} as pH values just above 6.2.

CHAPTER VII

Conclusions

Tissue acidification in gliomas serves as an important biomarker for tumor proliferation and treatment response. This work describes the development of a novel application of CEST MRI that can be used for pH-weighted imaging of the brain. MRI has advantages in spatial resolution over other imaging modalities such as MRS and PET, which is important in the context of brain tumor imaging due to the heterogeneity of many tumors. A theoretical basis for pH-weighted contrast using CEST MRI targeted to amino acid amine protons was derived from the Bloch-McConnell equations, and the effects of scan parameters and tissue properties on the CEST signal were described. Our pH-weighted sequence was applied in animal models of glioma, showing that pH-weighted MRI provides unique contrast within the tumor region and can serve as a biomarker in mice undergoing dendritic cell therapy. To our knowledge, we also performed the first *in vivo* comparison of measured tissue pH with pH-weighted imaging in an animal model. Our pH-weighted sequence was then applied serially in a cohort of human glioblastoma patients undergoing standard of care radiochemotherapy. The resulting contrast served as a biomarker for progression-free survival and was able to identify regions of proliferating tissue in select patients with biopsy data. Over time, our pH-weighted sequence was upgraded from a GRE readout to an EPI readout using manual modifications to the source code of these sequences. This allows us to collect full coverage of the brain, with additional spectral points and multiple averages within a clinically feasible scan time. We have shown a correlation between acidic contrast on pH-weighted imaging and uptake of ^{18}F-FDOPA PET, an amino acid analog tracer sensitive to tumor proliferation. We have also implemented our pH-weighted sequence in a cohort of glioma patients prior to surgery and demonstrated that histological markers of tumor proliferation are elevated in regions of acidity. We have shown that acidity as measured by pH-weighted MRI decreases following bevacizumab treatment, and that acidic lesions can sometimes be indicative of tumor growth at later time points. Finally, we have described some advanced techniques related to the acquisition and processing of pH-weighted MRI. We have introduced a multi-echo technique sensitive to multiple water compartments and that can be used to calculate T_2 maps. We have also developed an algorithm for calculating quantitative pH maps corrected for T_1 and T_2 using our previously described simulation, which incorporates the Bloch-McConnell equations as well as clinical scan parameters.

Although the work presented here has advanced our knowledge of CEST MRI and pH-weighted imaging in gliomas, further work remains to be done. Many ailments of the brain are associated with tissue acidification, including stroke; research on the effectiveness of pH-weighted MRI for delineating salvageable tissue is needed in these patients. Furthermore, tumors in other organs often present acidification of the tissue as well. Although there are logistical hurdles that must be surmounted in other settings such as prostate or thoracic imaging, pH-weighted imaging may show value in these settings and should be explored. Regardless, this work has described an encompassing development of our technique by incorporating simulations, phantom testing, animal experiments, and human data to show that CEST MRI can serve as a pH-weighted biomarker in gliomas.

Appendix A

CEST Simulation Code (Matlab)

```
% function [pHcurve] = CEST_Simulation_Iterative_v5(parA,parB)  %% Activate
when solving

%% MASTER SWITCH FOR CODE %%
% 1 - Signal vs ppm, MTRasym vs ppm
% 2 - Signal vs time, MTRasym vs time
% 3 - MTRasym vs pH
%% MASTER SWITCH FOR CODE %%

% x0 = [500, 5];
% ExchRateFunction =@(x) data - CEST_Simulation_Iterative_v5( x(1),x(2) );
% x = lsqnonlin( ExchRateFunction,x0 );

M_az_spectra = zeros(101,1);
M_bz_spectra = zeros(101,1);
M_cz_spectra = zeros(101,1);
MTRasym = zeros(50,1);

timespectra = zeros(101,50);  %% #TimePoints
timeMTRasym = zeros(50,50);   %% #TimePoints
m_spectra = zeros(101,50);
m_MTRasym = zeros(50,50);

pHcurve = zeros(1,51);    %% DEACTIVATE when solving
% pHcurve = zeros(1,12);    %% ACTIVATE when solving
ppmxaxis = linspace(-5,5,101);
ppmxposaxis = linspace(0.1,5,50);

% data = [15.2231   18.64195    20.38035    22.87845    22.40435    18.17615
13.27825    9.30111 4.8995  2.573925    1.791075    1.667245]; % sinc6
data = [18.7587 22.0734 26.3334 28.0175 27.12   22.4367 18.7575 14.2706
7.90236 4.23159 1.45495 1.51561]; %gauss 6 uT
% data = [20.1494     22.6863   25.1745   25.4579   21.4094   17.7415
10.3182   6.094     3.2317    2.577   2.2421    2.6649]; %gauss 4 uT
% data = [15.0552     16.7991   18.7687   18.747    15.857      12.8547
7.4873    4.4007  2.5025  1.8358  1.875   2.2028]; %sinc 4 uT
% data = [ 6.30315  5.65791 11.0303 11.4946 2.54487 1.39609 6.00787 3.96174
1.76724 1.00656 6.89547 8.74515 0.639372    1.98446 5.14876 5.88682] ; % 7T
Fit

% pHcurve = zeros(1,16); % 7T Fit
% pHarray = [6.948  6.962   6.784   6.704   6.85    6.85    6.55    6.65
6.71    6.92    6.9 6.8 6.72101 6.67101 6.56101 6.52101];

% pHarray = linspace(5.4,7.6,12);    %% ACTIVATE when solving
pHarray = linspace(4,9,51);     %% DEACTIVATE when solving

% ExchRateArray = parA + (parB*10^10).*(10.^-(14-pHarray));    %% ACTIVATE
when solving

% ExchRateArray = 4258 + (0.0808*10^10).*(10.^-(14-pHarray));    %%
```

```
DEACTIVATE when solving
% ExchRateArray = 134.7678 + (5.1443*10^10).*(10.^-(14-pHarray));    %%
DEACTIVATE when solving

ExchRateArray = 75.8854 + (5.6414*10^10).*(10.^-(14-pHarray));    %%
DEACTIVATE when solving

% for e = 11:41  %%% 3
% for e = 1:12  %%% 3     %% ACTIVATE when solving
for e = 21  %%% 3

    exportx07 = [];

% for i = -5:0.1:5  %%% 1
for i = -3.0:6.0:3.0  %%% 2,3  %% ACTIVATE when solving
% for i = 3.0

GMR = 42.576;
FieldStrength = 3.0;
BaseFrequency = GMR * FieldStrength;  % In MHz

B1 = 6;
GaussPulseNorm = [0.037775253   0.043008072 0.048837602 0.055312138
0.062481052 0.070394379 0.079102353 0.088654867 0.099100885 0.11048778
0.122860627 0.13626144  0.150728364 0.166294837 0.182988716 0.200831402
0.219836953 0.240011216 0.261350988 0.283843216 0.307464274 0.3321793
0.357941651 0.38469246  0.412360329 0.440861168 0.470098193 0.499962099
0.53033141  0.561073017 0.592042906 0.623087081 0.654042662 0.684739173
0.714999991 0.744643949 0.773487072 0.801344424 0.828032047 0.853368951
0.87717914  0.899293634 0.919552457 0.937806557 0.953919631 0.967769819
0.979251234 0.988275312 0.994771952 0.998690418 1   0.998690418 0.994771952
0.988275312 0.979251234 0.967769819 0.953919631 0.937806557 0.919552457
0.899293634 0.87717914  0.853368951 0.828032047 0.801344424 0.773487072
0.744643949 0.714999991 0.684739173 0.654042662 0.623087081 0.592042906
0.561073017 0.53033141  0.499962099 0.470098193 0.440861168 0.412360329
0.38469246  0.357941651 0.3321793   0.307464274 0.283843216 0.261350988
0.240011216 0.219836953 0.200831402 0.182988716 0.166294837 0.150728364
0.13626144  0.122860627 0.11048778  0.099100885 0.088654867 0.079102353
0.070394379 0.062481052 0.055312138 0.048837602 0.043008072 0.037775253];
SincPulseNorm = [   0   -0.0058   -0.0183   -0.0305   -0.0421   -0.0532   -
0.0639   -0.0742 -0.0839   -0.0932   -0.1018   -0.1095   -0.1162   -0.1215
-0.1251   -0.1268 -0.1260   -0.1226   -0.1162   -0.1064   -0.0932   -0.0763
-0.0556   -0.0311 -0.0027    0.0296    0.0656    0.1051    0.1480    0.1940
0.2427    0.2937 0.3466    0.4008    0.4557    0.5108    0.5653    0.6187
0.6703    0.7195 0.7658    0.8086    0.8477    0.8826    0.9133    0.9394
0.9608    0.9777   0.9898    0.9973    1.0000    0.9982    0.9916    0.9804
0.9645    0.9439 0.9187    0.8890    0.8549    0.8166    0.7744    0.7288
0.6801    0.6290  0.5759    0.5215    0.4665    0.4115    0.3571    0.3039
0.2525    0.2033  0.1568    0.1132    0.0730    0.0363    0.0034   -0.0258
-0.0511   -0.0726  -0.0902   -0.1041   -0.1145   -0.1216   -0.1256   -0.1268
-0.1256   -0.1223  -0.1173   -0.1109   -0.1033   -0.0949   -0.0858   -0.0761
-0.0660   -0.0554  -0.0443   -0.0328   -0.0208   -0.0083         0];

GaussPulse = GaussPulseNorm .* (B1*2*pi*GMR);
SincPulse = SincPulseNorm .* (B1*2*pi*GMR);
RectPulse = zeros(1,101) + (B1*2*pi*GMR);
```

```
PulseBins = 101;

w_a = 0;
w_b = BaseFrequency * 3.0;
w_c = BaseFrequency * 3.5;
w = BaseFrequency * i;

M_a0 = 1;
M_b0 = 0.0009009;
M_c0 = 0.000;

C_b = ExchRateArray(e);  %%% 3   %%% 1,2  % index=pH, 21=6, 26=6.5, 31=7
C_c = 10;  % Dummy value when M_c0 = 0 (can't be zero or equations will fail)
C_ab = (M_b0 / M_a0) * C_b;
C_ac = (M_c0 / M_a0) * C_c;
C_a = C_ab + C_ac;

T_1a = 1.22;  %% 3.374 from Chen et al  %% 1.22 for tissue   %% 1.36 for
tumor (Chistopher Larsson 2015) %% 1.939 7T
T_1b = 0.2;   %% using 0.2
T_1c = 0.1;
T_2a = 0.107;  %% 2.5 from Araujo et al % 0.107 for tissue (Ellingson
paper)  %% 0.170 for NET (Ellingson paper) % 0.055 7T
T_2b = 0.1;    %% using 0.1
T_2c = 0.1;

k_1a = (1 / T_1a) + C_a;
k_2a = (1 / T_2a) + C_a;
k_1b = (1 / T_1b) + C_b;
k_2b = (1 / T_2b) + C_b;
k_1c = (1 / T_1c) + C_c;
k_2c = (1 / T_2c) + C_c;

da = (w - w_a) * 2*pi;
db = (w - w_b) * 2*pi;
dc = (w - w_c) * 2*pi;


    % Sherry 2005
    % DY/dt = A*Y + b

 %  Y = [ M_ax(t) M_bx(t) M_cx(t) M_ay(t) M_by(t) M_cy(t) M_az(t) M_bz(t)
M_cz(t) ];

     I = eye(9);  %identity matrix

     b = [0; 0; 0; 0; 0; 0; M_a0/T_1a; M_b0/T_1b; M_c0/T_1c];

     for t = 1:1        % added for TIME LOOP

     t;
     time = 1.0*t;  %seconds
     timestep = time / PulseBins;

     x0 = [ 0; 0; 0; 0; 0; 0; M_a0; M_b0; M_c0] ;
```

```
     Y = zeros(9,1);    %allocate memory for Y matrix

     Slices = 25;

     ReadoutLength = 60; %% in ms

     Deadtime = 10; %% in ms

     % ADDED FOR M->0 per slice readout
     %  x0(7) = M_a0 - ( M_a0 - 0 ) * exp( -Slices*TR / T_1a );
     %  x0(7) = 0;
     % ADDED FOR M->0 per slice readout


     for m = 1:25  %% m is multiple RF influence from short TR loop (#slices)

     x0(1) = 0;
     x0(2) = 0;
     x0(3) = 0;
     x0(4) = 0;
     x0(5) = 0;
     x0(6) = 0;

         for ReadoutLoop = 1:ReadoutLength
        % for ReadoutLoop = 1:1

     % x0(7) = M_a0 - ( M_a0 - x0(7) ) * exp( -Readout / T_1a );
     % x0(8) = M_b0 - ( M_b0 - x0(8) ) * exp( -Readout / T_1b );
     % x0(9) = M_c0 - ( M_c0 - x0(9) ) * exp( -Readout / T_1c );
     x0(7) = M_a0 - ( M_a0 - x0(7) ) * exp( -00.001 / T_1a );
     x0(8) = M_b0 - ( M_b0 - x0(8) ) * exp( -00.001 / T_1b );
     x0(9) = M_c0 - ( M_c0 - x0(9) ) * exp( -00.001 / T_1c );

             exportx07 = [exportx07 x0(7)];

         end  %% ReadoutLoop End

         NumberOfPulses = 1;

     for N_RF = 1:NumberOfPulses  %% NumberOfPulses is number of RF pulses

         N_RF;

     longGaussPulse =
interp1(linspace(1,101,101),GaussPulse,linspace(1,101,PulseBins));

     longSincPulse =
interp1(linspace(1,101,101),SincPulse,linspace(1,101,PulseBins));

     longRectPulse =
interp1(linspace(1,101,101),RectPulse,linspace(1,101,PulseBins));

     for z = 1:PulseBins  %% z is Gaussian Pulse shape loop
```

```
       w_1 = longGaussPulse(z);  %% Input variable B1 amplitude
       % w_1 = longSincPulse(z);  a
       % w_1 = longRectPulse(z);

   A = [  -k_2a      C_b        C_c        -da          0          0
0        0       0 ;
           C_ab     -k_2b          0          0        -db          0
0        0       0 ;
           C_ac          0      -k_2c          0          0        -dc
0        0       0 ;

             da          0          0      -k_2a        C_b        C_c      -
w_1        0       0 ;
              0         db          0       C_ab      -k_2b          0
0     -w_1       0 ;
              0          0         dc       C_ac          0      -k_2c
0        0    -w_1 ;

              0          0          0        w_1          0          0     -
k_1a      C_b     C_c ;
              0          0          0          0        w_1          0
C_ab    -k_1b       0 ;
              0          0          0          0          0        w_1
C_ac        0   -k_1c   ];


            Ainvb = A\b;
            y0 = x0;
            Y(:,1) = expm(A*timestep)*(y0+Ainvb)-Ainvb;

            % compared to Jin code: M0 = b, M = A %
            % so A\b = M\M0 ;
            % and y0 = x0 = Mi ;
            % so Ainvb = -Meq ;

            x0 = [ double(Y(1,1)); double(Y(2,1)); double(Y(3,1));
double(Y(4,1)); double(Y(5,1)); double(Y(6,1)); double(Y(7,1));
double(Y(8,1)); double(Y(9,1)) ];

            exportx07 = [exportx07 x0(7)];

     end  %% from z loop

       %   timespectra(int16(i*10+51),NumRF) = double(Y(7,1));   % use for RF
LOOP

           timespectra(int16(i*10+51),t) = double(Y(7,1));     % use for TIME
LOOP

           if N_RF ~= NumberOfPulses

           for DeadtimeLoop = 1:Deadtime

                     x0(7) = M_a0 - ( M_a0 - x0(7) ) * exp( -0.001 / T_1a );
                     x0(8) = M_b0 - ( M_b0 - x0(8) ) * exp( -0.001 / T_1b );
```

```
                    x0(9) = M_c0 - ( M_c0 - x0(9) ) * exp( -0.001 / T_1c );

                    exportx07 = [exportx07 x0(7)];

          end %% DeadtimeLoop End

          end  %% N_RF~=Max loop End

     end %% from RFnum loop

     m_spectra(int16(i*10+51),m) = double(Y(7,1));

     end  %% from m loop, #### MAGNETIZATION READ OUT HERE ####

           M_az_spectra(int16(i*10+51),1) = double(Y(7,1));

     end   %% from t loop

end

for k = 0.1:0.1:5  %%% 2,3

   % MTRasym(k,:) = ( M_az_spectra(51-k,:) - M_az_spectra(51+k,:) );
     MTRasym(int16(k*10),1) = ( M_az_spectra(int16(51-k*10),1) -
M_az_spectra(int16(51+k*10),1) ) * 100;
     timeMTRasym(int16(k*10),:) = ( timespectra(int16(51-k*10),:) -
timespectra(int16(51+k*10),:) ) * 100;
     m_MTRasym(int16(k*10),:) = ( m_spectra(int16(51-k*10),:) -
m_spectra(int16(51+k*10),:) ) * 100;
end


  pHcurve(1,e) = MTRasym(30,1) ;  %%% 3

      e  %%% 3
      % plot(ppmxaxis,M_az_spectra(:,1))
      pause(0.1)

  end  %%% 3

%% PLOTS
%% 1 - plot(ppmxaxis,M_az_spectra(:,1))   or  plot(ppmxposaxis,MTRasym(:,1))
%% 2 - plot(timespectra(21,:))  or  plot(timespectra(81,:))  or
plot(timeMTRasym(30,:))
%% 3 - plot(pHarray,pHcurve)  or  plot(pHarray,pHcurveMaz)  or
plot(pHarray,pHcurveMazNeg)

%% semilogx(ExchRateArray,pHcurve)
%% plot(m_spectra(21,:))  or  plot(m_spectra(81,:))  or
plot(m_MTRasym(30,:))
```

Appendix B

pH Solver Code (Matlab)

```
[err, MTRasymdata, Info, ErrMessage] =
BrikLoad('Echo1and2_MTRasym+orig.BRIK');
[err, T1map, Info, ErrMessage] = BrikLoad('T1map+orig.BRIK');
[err, T2map, Info, ErrMessage] = BrikLoad('T2map+orig.BRIK');
[err, MaskForMatlab, Info, ErrMessage] = BrikLoad('MaskForMatlab+orig.BRIK');



XX = size(MTRasymdata,1);
YY = size(MTRasymdata,2);
ZZ = size(MTRasymdata,3);

pHmap = zeros(XX,YY,ZZ);
vcount = 0;

for i = 1:XX
    for j = 1:YY
        for k = 1:ZZ

            if MTRasymdata(i,j,k) ~=0;
                if T1map(i,j,k) ~=0;
                    if T2map(i,j,k) ~=0;
                        if MaskForMatlab(i,j,k) ~=0;

            try

            x0 = [7.0];
            SolvingFunction =@(x) MTRasymdata(i,j,k) -
CEST_pH_Solver2( T1map(i,j,k) , T2map(i,j,k), x(1) );
            x = lsqnonlin( SolvingFunction, x0, 6.0, 8.0 );

            pHmap(i,j,k) = x;

            catch
                pHmap(i,j,k) = 0;
            end

            x
            vcount = vcount+1

                        end
                    end
                end
            end

        end
    end
end

Opt.Prefix = 'pHMap'
WriteBrik(pHmap, Info, Opt);
```

REFERENCES

1. Dolecek, T.A., et al., *CBTRUS statistical report: primary brain and central nervous system tumors diagnosed in the United States in 2005-2009.* Neuro Oncol, 2012. **14 Suppl 5**: p. v1-49.

2. Grier, J.T. and T. Batchelor, *Low-grade gliomas in adults.* Oncologist, 2006. **11**(6): p. 681-93.

3. Omuro, A. and L.M. DeAngelis, *Glioblastoma and other malignant gliomas: a clinical review.* JAMA, 2013. **310**(17): p. 1842-50.

4. Stupp, R., et al., *Radiotherapy plus concomitant and adjuvant temozolomide for glioblastoma.* N Engl J Med, 2005. **352**(10): p. 987-96.

5. Venur, V.A., D.M. Peereboom, and M.S. Ahluwalia, *Current medical treatment of glioblastoma.* Cancer Treat Res, 2015. **163**: p. 103-15.

6. Ellingson, B.M., et al., *Probabilistic radiographic atlas of glioblastoma phenotypes.* AJNR Am J Neuroradiol, 2013. **34**(3): p. 533-40.

7. Gerweck, L.E. and K. Seetharaman, *Cellular pH gradient in tumor versus normal tissue: potential exploitation for the treatment of cancer.* Cancer Res, 1996. **56**(6): p. 1194-8.

8. Griffiths, J.R., *Are cancer cells acidic?* Br J Cancer, 1991. **64**(3): p. 425-7.

9. Helmlinger, G., et al., *Interstitial pH and pO2 gradients in solid tumors in vivo: high-resolution measurements reveal a lack of correlation.* Nat Med, 1997. **3**(2): p. 177-82.

10. Gallagher, F.A., et al., *Magnetic resonance imaging of pH in vivo using hyperpolarized 13C-labelled bicarbonate.* Nature, 2008. **453**(7197): p. 940-3.

11. Estrella, V., et al., *Acidity generated by the tumor microenvironment drives local invasion.* Cancer Res, 2013. **73**(5): p. 1524-35.

12. Raghunand, N., R.A. Gatenby, and R.J. Gillies, *Microenvironmental and cellular consequences of altered blood flow in tumours.* Br J Radiol, 2003. **76 Spec No 1**: p. S11-22.

13. Helmlinger, G., et al., *Acid production in glycolysis-impaired tumors provides new insights into tumor metabolism.* Clin Cancer Res, 2002. **8**(4): p. 1284-91.

14. Gatenby, R.A. and R.J. Gillies, *Why do cancers have high aerobic glycolysis?* Nat Rev Cancer, 2004. **4**(11): p. 891-9.

15. Harris, R.J., et al., *pH-weighted molecular imaging of gliomas using amine chemical exchange saturation transfer MRI.* Neuro Oncol, 2015. **17**(11): p. 1514-24.

16. Lardner, A., *The effects of extracellular pH on immune function.* J Leukoc Biol, 2001. **69**(4): p. 522-30.

17. Morita, T., et al., *Clastogenicity of low pH to various cultured mammalian cells.* Mutat Res, 1992. **268**(2): p. 297-305.

18. Martinez-Zaguilan, R., et al., *Acidic pH enhances the invasive behavior of human melanoma cells.* Clin Exp Metastasis, 1996. **14**(2): p. 176-86.

19. Shi, Q., et al., *Regulation of vascular endothelial growth factor expression by acidosis in human cancer cells.* Oncogene, 2001. **20**(28): p. 3751-6.

20. Griffiths, L., et al., *The influence of oxygen tension and pH on the expression of platelet-derived endothelial cell growth factor/thymidine phosphorylase in human breast tumor cells grown in vitro and in vivo.* Cancer Res, 1997. **57**(4): p. 570-2.

21. Freeman, M.L. and E. Sierra, *An acidic extracellular environment reduces the fixation of radiation damage.* Radiat Res, 1984. **97**(1): p. 154-61.

22. Reichert, M., et al., *Modulation of growth and radiochemosensitivity of human malignant glioma cells by acidosis.* Cancer, 2002. **95**(5): p. 1113-9.

23. Lagemaat, M.W., et al., *(31) P MR spectroscopic imaging of the human prostate at 7 T: T1 relaxation times, Nuclear Overhauser Effect, and spectral characterization.* Magn Reson Med, 2015. **73**(3): p. 909-20.

24. Rata, M., et al., *Comparison of three reference methods for the measurement of intracellular pH using 31P MRS in healthy volunteers and patients with lymphoma.* NMR Biomed, 2014. **27**(2): p. 158-62.

25. Gerweck, L.E., *Tumor pH: implications for treatment and novel drug design.* Semin Radiat Oncol, 1998. **8**(3): p. 176-82.

26. Salamanca-Cardona, L. and K.R. Keshari, *(13)C-labeled biochemical probes for the study of cancer metabolism with dynamic nuclear polarization-enhanced magnetic resonance imaging.* Cancer Metab, 2015. **3**: p. 9.

27. Lokling, K.E., et al., *pH-sensitive paramagnetic liposomes as MRI contrast agents: in vitro feasibility studies.* Magn Reson Imaging, 2001. **19**(5): p. 731-8.

28. Mikawa, M., et al., *Gd(3+)-loaded polyion complex for pH depiction with magnetic resonance imaging.* J Biomed Mater Res, 2000. **49**(3): p. 390-5.

29. Aime, S.B., A; Botta, M; Howard, J; Kataky, R; Lowe, M; Moloney, J; Parker, D; de Sousa, A, *Dependence of the relaxivity and luminescence of gadolinium and europium amino-acid complexes on hydrocarbonate and pH.* Chemical Communications, 1999(11): p. 1047-1048.

30. Deoni, S.C., *Quantitative relaxometry of the brain.* Top Magn Reson Imaging, 2010. **21**(2): p. 101-13.

31. Al-Khalili, J., *The birth of the electric machines: a commentary on Faraday (1832) 'Experimental researches in electricity'.* Philos Trans A Math Phys Eng Sci, 2015. **373**(2039).

32. Mezrich, R., *A perspective on K-space.* Radiology, 1995. **195**(2): p. 297-315.

33. Woessner, D.E., et al., *Numerical solution of the Bloch equations provides insights into the optimum design of PARACEST agents for MRI.* Magn Reson Med, 2005. **53**(4): p. 790-9.

34. Zaiss, M. and P. Bachert, *Chemical exchange saturation transfer (CEST) and MR Z-spectroscopy in vivo: a review of theoretical approaches and methods.* Phys Med Biol, 2013. **58**(22): p. R221-69.

35. Jones, C.K., et al., *Nuclear Overhauser enhancement (NOE) imaging in the human brain at 7T.* Neuroimage, 2013. **77**: p. 114-24.

36. Kogan, F., et al., *Investigation of chemical exchange at intermediate exchange rates using a combination of chemical exchange saturation transfer (CEST) and spin-locking methods (CESTrho).* Magn Reson Med, 2012. **68**(1): p. 107-19.

37. Haris, M., et al., *MICEST: a potential tool for non-invasive detection of molecular changes in Alzheimer's disease.* J Neurosci Methods, 2013. **212**(1): p. 87-93.

38. Chan, K.W., et al., *Natural D-glucose as a biodegradable MRI contrast agent for detecting cancer.* Magn Reson Med, 2012. **68**(6): p. 1764-73.

39. Walker-Samuel, S., et al., *In vivo imaging of glucose uptake and metabolism in tumors.* Nat Med, 2013. **19**(8): p. 1067-72.

40. Ling, W., et al., *Assessment of glycosaminoglycan concentration in vivo by chemical exchange-dependent saturation transfer (gagCEST).* Proc Natl Acad Sci U S A, 2008. **105**(7): p. 2266-70.

41. Dula, A.N., et al., *Optimization of 7-T chemical exchange saturation transfer parameters for validation of glycosaminoglycan and amide proton transfer of fibroglandular breast tissue.* Radiology, 2015. **275**(1): p. 255-61.

42. Wu, R., et al., *Quantitative chemical exchange saturation transfer (qCEST) MRI - omega plot analysis of RF-spillover-corrected inverse CEST ratio asymmetry for simultaneous determination of labile proton ratio and exchange rate.* NMR Biomed, 2015. **28**(3): p. 376-83.

43. Saito, S., et al., *Factors affecting the chemical exchange saturation transfer of Creatine as assessed by 11.7 T MRI.* Radiol Phys Technol, 2015. **8**(1): p. 146-52.

44. Cai, K., et al., *CEST signal at 2ppm (CEST@2ppm) from Z-spectral fitting correlates with creatine distribution in brain tumor.* NMR Biomed, 2015. **28**(1): p. 1-8.

45. Kogan, F., et al., *In vivo chemical exchange saturation transfer imaging of creatine (CrCEST) in skeletal muscle at 3T.* J Magn Reson Imaging, 2014. **40**(3): p. 596-602.

46. Sun, P.Z., et al., *Investigation of optimizing and translating pH-sensitive pulsed-chemical exchange saturation transfer (CEST) imaging to a 3T clinical scanner.* Magn Reson Med, 2008. **60**(4): p. 834-41.

47. Chen, L.Q., et al., *Evaluations of extracellular pH within in vivo tumors using acidoCEST MRI.* Magn Reson Med, 2014. **72**(5): p. 1408-17.

48. Sun, P.Z., et al., *Quantification of iopamidol multi-site chemical exchange properties for ratiometric chemical exchange saturation transfer (CEST) imaging of pH.* Phys Med Biol, 2014. **59**(16): p. 4493-504.

49. Moon, B.F., et al., *A comparison of iopromide and iopamidol, two acidoCEST MRI contrast media that measure tumor extracellular pH.* Contrast Media Mol Imaging, 2015. **10**(6): p. 446-55.

50. Longo, D.L., et al., *A general MRI-CEST ratiometric approach for pH imaging: demonstration of in vivo pH mapping with iobitridol.* J Am Chem Soc, 2014. **136**(41): p. 14333-6.

51. Ali, M.M., et al., *A nano-sized PARACEST-fluorescence imaging contrast agent facilitates and validates in vivo CEST MRI detection of glioma.* Nanomedicine (Lond), 2012. **7**(12): p. 1827-37.

52. Li, A.X., et al., *In vivo detection of MRI-PARACEST agents in mouse brain tumors at 9.4 T.* Magn Reson Med, 2011. **66**(1): p. 67-72.

53. Zhang, S., et al., *PARACEST agents: modulating MRI contrast via water proton exchange.* Acc Chem Res, 2003. **36**(10): p. 783-90.

54. Wu, Y., et al., *pH imaging of mouse kidneys in vivo using a frequency-dependent paraCEST agent.* Magn Reson Med, 2015.

55. Sheth, V.R., et al., *Measuring in vivo tumor pHe with CEST-FISP MRI.* Magn Reson Med, 2012. **67**(3): p. 760-8.

56. Liu, G., et al., *Imaging in vivo extracellular pH with a single paramagnetic chemical exchange saturation transfer magnetic resonance imaging contrast agent.* Mol Imaging, 2012. **11**(1): p. 47-57.

57. Zhou, J., et al., *Amide proton transfer (APT) contrast for imaging of brain tumors.* Magn Reson Med, 2003. **50**(6): p. 1120-6.

58. Togao, O., et al., *Amide proton transfer imaging of adult diffuse gliomas: correlation with histopathological grades.* Neuro Oncol, 2014. **16**(3): p. 441-8.

59. Heo, H.Y., et al., *Quantitative assessment of amide proton transfer (APT) and nuclear overhauser enhancement (NOE) imaging with extrapolated semi-solid magnetization transfer reference (EMR) signals: Application to a rat glioma model at 4.7 tesla.* Magn Reson Med, 2015.

60. Zhou, J., et al., *Three-dimensional amide proton transfer MR imaging of gliomas: Initial experience and comparison with gadolinium enhancement.* J Magn Reson Imaging, 2013. **38**(5): p. 1119-28.

61. Sun, P.Z., et al., *Simplified quantitative description of amide proton transfer (APT) imaging during acute ischemia.* Magn Reson Med, 2007. **57**(2): p. 405-10.

62. Tee, Y.K., et al., *Comparing different analysis methods for quantifying the MRI amide proton transfer (APT) effect in hyperacute stroke patients.* NMR Biomed, 2014. **27**(9): p. 1019-29.

63. Klomp, D.W., et al., *Amide proton transfer imaging of the human breast at 7T: development and reproducibility.* NMR Biomed, 2013. **26**(10): p. 1271-7.

64. Dula, A.N., et al., *Amide proton transfer imaging of the breast at 3 T: establishing reproducibility and possible feasibility assessing chemotherapy response.* Magn Reson Med, 2013. **70**(1): p. 216-24.

65. Wang, R., et al., *Amide proton transfer magnetic resonance imaging of Alzheimer's disease at 3.0 Tesla: a preliminary study.* Chin Med J (Engl), 2015. **128**(5): p. 615-9.

66. Yuan, J., et al., *Amide proton transfer-weighted imaging of the head and neck at 3 T: a feasibility study on healthy human subjects and patients with head and neck cancer.* NMR Biomed, 2014. **27**(10): p. 1239-47.

67. Tietze, A., et al., *Assessment of ischemic penumbra in patients with hyperacute stroke using amide proton transfer (APT) chemical exchange saturation transfer (CEST) MRI.* NMR Biomed, 2014. **27**(2): p. 163-74.

68. Zhou, J., et al., *Practical data acquisition method for human brain tumor amide proton transfer (APT) imaging.* Magn Reson Med, 2008. **60**(4): p. 842-9.

69. Vogeli, B., *The nuclear Overhauser effect from a quantitative perspective.* Prog Nucl Magn Reson Spectrosc, 2014. **78**: p. 1-46.

70. Zhou, J., et al., *APT-weighted and NOE-weighted image contrasts in glioma with different RF saturation powers based on magnetization transfer ratio asymmetry analyses.* Magn Reson Med, 2013. **70**(2): p. 320-7.

71. Paech, D., et al., *Nuclear overhauser enhancement mediated chemical exchange saturation transfer imaging at 7 Tesla in glioblastoma patients.* PLoS One, 2014. **9**(8): p. e104181.

72. Goerke, S., et al., *Signature of protein unfolding in chemical exchange saturation transfer imaging.* NMR Biomed, 2015. **28**(7): p. 906-13.

73. Li, H., et al., *Imaging of amide proton transfer and nuclear Overhauser enhancement in ischemic stroke with corrections for competing effects.* NMR Biomed, 2015. **28**(2): p. 200-9.

74. Jin, T. and S.G. Kim, *Advantages of chemical exchange-sensitive spin-lock (CESL) over chemical exchange saturation transfer (CEST) for hydroxyl- and amine-water proton exchange studies.* NMR Biomed, 2014. **27**(11): p. 1313-24.

75. Kogan, F., et al., *Imaging of glutamate in the spinal cord using GluCEST.* Neuroimage, 2013. **77**: p. 262-7.

76. Scheidegger, R., E.T. Wong, and D.C. Alsop, *Contributors to contrast between glioma and brain tissue in chemical exchange saturation transfer sensitive imaging at 3 Tesla.* Neuroimage, 2014. **99**: p. 256-68.

77. Olsson, M.B., R. Wirestam, and B.R. Persson, *A computer simulation program for MR imaging: application to RF and static magnetic field imperfections.* Magn Reson Med, 1995. **34**(4): p. 612-7.

78. Gullberg, G.T., et al., *An MRI perfusion model incorporating nonequilibrium exchange between vascular and extravascular compartments.* Magn Reson Imaging, 1991. **9**(1): p. 39-52.

79. Graham, S.J. and R.M. Henkelman, *Understanding pulsed magnetization transfer.* J Magn Reson Imaging, 1997. **7**(5): p. 903-12.

80. Jin, T., et al., *Magnetic resonance imaging of the Amine-Proton EXchange (APEX) dependent contrast.* Neuroimage, 2012. **59**(2): p. 1218-27.

81. Sun, P.Z., *Simplified and scalable numerical solution for describing multi-pool chemical exchange saturation transfer (CEST) MRI contrast.* J Magn Reson, 2010. **205**(2): p. 235-41.

82. Sun, P.Z., et al., *Evaluation of the dependence of CEST-EPI measurement on repetition time, RF irradiation duty cycle and imaging flip angle for enhanced pH sensitivity.* Phys Med Biol, 2013. **58**(17): p. N229-40.

83. Zaiss, M. and P. Bachert, *Exchange-dependent relaxation in the rotating frame for slow and intermediate exchange -- modeling off-resonant spin-lock and chemical exchange saturation transfer.* NMR Biomed, 2013. **26**(5): p. 507-18.

84. Zaiss, M., et al., *A combined analytical solution for chemical exchange saturation transfer and semi-solid magnetization transfer.* NMR Biomed, 2015. **28**(2): p. 217-30.

85. Liepinsh, E. and G. Otting, *Proton exchange rates from amino acid side chains--implications for image contrast.* Magn Reson Med, 1996. **35**(1): p. 30-42.

86. Chen, F.e.a., *Positive and Negative Lattice Shielding Effects CO-existing in Gd (III) Ion Doped Bifunctional Upconversion Nanoprobes.* Advanced Functional Materials, 2011. **21**(22): p. 4285-4294.

87. Araujo, E.C., Y. Fromes, and P.G. Carlier, *New insights on human skeletal muscle tissue compartments revealed by in vivo t2 NMR relaxometry.* Biophys J, 2014. **106**(10): p. 2267-74.

88. Choi, C., et al., *T2 measurement and quantification of glutamate in human brain in vivo.* Magn Reson Med, 2006. **56**(5): p. 971-7.

89. Traber, F., et al., *1H metabolite relaxation times at 3.0 tesla: Measurements of T1 and T2 values in normal brain and determination of regional differences in transverse relaxation.* J Magn Reson Imaging, 2004. **19**(5): p. 537-45.

90. Li, Y., et al., *Comparison of T(1) and T(2) metabolite relaxation times in glioma and normal brain at 3T.* J Magn Reson Imaging, 2008. **28**(2): p. 342-50.

91. Perry, T.L., et al., *Free amino acids and related compounds in biopsies of human brain.* J Neurochem, 1971. **18**(3): p. 521-8.

92. Wright, P.J., et al., *Water proton T1 measurements in brain tissue at 7, 3, and 1.5 T using IR-EPI, IR-TSE, and MPRAGE: results and optimization.* MAGMA, 2008. **21**(1-2): p. 121-30.

93. Ellingson, B.M., et al., *Quantification of Nonenhancing Tumor Burden in Gliomas Using Effective T2 Maps Derived from Dual-Echo Turbo Spin-Echo MRI.* Clin Cancer Res, 2015. **21**(19): p. 4373-83.

94. Larsson, C., et al., *T1 in high-grade glioma and the influence of different measurement strategies on parameter estimations in DCE-MRI.* J Magn Reson Imaging, 2015. **42**(1): p. 97-104.

95. Schmitt, B., et al., *Optimization of pulse train presaturation for CEST imaging in clinical scanners.* Magn Reson Med, 2011. **65**(6): p. 1620-9.

96. Zong, X., et al., *Sensitivity and source of amine-proton exchange and amide-proton transfer magnetic resonance imaging in cerebral ischemia.* Magn Reson Med, 2014. **71**(1): p. 118-32.

97. Xiao, G., P.Z. Sun, and R. Wu, *Fast simulation and optimization of pulse-train chemical exchange saturation transfer (CEST) imaging.* Phys Med Biol, 2015. **60**(12): p. 4719-30.

98. Ashwal, S., et al., *Proton MR spectroscopy detected glutamate/glutamine is increased in children with traumatic brain injury.* J Neurotrauma, 2004. **21**(11): p. 1539-52.

99. van Wageningen, H., et al., *A 1H-MR spectroscopy study of changes in glutamate and glutamine (Glx) concentrations in frontal spectra after administration of memantine.* Cereb Cortex, 2010. **20**(4): p. 798-803.

100. Bustillo, J.R., et al., *Increased glutamine in patients undergoing long-term treatment for schizophrenia: a proton magnetic resonance spectroscopy study at 3 T.* JAMA Psychiatry, 2014. **71**(3): p. 265-72.

101. Liubinas, S.V., et al., *Glutamate quantification in patients with supratentorial gliomas using chemical shift imaging.* NMR Biomed, 2014. **27**(5): p. 570-7.

102. Elster, A.D., *Gradient-echo MR imaging: techniques and acronyms.* Radiology, 1993. **186**(1): p. 1-8.

103. Antonios, J.P., R.G. Everson, and L.M. Liau, *Dendritic cell immunotherapy for brain tumors.* J Neurooncol, 2015. **123**(3): p. 425-32.

104. Suzuki, S., et al., *Current status of immunotherapy.* Jpn J Clin Oncol, 2016.

105. Antonios, J.P., Journal of Clinical Investigation, 2016. **[Manuscript under review]**.

106. Converse, A.K., et al., *Mathematical modeling of positron emission tomography (PET) data to assess radiofluoride transport in living plants following petiolar administration.* Plant Methods, 2015. **11**: p. 18.

107. Jeraj, R., T. Bradshaw, and U. Simoncic, *Molecular Imaging to Plan Radiotherapy and Evaluate Its Efficacy.* J Nucl Med, 2015. **56**(11): p. 1752-65.

108. Young, A.M., et al., *Aberrant NF-kappaB expression in autism spectrum condition: a mechanism for neuroinflammation.* Front Psychiatry, 2011. **2**: p. 27.

109. Monoranu, C.M., et al., *pH measurement as quality control on human post mortem brain tissue: a study of the BrainNet Europe consortium.* Neuropathol Appl Neurobiol, 2009. **35**(3): p. 329-37.

110. Grant, S.B., K; Krulevitch, P; Hamilton, J; Glass, R, *In vitro and in vivo measurements of fiber optic and electrochemical sensors to monitor brain tissue pH.* Sensors and Actuators B: Chemical, 2000. **72**(2): p. 174-179.

111. Schwarzkopf, T.M., et al., *Blood gases and energy metabolites in mouse blood before and after cerebral ischemia: the effects of anesthetics.* Exp Biol Med (Maywood), 2013. **238**(1): p. 84-9.

112. G, E.W.H.A.A.G.P.B.B., *A comparitive study with various anesthetics in mice (pentobarbitone, ketamine-xylazine, carfentanyl-etomidate).* Res Exp Med, 1984(184(3)): p. 159-69.

113. Saab, B.J., et al., *Short-term memory impairment after isoflurane in mice is prevented by the alpha5 gamma-aminobutyric acid type A receptor inverse agonist L-655,708.* Anesthesiology, 2010. **113**(5): p. 1061-71.

114. Constantinides, C., R. Mean, and B.J. Janssen, *Effects of isoflurane anesthesia on the cardiovascular function of the C57BL/6 mouse.* ILAR J, 2011. **52**(3): p. e21-31.

115. Kim, M., et al., *Water saturation shift referencing (WASSR) for chemical exchange saturation transfer (CEST) experiments.* Magn Reson Med, 2009. **61**(6): p. 1441-50.

116. Wen, P.Y., et al., *Updated response assessment criteria for high-grade gliomas: response assessment in neuro-oncology working group.* J Clin Oncol, 2010. **28**(11): p. 1963-72.

117. Schmainda, K.M., et al., *Characterization of a first-pass gradient-echo spin-echo method to predict brain tumor grade and angiogenesis.* AJNR Am J Neuroradiol, 2004. **25**(9): p. 1524-32.

118. Boxerman, J.L., K.M. Schmainda, and R.M. Weisskoff, *Relative cerebral blood volume maps corrected for contrast agent extravasation significantly correlate with glioma tumor grade, whereas uncorrected maps do not.* AJNR Am J Neuroradiol, 2006. **27**(4): p. 859-67.

119. Roberts, T.P. and H.A. Rowley, *Diffusion weighted magnetic resonance imaging in stroke.* Eur J Radiol, 2003. **45**(3): p. 185-94.

120. Kinahan, P.E., et al., *Attenuation correction for a combined 3D PET/CT scanner.* Med Phys, 1998. **25**(10): p. 2046-53.

121. Nuyts, J., C. Michel, and P. Dupont, *Maximum-likelihood expectation-maximization reconstruction of sinograms with arbitrary noise distribution using NEC-transformations.* IEEE Trans Med Imaging, 2001. **20**(5): p. 365-75.

122. Chan, J.K., *The wonderful colors of the hematoxylin-eosin stain in diagnostic surgical pathology.* Int J Surg Pathol, 2014. **22**(1): p. 12-32.

123. Scholzen, T. and J. Gerdes, *The Ki-67 protein: from the known and the unknown.* J Cell Physiol, 2000. **182**(3): p. 311-22.

124. Zhong, H., et al., *Overexpression of hypoxia-inducible factor 1alpha in common human cancers and their metastases.* Cancer Res, 1999. **59**(22): p. 5830-5.

125. Cai, K., et al., *Magnetic resonance imaging of glutamate.* Nat Med, 2012. **18**(2): p. 302-6.
126. Cai, K., et al., *Mapping glutamate in subcortical brain structures using high-resolution GluCEST MRI.* NMR Biomed, 2013. **26**(10): p. 1278-84.

127. Zhou, J., et al., *Differentiation between glioma and radiation necrosis using molecular magnetic resonance imaging of endogenous proteins and peptides.* Nat Med, 2011. **17**(1): p. 130-4.

128. Zaiss, M., et al., *Relaxation-compensated CEST-MRI of the human brain at 7T: Unbiased insight into NOE and amide signal changes in human glioblastoma.* Neuroimage, 2015. **112**: p. 180-8.

129. Xu, J., et al., *On the origins of chemical exchange saturation transfer (CEST) contrast in tumors at 9.4 T.* NMR Biomed, 2014. **27**(4): p. 406-16.

130. McMahon, M.T., et al., *Quantifying exchange rates in chemical exchange saturation transfer agents using the saturation time and saturation power dependencies of the magnetization transfer effect on the magnetic resonance imaging signal (QUEST and QUESP): Ph calibration for poly-L-lysine and a starburst dendrimer.* Magn Reson Med, 2006. **55**(4): p. 836-47.

131. McVicar, N., et al., *Quantitative tissue pH measurement during cerebral ischemia using amine and amide concentration-independent detection (AACID) with MRI.* J Cereb Blood Flow Metab, 2014. **34**(4): p. 690-8.

132. Zaiss, M., B. Schmitt, and P. Bachert, *Quantitative separation of CEST effect from magnetization transfer and spillover effects by Lorentzian-line-fit analysis of z-spectra.* J Magn Reson, 2011. **211**(2): p. 149-55.

133. Yoo, B., et al., *Detection of in vivo enzyme activity with CatalyCEST MRI.* Magn Reson Med, 2014. **71**(3): p. 1221-30.

134. Ortendahl, D.A. and L.E. Crooks, *Directions in magnetic resonance imaging technology.* Med Prog Technol, 1989. **15**(3-4): p. 171-84.

135. Hernando, D., et al., *Removal of olefinic fat chemical shift artifact in diffusion MRI.* Magn Reson Med, 2011. **65**(3): p. 692-701.

136. Schmiedeskamp, H., et al., *Improvements in parallel imaging accelerated functional MRI using multiecho echo-planar imaging.* Magn Reson Med, 2010. **63**(4): p. 959-69.

137. Yang, Q.X., et al., *Reduction of magnetic field inhomogeneity artifacts in echo planar imaging with SENSE and GESEPI at high field.* Magn Reson Med, 2004. **52**(6): p. 1418-23.

138. Schomberg, H., *Off-resonance correction of MR images.* IEEE Trans Med Imaging, 1999. **18**(6): p. 481-95.

139. Li, T. and S.A. Mirowitz, *Fast T2-weighted MR imaging: impact of variation in pulse sequence parameters on image quality and artifacts.* Magn Reson Imaging, 2003. **21**(7): p. 745-53.

140. Glockner, J.F., et al., *Parallel MR imaging: a user's guide.* Radiographics, 2005. **25**(5): p. 1279-97.

141. Hua, J., et al., *Quantitative description of the asymmetry in magnetization transfer effects around the water resonance in the human brain.* Magn Reson Med, 2007. **58**(4): p. 786-93.

142. Ostergaard, L., et al., *High resolution measurement of cerebral blood flow using intravascular tracer bolus passages. Part I: Mathematical approach and statistical analysis.* Magn Reson Med, 1996. **36**(5): p. 715-25.

143. Leu K, B.J., Cloughesy TF, Lai A, Nghiemphu PL, Liau LM, Pope WB, Ellingson BM., *mproved Leakage Correction for Single-Echo Dynamic Susceptibility Contrast (DSC) Perfusion MRI Estimates of Relative Cerebral Blood Volume (rCBV) in High-grade Gliomas by Accounting for Bidirectional Contrast Agent Exchange.* Am J Neuroradiol., 2016; In Press.

144. Ellingson, B.M., et al., *Recurrent glioblastoma treated with bevacizumab: contrast-enhanced T1-weighted subtraction maps improve tumor delineation and aid prediction of survival in a multicenter clinical trial.* Radiology, 2014. **271**(1): p. 200-10.

145. Shih, S.C., et al., *Molecular profiling of angiogenesis markers.* Am J Pathol, 2002. **161**(1): p. 35-41.

146. Pusztaszeri, M.P., W. Seelentag, and F.T. Bosman, *Immunohistochemical expression of endothelial markers CD31, CD34, von Willebrand factor, and Fli-1 in normal human tissues.* J Histochem Cytochem, 2006. **54**(4): p. 385-95.

147. Singh, S.K., et al., *Identification of a cancer stem cell in human brain tumors.* Cancer Res, 2003. **63**(18): p. 5821-8.

148. Bofan, M., et al., *Within-day and between-day repeatability of measurements with an electronic nose in patients with COPD.* J Breath Res, 2013. **7**(1): p. 017103.

149. Obuchowski, N.A., et al., *Quantitative imaging biomarkers: a review of statistical methods for computer algorithm comparisons.* Stat Methods Med Res, 2015. **24**(1): p. 68-106.

150. Harris, R.J., et al., *18F-FDOPA and 18F-FLT positron emission tomography parametric response maps predict response in recurrent malignant gliomas treated with bevacizumab.* Neuro Oncol, 2012. **14**(8): p. 1079-89.

151. Chang, H.H., et al., *Performance measure characterization for evaluating neuroimage segmentation algorithms.* Neuroimage, 2009. **47**(1): p. 122-35.

152. Shrout, P.E. and J.L. Fleiss, *Intraclass correlations: uses in assessing rater reliability.* Psychol Bull, 1979. **86**(2): p. 420-8.

153. Saltzherr, M.S., et al., *Metric properties of advanced imaging methods in osteoarthritis of the hand: a systematic review.* Ann Rheum Dis, 2014. **73**(2): p. 365-75.

154. Araie, M., *Test-retest variability in structural parameters measured with glaucoma imaging devices.* Jpn J Ophthalmol, 2013. **57**(1): p. 1-24.

155. Welton, T., et al., *Reproducibility of graph-theoretic brain network metrics: a systematic review.* Brain Connect, 2015. **5**(4): p. 193-202.

156. Demetriades, A.K., et al., *Applications of positron emission tomography in neuro-oncology: a clinical approach.* Surgeon, 2014. **12**(3): p. 148-57.

157. Chen, W., et al., *18F-FDOPA PET imaging of brain tumors: comparison study with 18F-FDG PET and evaluation of diagnostic accuracy.* J Nucl Med, 2006. **47**(6): p. 904-11.

158. Fueger, B.J., et al., *Correlation of 6-18F-fluoro-L-dopa PET uptake with proliferation and tumor grade in newly diagnosed and recurrent gliomas.* J Nucl Med, 2010. **51**(10): p. 1532-8.

159. Holash, J., et al., *Vessel cooption, regression, and growth in tumors mediated by angiopoietins and VEGF.* Science, 1999. **284**(5422): p. 1994-8.

160. Plate, K.H., G. Breier, and W. Risau, *Molecular mechanisms of developmental and tumor angiogenesis.* Brain Pathol, 1994. **4**(3): p. 207-18.

161. Narita, Y., *Bevacizumab for glioblastoma.* Ther Clin Risk Manag, 2015. **11**: p. 1759-65.

162. Harris, R.J., et al., *MRI perfusion measurements calculated using advanced deconvolution techniques predict survival in recurrent glioblastoma treated with bevacizumab.* J Neurooncol, 2015. **122**(3): p. 497-505.

163. Ellingson, A.M., et al., *Quantitative T2* (T2 star) relaxation times predict site specific proteoglycan content and residual mechanics of the intervertebral disc throughout degeneration.* J Orthop Res, 2014. **32**(8): p. 1083-9.

164. Zaiss, M., et al., *Inverse Z-spectrum analysis for spillover-, MT-, and T1 -corrected steady-state pulsed CEST-MRI--application to pH-weighted MRI of acute stroke.* NMR Biomed, 2014. **27**(3): p. 240-52.